THE DEVELOPMENT AND CALIBRATION OF THE ATOM PROBE FIELD-ION MICROSCOPE

By

Daniel Lewis Stoltz

A Dissertation Presented to the Graduate Council of
the University of Florida
In Partial Fulfillment of the Requirements for the
Degree of Doctor of Philosophy

UNIVERSITY OF FLORIDA

1972

Dedicated to my wife,
Orleen Faye.

Engng
9-4-73

ACKNOWLEDGEMENTS

The author would like to acknowledge and thank his advisory committee, Professors J. J. Hren, L. L. Hench, R. T. DeHoff, J. B. Conklin and E. H. Hadlock. In particular he would express his gratitude to his chairman, Professor J. J. Hren, who convinced the author of the importance of this research and who maintained an open and creative research environment to accomplish it. Also, the expert help of J. H. Bottcher, D. A. Jenkins, C. S. Kim, H. R. King, E. C. Logsdon and U. T. Son in completing the construction and calibration of the atom probe field-ion microscope was gratefully appreciated.

The author's wife, Orleen Faye, is also acknowledged for her constant encouragement, inspiration and good humor. Also, the author's parents are thanked for their lifelong encouragement and support.

Finally, the financial support of the National Aeronautic and Space Administration and Advanced Research Products Agency was appreciated.

TABLE OF CONTENTS

Page

ACKNOWLEDGEMENTS iii

LIST OF FIGURES vi

ABSTRACT ix

CHAPTER

I INTRODUCTION 1

II FIELD EVAPORATION 6

Introduction 6
Theoretical Background 8
Experimental Verification 24

III ATOM PROBE FIELD-ION MICROSCOPE 33

Introduction 33
Technical Design and Material Selection 37
Description of Atom Probe 40

IV ATOM PROBE CALIBRATION 72

Introduction 72
Performance of Individual Components . 72
Operational Performance and Calibration 89

V FIELD EMISSION AND IONIZATION MICROSCOPE 115

Introduction 115
Description of Microscope 116
Description of Field Emission Analysis 126

VI CONCLUSIONS 150

TABLE OF CONTENTS (continued)

Page

LIST OF REFERENCES 155

BIOGRAPHICAL SKETCH 159

LIST OF FIGURES

Figure Page

1 Potential energy diagrams for (a) a surface atom, (b) a surface ion, and (c) a surface ion in the presence of a field 11

2 Three possible field evaporation models: (a) simple ionic bonding, (b) evaporation over the Schottky barrier after transition from atomic to ionic state at x_n, and (c) ionization at x_n followed by immediate evaporation 11

3 Potential energy curves illustrating the various correction terms for both the image-hump model (a) and the intersection model (b) 15

4 Energy scheme for field evaporation of a nonmetallic impurity as: (a) a monatomic ion and (b) a molecular ion 23

5 Principle of operation of the atom probe field-ion microscope 34

6 Atom probe field-ion microscope 41

7 Ultra-high vacuum system for atom probe . 42

8 Initial atom probe specimen holder 47

9 Physical arrangement of specimen holder and manipulator in atom probe . . . 48

10 Final specimen holder and mechanical manipulating assembly 50

11 Specimen holder and manipulating rod assembly in biased position 53

12 Principle of microchannel-plate image intensifier 55

LIST OF FIGURES (continued)

Figure Page

13 Microchannel-plate image intensifier for atom probe 57

14 Atmospheric high voltage feedthrough for atom probe 62

15 Circuit diagram of preamplifier 67

16 Detection circuitry for atom probe 68

17 Specimen manipulation provides observation of nearly entire surface of tip . . . 77

18 Analog mode circuitry for Spiraltron detector 83

19 Neon ion current vs. applied potential to Spiraltron detector in analog mode . . 85

20 Optimum focusing potentials for microchannel-plate and phosphor-coated screen 94

21 Micrograph of tungsten covered with gaseous contaminants at 78°K 98

22 Random signals detected from triggered Tektronix 549 Storage Oscilloscope on 500 μsec traces 100

23 Tektronix 549 Storage Oscilloscope 20 μsec traces of field desorbed species from tungsten surface, where V_{dc} = 7.5 kV and V_p = .9 kV 101

24 Micrograph of tungsten at 78°K imaged in helium-10 percent neon 106

25 Tektronix 549 Storage Oscilloscope, 20 and 10 μsec traces for field-evaporated tungsten at 78°K in helium-10 percent neon 107

26 Constructed field emission and ion microscope 117

LIST OF FIGURES (continued)

Figure Page

27 Ultra-high vacuum system for microscope . 119

28 Sequence involved with specimen exchange mechanism 122

29 Atmospheric high voltage feedthrough circuitry for microscope 127

30 Calibration of Brandenburg high voltage supply 128

31 Circuit for point-by-point measurement of ℓn I vs. 1/V 130

32 Circuit for automatic measurement of ℓn I vs. 1/V 132

33 Calibration of photomultiplier current vs. Quantum Radiometer 134

34 Field-ion and field emission images of tungsten obtained from fiber-optic screen 136

35 Field emission data for tungsten 138

36 Silicon weight loss vs. time for different HF-HNO_3 solutions 141

37 An acceptable silicon tip mounted to a nickel lead 143

38 Field-ion micrographs of phosphor-doped silicon imaged at 78°K in a helium-10 percent neon mixture at $5x10^{-4}$ Torr 144

39 Computer simulated field evaporation of the (100) pole of silicon 148

Abstract of Dissertation Presented to the Graduate Council
of the University of Florida in Partial Fulfillment of the
Requirements for the Degree of Doctor of Philosophy

THE DEVELOPMENT AND CALIBRATION OF THE ATOM PROBE FIELD-ION MICROSCOPE

By

Daniel Lewis Stoltz

December, 1972

Chairman: John J. Hren
Major Department: Materials Science and Engineering

Since field evaporated surface atoms are identified with the atom probe field-ion microscope, the theoretical parameters of the essential field evaporation process are reviewed. The current status of the image-hump and intersection models, field strength, field evaporation rates and the field evaporation of alloys is described. The experimental verification discussions include the rate sensitivities, imaging gas effect and pulsed field evaporation. In addition, current atom probe results are discussed that indicate further experimental data are needed to provide a quantitative field evaporation theory.

A detailed description of the technical design, material selection, fabrication and construction of the individual components for the completed atom probe field-ion microscope is presented. In particular, the ultra-high vacuum system, specimen holder, internal microchannel-plate

image intensifier, Bendix Spiraltron detector, impedance matched of the high voltage pulse to the high voltage feedthrough circuitry, high voltage power supplies and electronic circuitry are discussed separately.

The operational performance and calibration of the completed atom probe field-ion microscope are described. In particular, the specimen holder and mechanical manipulator assembly allowed the tip surface a minimum of 60° rotation providing the tip was precisely positioned within ±.3 mm of the optical axes. Voltages were applied up to 24 kV without breakdown. The Spiraltron detector was operational in both the analog and pulse counting modes and was found to limit the effective sensitive area of the tip to 30 and 50 Å^2 for 400 and 800 Å tip radii, respectively. Critical alignment of the Spiraltron detector and the specimen tip was achieved by optical, laser and electronic means. A detrimental defocusing effect was observed and was attributed to a long time constant and residual charge buildup at the perimeter of the probe holes in the microchannel-plate and phosphor-coated screen. This defocusing effect was corrected by utilizing the microchannel-plate and screen as electrostatic einzel lenses. Optimum focusing potentials were determined.

Gas desorption studies of tungsten surfaces indicated from the 20 μsec traces with the Tektronix 549 Storage Oscilloscope the following ionic species: H^+, N^{++}, N^+, O^+,

O_2^+, CO_2^+, WN_2^+ and possibly $W_2O_5^+$. The efficiency in detecting aligned single particles was about 50 percent. Although the efficiency of the fixed probe hole method was less, the method was successfully used to monitor the field evaporation of the tungsten.

Field evaporation studies of tungsten at 78°K in He-10 percent Ne revealed from the 10 and 20 µsec traces of the Tektronix 549 Storage Oscilloscope the following species: CO_2^+, H^+, Ne^{++}, N^{++}, O^+, WO_2^{+4}, WO_2^{+3}, WH_2^+, $WO_2 \cdot H_2O^+$ and possibly $W_2O_5^+$ and WH_2^{+4}. No tungsten-helium and -neon compounds were identified from these traces; however, the overlapping of the various isotope forms of tungsten-hydride and -helide compounds prevented their unambiguous distinction. The efficiency of detecting aligned surface atoms was less than 50 percent, but this was improved by aligning the probe hole on the inside of the ionization ring.

The practical mass resolution of the atom probe was ±.5 AMU (atomic mass unit) for m/n ratios below 100 and ±.7 AMU for m/n values above 100. These values were obtained for the assumed pulse factor of two. It was discovered that the determined AMU values did not differ more than ±.2 AMU when the electronic dead time was assumed a maximum of .060 µsec, so it was neglected in the ionic species identification. Accurate determination of the pulse factor and electronic dead time can be obtained when a more favorable statistical representation of detected species is obtained.

CHAPTER I

INTRODUCTION

The historical development of the atom probe field-ion microscope originated when field ionization was used as a source for mass spectrographic investigations by Inghram and Gomer,(1) Beckey(2) and Block.(3) Results obtained from these studies of H_2, D_2, N_2, O_2 and hydrocarbon gases ionized by a field-ion emitter were quite different from previous results obtained from conventional ion sources. Mass spectrographic analysis of the field evaporated ionic species, however, was difficult experimentally because of the rapid blunting of the emitter tips. Despite this problem, Müller and Thomsen(4) observed the copper hydride products of a hydrogen promoted field evaporated copper emitter. Also, Vanselow and Schmidt(5) observed several platinum and platinum oxide species that were field evaporated from platinum tips which had been heated between 1300 and 1500°K. Finally, Barofsky and Müller(6) performed the first spectrometric analysis of metal emitters cooled between 21 and 300°K. Field evaporated species of beryllium, iron, cobalt, nickel and copper were identified as hydrides by a focusing mass spectrometer which was capable of scanning up to 90 AMU (atomic mass units) in approximately 9 seconds. However, the sensitivity of this instrument was limited by the significant signal-to-noise ratio. While concentrating on means to minimize this problem, Müller(7) conceived the idea of detecting only one single particle and eliminating the noise discrimination problem by imposing a strict correlation between the initiation of the field evaporation and the detection event.

In order to satisfy these conditions the developed instrument, the atom probe field-ion microscope, combined the atomic resolution of the field-ion microscope with the single particle detection capability of the time-of-flight mass spectrometer. By locating a probe hole in the center of the phosphor-coated screen of the field-ion microscope a single surface atom could be selected and field evaporated to the aligned ion detector. In 1967 the first prototype atom probe was completed by Müller *et al.*(8,9) This instrument has been modified recently to provide better vacuum capabilities, specimen manipulation and photographic recording of the images. Brenner and McKinney(10) independently constructed an atom probe that was similar to Müller's but featured an internal gimbal system to provide two axes of rotation for the tip. This instrument was designed also to apply a negative high voltage pulse to the tip through a flexible, unshielded wire loop, rather than applying a positive pulse directly to the tip as done originally by Müller. The main disadvantage of this method is the reported loss in mass resolution and detector efficiency of the atom probe.(11) At this date, these two research groups are the only ones conducting active research with the atom probe field-ion microscope.

The initial significant experimental result obtained by Müller with the atom probe was the detection of three- and four-fold charged metallic ions and their oxide and nitride compounds which had been field evaporated from tungsten, rhenium, tantalum and niobium surfaces.(9,12) In addition, Brenner and McKinney(13) independently observed two and three positive charges for iridium and confirmed the highly charged ions for tungsten. It was also observed that the amount of these highly charged ions increased as the field evaporation rate was increased. Another surprising observation made by Müller with the atom probe was the adsorption of helium, neon and argon at the metal surfaces.(14) The field strength required to remove these adsorbed inert gases was sufficient to evaporate the surface metallic atoms simultaneously.(14) Brenner and McKinney reported that the adsorption of helium was observed even when the helium gas pressure was reduced to 5×10^{-9} Torr.(15) The reported ±.2 AMU mass resolution capability with Müller's atom probe allowed the important observation of field desorbed metal-noble gas molecular ions, $RhHe^{+2}$ and WHe^{+3}.(14) Other experiments in which tantalum was field evaporated in helium and neon imaging gases indicated that the surface binding of helium and neon might be an activated chemisorption with the activation energy supplied by the strong polarization of the surface atoms exposed to the field.(16) All of these experimental results are not predicted by the current field evaporation and ionization theories and must be incorporated in them to provide a quantitative description.

The experimental results obtained by the atom probe field-ion microscope emphasize the unique sensitivity and versatile capabilities available with the instrument for surface studies and microanalysis. Consequently, this powerful instrument can supply sophisticated experimental evidence for many scientific disciplines. For example, in physics the atom probe can be used to study the following: field ionization and field evaporation parameters to provide a quantitative description of these processes, the nature of "clean" metallic surfaces, the measurement of the polarization factor and the high electric field penetration of a metallic surface, the peculiar formation of metal-inert gas molecules, and the influence of emerging defects on the surface's structural and electronic properties. Chemists, on the other hand, might apply the atom probe to the following investigations: determination of single particle chemical composition, mass spectrometry of molecular species (since the molecule will not be fragmented by this technique), the formation of the adsorbed gaseous layers, and possibly catalytic reactions, by the high field. Besides applying the atom probe to specific field-ion microscopic problems, the material scientist has a very wide scope of possible investigations for which the atom probe can supply invaluable information. For instance, order-disorder transformations, spinodal decomposition, solute atom distribution, interfacial segregation, oxidation and corrosion, surface diffusion, surface binding energy determinations, nucleation of vapor-deposited films, heterogeneous nucleation of defects and microanalysis.

The present research will describe in detail (a) the theoretical foundation of the phenomena embodied in field-ion mass spectrometry, (b) the design associated with producing such an instrument, and (c) data relative to the use of the field-ion and field emission microscopic features and the single particle identification capability of the calibrated atom probe device.

CHAPTER II

FIELD EVAPORATION

Introduction

The attainment of a "clean" solid surface involves sophisticated techniques and ultra-high vacuums below 10^{-10} Torr. Under these conditions reasonable periods of time are realized to conduct experiments concerning the nature and characterization of the "clean" surface prior to its coverage with gaseous adsorbates. One of the most unique methods used to create "clean" surfaces is associated with field-ion microscopy. In field-ion microscopy a nearly hemispherical, atomically smooth surface must be produced to develop radially projected images with 10^6 magnification and 2 to 3 Å resolution. To produce this "clean" surface from a cryogenically cooled specimen the electrostatic field at the tip is increased until the surface contaminates are desorbed and the atomic asperities are evaporated as ions. This technique was designated "field evaporation" by its innovator, Müller,(17,18) in 1941. At that time, experimental techniques were adequate to produce the necessary 5 to 8 V/Å potential at the tip and to observe the stripping of the surface atoms with a helium image. In addition to producing "clean" surfaces, field evaporation can be repeated on a specimen to achieve an atomic layer by atomic layer serial sectioning of the bulk structure and to observe any defects in the bulk as they emerge at the surface.

Since field evaporation is essential to field-ion microscopy, it is important to understand how the field evaporated surface is formed and its influence on the resulting field-ion image's interpretation. Ideally, the field evaporation theory should determine initially the evaporation of individual atoms with respect to temperature, field strength and chemical properties. Next, the theory should consider the surrounding structure's influence on the evaporating species. Such parameters would include crystal structure and orientation, electronic structure, specimen size, solute and impurity atoms, and the presence of residual gases in the microscope body. From these factors one should be able to predict the final shape or "end form" of the evaporated specimen, plus the necessary parameters to control the evaporation process. Due to the complexities involved with this process, the current theory provides only a qualitative description and is being modified constantly to better explain sparse amounts of available experimental data. Consequently, it is the purpose of this section to review briefly the current status of the field evaporation theory and discuss the pertinent experimental measurements.

Theoretical Background

Activation Energy

The primary theoretical problem involves determining the activation energy, Q, necessary to field evaporate surface atoms as a function of the applied potential, V. Müller$^{(18)}$ envisioned this process as a special case of a thermionic cycle and expressed the activation energy needed to remove a surface atom without an applied field as

$$Q_o = \Lambda + \sum_n I_n - n\Phi \ , \tag{1}$$

where Λ is the sublimation energy needed to free the surface atom from its potential well at the surface, as shown in Figure 1(a). The terms $\sum_n I_n$ represent the additional energy required to ionize the sublimated or gaseous atom with a charge of ne; i.e., the term I_n corresponds to the n^{th} ionization potential. When the metallic atom is ionized, the ejected electrons from the atom return to the metal surface and contribute a potential energy, $n\Phi$, to the metal. Consequently, Φ in relation (1) represents the total, not absolute, work function because it corresponds to the potential energy difference of an electron located at the Fermi surface and at infinity in a vacuum.$^{(19)}$ Consequently, the activation energy, Q_o, is illustrated in Figure 1(b) as the energy increment between the bottom of the atomic potential well and the zero level of the ionic potential. Note that the zero levels of the ionic and atomic potential energies are separated by the amount $\sum_n I_n - n\Phi$.

When a positive potential is applied at the specimen tip the ion experiences a repelling potential equivalent to $-neF\chi$, where F is the electric field, χ is the distance between the ion and the metal surface, and ne is the number of electronic charges. Correspondingly, an attractive image-force term is formed by the rearrangement of surface charge on the metal due to the ion's presence and is equal to $-(ne)^2/4\chi$. In addition, Brandon(21) proposed that another short range repulsive term $V_{r_n}(\chi)$ must be included. So, the ionic potential in the presence of a field, as illustrated in Figure 1(c), is equivalent to

$$V_i(\chi,F) = V_{r_n}(\chi) - neF\chi - \frac{(ne)^2}{4\chi} . \qquad (2)$$

Generally, the short range repulsion term $V_{r_n}(\chi)$ is neglected(4) because the ionization process is assumed to occur at a sufficiently great distance from the atomic surface. Consequently, expression (2) is approximated by

$$V_i(\chi,F) \cong - neF\chi - \frac{(ne)^2}{4\chi} . \qquad (3)$$

Differentiation of expression (3) to obtain the maximum energy, referred to as the image-hump or Schottky barrier, results as follows,

$$\chi_s = \left(\frac{ne}{4F}\right)^{1/2} \text{ or } \left(\frac{3.6n}{F}\right)^{1/2} , \qquad (4)$$

where χ_s is Å and F is V/Å. This position χ_s is illustrated in Figure 1(c).

If the ionic potential curve of Figure 1(c) is superimposed on the atomic potential curve of Figure 1(a), three possible models for field evaporation are devised. Under the condition that $\sum_n I_n - n\Phi$ is small, the ionic and atomic potential curves do not intersect and the resulting model represents simple ionic bonding, as shown in Figure 2(a). The second and third possibilities assume the usual conditions for metals, i.e., the $\sum_n I_n - n\Phi$ term is large, which allows intersection of the two potential energy curves. In Figure 2(b) the atomic state is stable at the surface and the two curves intersect left of the Schottky barrier. This means that the atom has sufficient energy to be ionized at the intersection distance, χ_n. However, to be evaporated the ion must have additional kinetic energy to overcome the Schottky maximum or it will be forced back into the stable interior of the metal. This evaporation process was introduced by Müller(17,18) and is referred to as the image-hump or image-force model. The required activation energy for this model is given by

$$Q_n = Q_o - neF\chi_n - \frac{(ne)^2}{4\chi_n} = Q_o - (n^3e^3F)^{1/2}, \quad (5)$$

where Q_o is given by expression (1).

The third possibility represents the atomic potential curve intersecting the ionic curve to the right of the Schottky barrier. This occurs when the atom has sufficient energy to ionize at the intersection point χ_m and is

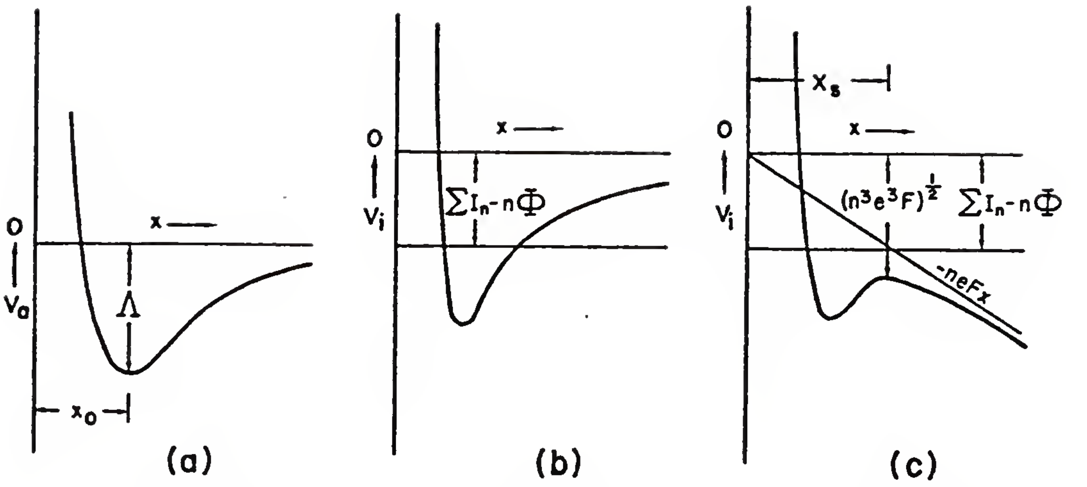

Figure 1. Potential energy diagrams for (a) a surface atom, (b) a surface ion, and (c) a surface ion in the presence of a field.(20) (Note the difference in the zero energy level for the atom and ion.)

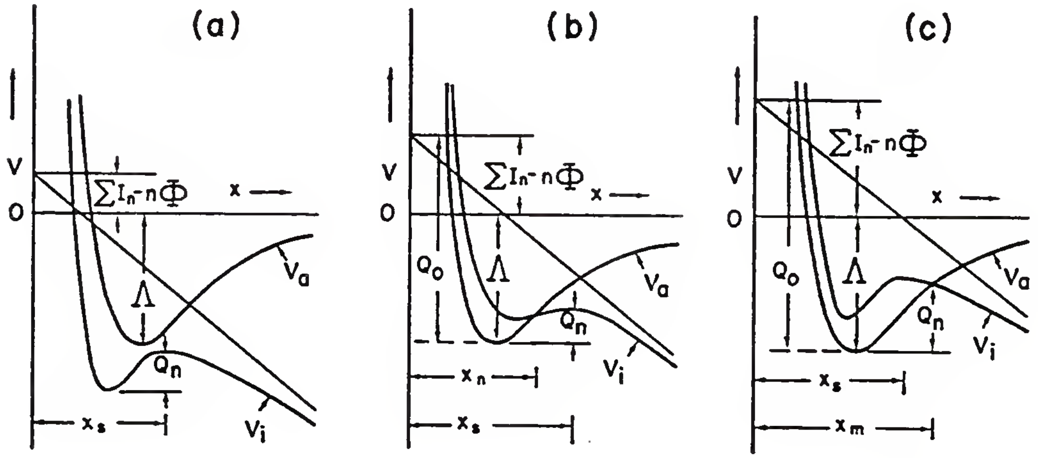

Figure 2. Three possible field evaporation models: (a) simple ionic bonding, (b) evaporation over the Schottky barrier after transition from atomic to ionic state at x_n, and (c) ionization at x_n followed by immediate evaporation.(20)

spontaneously repelled from the surface. Gomer(22) introduced this intersection model of the evaporation process and expressed its required activation energy as

$$Q_n = Q_o - neF\chi_m - \frac{(ne)^2}{4\chi_m} , \qquad (6)$$

where χ_m is the distance between the metal surface and the ionization region; i.e., the point of intersection of the two potential energy curves. Brandon(23) also noted that the activation energy of the image-hump model could be linearly dependent on the field, if a significant short-range repulsive potential $V_{r_n}(\chi)$ existed for the ion. This would effectively reduce or possibly eliminate the Schottky barrier and invalidate expression (3).

Several corrections to the activation energy expressions (5) and (6) have been reported for both models. Müller(24) and Gomer and Swanson(25) have added an important term, $\frac{1}{2}(\alpha_a - \alpha_i)F^2$, to both relations (5) and (6). This term represents the difference in the dipole polarizability of the metal atom, α_a, and the singly charged ion, α_i, and disregards the reported higher order polarization terms.(26) The effect of this polarization difference is equivalent to assuming larger values of Q_o for a given field. Typically, polarization corrections amount to 1 to 3 eV. In addition, when the different types of surface binding were considered by Gomer and Swanson(25) with the intersection model, broadening of energy levels and energy shifting became significant for covalent bonding. Thus, the activation energy expressed in relation (6) was appropriately corrected, as follows:

$$Q_n = \Lambda + \sum_n I_n - n\Phi - \frac{(ne)^2}{4\chi_m} - neF\chi_m - \frac{\Gamma}{2} - \Delta E \qquad (7)$$

where ΔE is the shift of energy level and Γ is the energy level broadening value which is given as the ratio of Planck's constant h and the electronic transition time τ. Note that expression (7) also indicates a linear relationship between Q_n and F. Recently, Gadzuk(27) reported a detailed analysis that included calculated energy level broadening and shift effects for cesium on tungsten and potassium on platinum. The broadening value was approximately 1 eV and the energy shift was about 0.3 eV.

Another important factor to consider is the electric field penetration of the metal surface. By assuming the metal surface to be an abrupt termination of a periodic array of atoms, it will be void of conduction electrons and can be penetrated by the electric field to a finite screening distance, λ. This effect reduces the ionic potential curve by an amount neFλ. In addition, if the intersection model assumes that the surface mirror plane of the metal coincides with its assumed surface-vacuum interface, the surface atoms would experience this electric field penetration and its term must be added to relation (7). Although the assumed metal surface does not correspond to the real surface, the corrected expression (7) provides reasonable agreement between the calculated and experimental activation energies for desorbed inert gas atoms and highly charged ions of tungsten.(26)

These corrections are illustrated schematically in Figures 3(a) and (b) for the respective image-hump and intersection models. Considering the various assumptions made for each model, the image-hump model would appear more valid if a Schottky hump really existed and is located beyond χ_n in Figure 3(b). However, values of χ_s, calculated from relation (4), for typical experimental parameters were less than the radius of most ions for both singly and doubly charged ionic species.(11)

Quantum mechanical treatment of metal surface potentials was undertaken initially by Bardeen(28) and later refined by Juretschke(29) and Loucks and Cutler.(30) These calculations indicate that the classical image potential remains valid at a large distance from the metal surface, whereas quantum mechanical exchange and correlation forces predominate near the surface. Consequently, these calculations also indicate there is no theoretical basis for the Schottky barrier to exist for singly and doubly charged ions. In addition, its existence with triply charged ions is doubtful. However, calculations for higher ionic charges suggest its possible existence.(26)

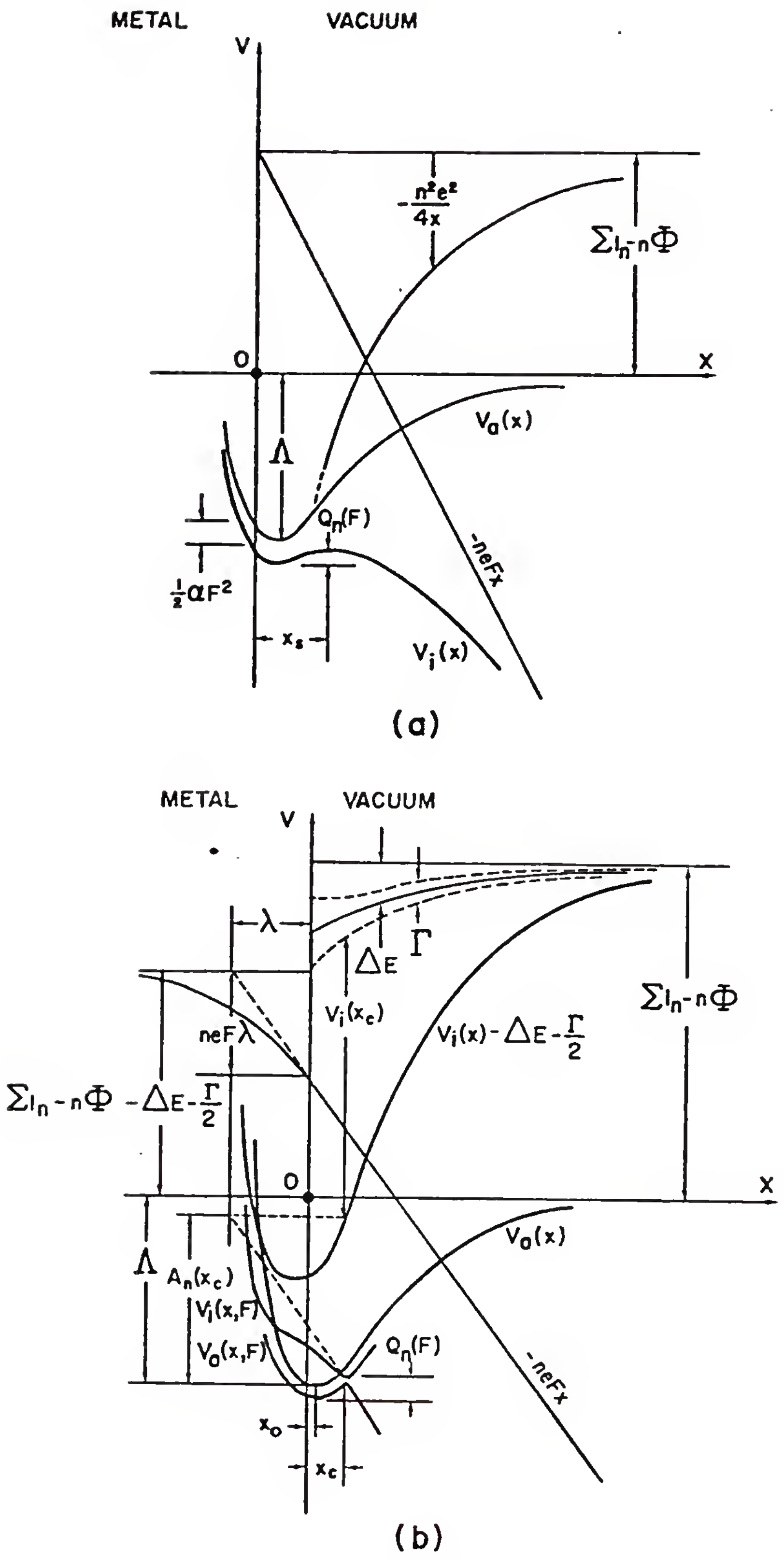

Figure 3. Potential energy curves illustrating the various correction terms for both the image-hump model (a) and the intersection model (b).(9)

Evaporation Field Strength

At the cryogenic temperatures used in field-ion microscopy the activation energy, Q_n, is assumed negligible. With this assumption the evaporating field, F_{e_n}, can be determined from the respective activation energy relations for both the image-hump and intersection models. For the image-hump model the evaporating field is determined from relation (5) and is expressed as

$$F_{e_n} = \frac{(\Lambda + I_n - n\Phi)^2}{n^3 e^3} \quad , \qquad (8)$$

providing the polarization and field penetration terms are neglected. The evaporation field for the intersection model was determined from relation (7) and is equivalent to

$$F_{e_n} = \frac{\Lambda + I_n - n\Phi - 3.6n^2/r_o}{nr_o} \text{ V/Å} \; . \qquad (9)$$

Both $\Lambda/2$ and ΔE were neglected in expression (7) because their contributions are small. Q_n was assumed zero and χ_n was assigned the single bond atomic radius, r_o, of the metal atom. As mentioned previously, the existence of the Schottky barrier is difficult to predict theoretically. Consequently, it is not possible to state if the atom will tunnel or be thermally excited over the Schottky hump by either of these two evaporation models. Despite this uncertainty, useful data(24,31) comparing the evaporation fields for various metals were determined from the image-hump model by Müller(24) and Brandon.(31) Brandon's(31) calculations also indicated that the doubly charged ions had lower evaporation fields than the singly charged ions. Predicting the evaporation field required to evaporate triply and higher charged ions is limited because their ionization potentials and sublimation energies are unknown.

Other factors contribute to the strength of the evaporating field which are not included directly in the above relations (8) and (9). For instance, the degree of protrusion of the atom, the location of an atom in the crystallographic plane and the tip geometry should be included. The complex interaction of the various field evaporating variables led Brandon(31) to introduce the following relation

$$F = \beta_1 \beta_2 F_a , \tag{10}$$

where β_1 is the field enhancement factor related to the local radius of curvature, β_2 is the field enhancement factor due to local lattice geometry, particularly the lattice step height, and F_a is the average field on a tip. Gomer(22) equated the average field strength F_a as follows

$$F_a = \frac{1}{k} \frac{V}{R} , \tag{11}$$

where k is a semi-constant (normally 5), V is the applied tip potential and R is the tip radius. When the product $\beta_1\beta_2$ in relation (10) is practically constant, the stable tip will exhibit a surface with flat, close-packed planar regions due to their large lattice step heights. In achieving this stable condition the weakly bound atomic sites at the edges of the close-packed planes were field evaporated initially. Even when the tip surface is stable, the field strengths over the different regions of the surface are not uniform due to the slight changes in radii of curvatures.

Field Evaporation Rates

The field evaporation rate k_{e_n} for both the image-hump and intersection models assumes that the process is thermally activated and obeys the Arrhenius rate equation of the form

$$k_{e_n} = \nu_n \exp\{-Q_n/kT\} , \qquad (12)$$

where ν_n is the vibrational frequency of the surface atom, Q_n is the activation energy, k is the Boltzmann constant and T is the absolute temperature. Further considerations indicate that quantum mechanical tunneling predominates at low temperatures.(22,25,32,33) Consequently, the rate constant is approximated by

$$k_{e_n} \cong \nu_n \exp\{-a_n \, Q_n{}^{3/2}\} , \qquad (13)$$

where a_n is dependent on the atomic mass as well as the shape of the potential barrier and is a slow function of the electric field F. At intermediate temperatures, optimum rates are combinations of the thermal activation and tunneling processes. Gomer and Swanson(25) and Tsong(33) extended their field desorption process to determine the rate of field evaporation for either lattice atoms or adatoms with masses similar to the substrate mass, where $h\nu << kT$. The resulting rate appeared as follows

$$k_e \cong p\nu \exp\{\frac{-Q_n}{kT} + \frac{4}{27a_n^2(kT)^3}\} , \qquad (14)$$

where p is the electronic transition probability, ν is the surface atom vibrational frequency and a_n is the constant described for relation (13). This expression is similar to the rate equation for ionic bonding and indicates that the field evaporation involves three steps: thermal excitation to higher vibrational levels, electronic transition and atomic or ionic tunneling.(11) Gomer and Swanson determined values for the pre-exponential factor, p, which indicated that a two-electron transition was more favorable than a single electron transition by two to four orders of magnitude.

Another field evaporation rate expression was introduced by Tsong(26) and Müller(34) which describes the absolute rate of the desorption of single adatoms as a function of the electric field. This rate is

$$k_e(F) = \frac{1}{N\tau} \sec^{-1} , \qquad (15)$$

where N is the number of pulses of width τ and field strength F required to evaporate an adatom. Since the evaporation rate, k_e, increases eight orders of magnitude by raising the field by approximately 10 percent,(26,34) it is very important to accurately determine the field strength experienced by the individual adatoms. Consequently, expression (15) becomes very important when an evaporating pulse of known strength and duration is utilized with the atom probe field-ion microscope(26) to identify individual adatoms or lattice atoms. This method of field evaporation is very versatile because it provides an accurate measure of the field strength required for evaporating individual atoms. For instance, Plummer and Rhodin(35) reported that the required field intensity decreased about 10 percent when scanning from the center to the edge of the tungsten (110) plane.

Field Evaporation of Alloys

Theoretical considerations pertaining to the field evaporation of dilute alloys differ from the previously described pure metal case. Observed field-ion images of dilute alloys reveal a lack of surface regularity and sharply resolved high index planes. This suggests that the presence of the solute atoms in the solvent lattice either creates preferred field evaporation or the solute atoms are merely invisible. Brandon(36) considered this effect in terms of thermodynamic quantities. These include $\Delta \overline{H}_s$ (heat of sublimation of pure solute), H_s (heat of solution), E_d (dissociation energy of diatomic gas rather than the monatomic solute ion), and H_A (heat of adsorption). From expression (1), which represents the activation energy required to remove an ion of charge n from the metal lattice, Brandon determined from the image-hump model that $Q_o = (n^3e^3F_n)^{1/2}$, providing Q_n was assumed a minimum and the polarization and penetration corrections were ignored. F_n is the field strength required to evaporate the ion at 0°K. The sublimation energies for the monatomic solute ion and the diatomic gases are approximated by relations (16a, b and c) respectively.

$$\Lambda \cong \Lambda_o - \Delta\overline{H}_s \ , \tag{16a}$$

$$\Lambda \cong \Lambda_o + H_s \ , \tag{16b}$$

$$\Lambda \cong E_d + H_A \ . \tag{16c}$$

By substituting these calculated sublimation energies and the predicted ion charges ($n^{-3/2}\ Q_o = Q_n$ is a minimum) into expression (1), the evaporation field, F_n, can be determined. With the available values of H_s and H_A the general condition, $H_A > -\Delta H_F > H_s$, was noted where $-\Delta H_F$ is the selected compound's heat of formation. This indicates that if the solute atom has a lower free energy at the surface as compared to the bulk, the difference in energy must appear as a reduced average binding energy for nearest neighboring solvent atoms at the surface when the migrating solutes reach the surface. Therefore, as field evaporation occurs, the solvent atoms will evaporate preferentially to expose the underlying impurity atom. This effect was observed by Machlin *et al.*(37)

To provide more physical insight into this process, Brandon(36) selected iron as the solvent and calculated the field strengths expected to evaporate the various solutes normally present in iron. The results predicted that either the solutes evaporated with a preferred ionic charge or remained in the lattice. More important, however, his calculations indicated that nonmetallic solutes, such as C, O_2 and N_2, required extremely high evaporation fields and without another evaporation mechanism would remain on the iron surface. One of the proposed processes considered the field evaporation of a molecular ion composed of the metal atom and the nonmetallic solute atom. Brandon(36) presented the following condition for such an event:

$$\Lambda_m - (E_d + H_A) < \sum_n I_g - \sum_n I_d , \qquad (17)$$

where Λ_m is the sublimation energy of the molecule from the metal lattice, $\sum_n I_g$ is the total ionization potential of the nonmetallic impurity, and $\sum_n I_d$ is the total ionization potential of the metal-impurity molecule. The appropriate potential energy scheme based on the assumption that the metal-impurity complex will have the identical charge as the metal ion is shown in Figure 4. Presently, limited data for these thermodynamic quantities prevent a detailed prediction of whether molecular ions are either field evaporated or dissociated. However, experimental results from the analyses of field evaporated species have produced evidence of the existence of molecular ions. For instance, multiply charged

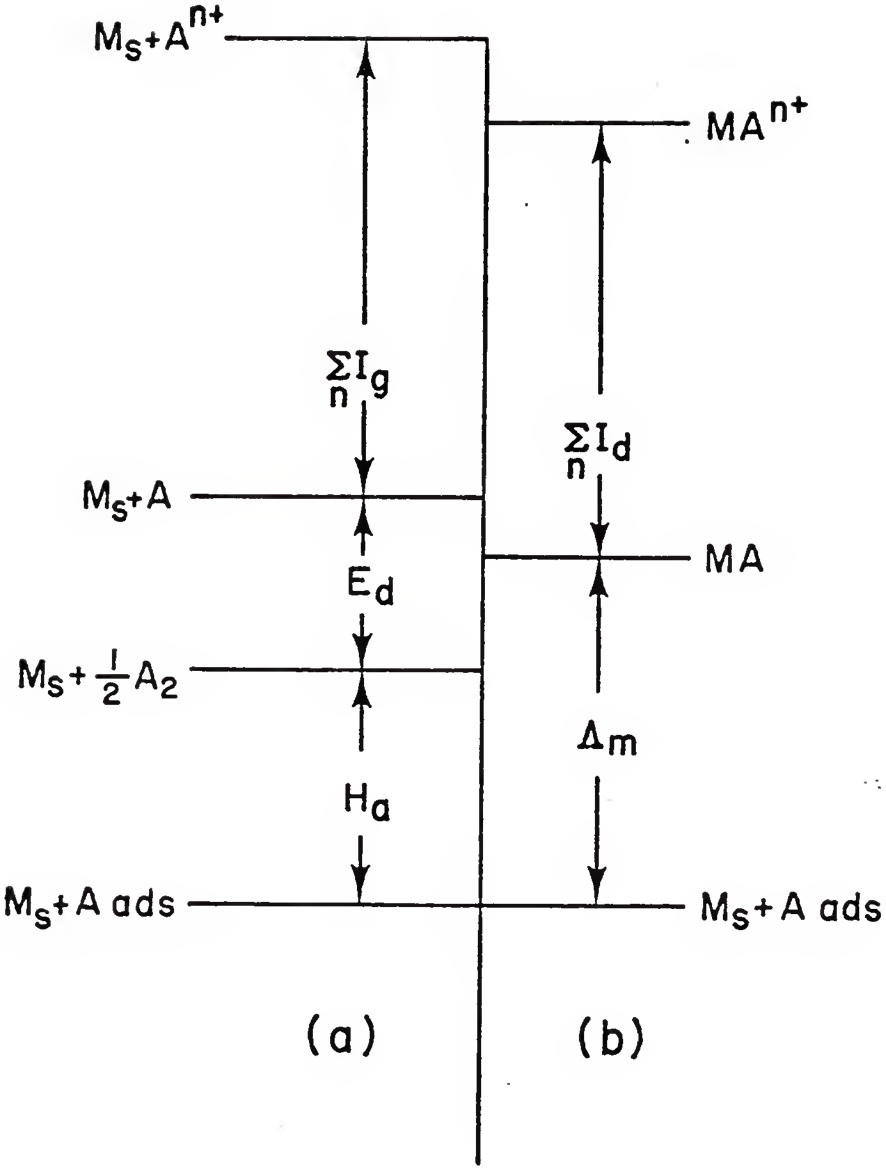

Figure 4. Energy scheme for field evaporation of a nonmetallic impurity as: (a) a monatomic ion and (b) a molecular ion.(36)

oxide and nitride molecular ions of metals, CuO^+, NiO^+, FeO_2^{++}, FeN_2^{++}, WO_2^{3+} and WN_2^{4+}, were observed by either magnetically focused mass spectrometers(6) or by atom-probe field-ion analyses.(9)

Experimental Verification

Rate Sensitivities

Examination of the Arrhenius rate equation, $k_{e_n} = \nu_n \exp\{-Q_n/kT\}$, and the activation energy for the image-hump model including the polarization factor

$$Q_n = Q_o - (n^3e^3F)^{1/2} + \frac{1}{2} (\alpha_a - \alpha_i) F^2 \qquad (18)$$

reveals two means to vary the rate of evaporation. An increase in temperature with both the electric field and activation energy constant will increase the evaporation rate. Also, as the field is increased, the evaporation rate will increase providing the temperature remains constant and the activation energy decreases. The sensitivity of the evaporation rate to the field at a constant temperature is designated field sensitivity,(32) while the sensitivity of the evaporation rate to the temperature at a constant field determines the temperature sensitivity. Both terms are classified as rate sensitivities. Another experimental approach introduced by Brandon(32) utilizes the variation of both temperature and field to keep a constant evaporation rate. Mathematically, this method is related directly to the first two sensitivities and the experimental value is designated the rate sensitivity.

The Arrhenius relation is differentiated to determine the theoretical values for these various rate sensitivities to allow comparison with the experimental work. The field sensitivity, S_T, is determined as follows(20,38):

$$S_T = \left.\frac{d\ \ell n(k_{en})}{d\ \ell n(F)}\right|_T = \left.\frac{F\ d\ \ell n(k_{en})}{dF}\right|_T = \frac{-F}{kT}\left(\frac{dQ_n}{dF}\right) . \tag{19}$$

The temperature sensitivity, S_F, is obtained by differentiating the Arrhenius equation with respect to $\ell n(T)$ and is shown to be equivalent to

$$S_F = \left.\frac{d\ \ell n(k_{en})}{d\ \ell n(T)}\right|_F = \frac{Q_n}{kT} = \ell n\left(\frac{\nu_n}{k_{en}}\right) . \tag{20}$$

The third sensitivity, S_k, maintains a constant evaporation rate and is defined as

$$S_k = \left.\frac{d\ \ell n(F)}{d\ \ell n(T)}\right|_{kn} . \tag{21}$$

All three of these sensitivities apply to both the image-hump and intersection models by merely choosing the appropriate field evaporation activation energy relation.

Tsong(33) assumed that the pre-exponential term ν_n in the Arrhenius relation was a slowly varying function of field and temperature as compared to the exponential dependence of k_{en} for these parameters. Thus, by approximating ν_n as a constant one can obtain

$$Q_n = k\ T\ \ell n \left(\frac{\nu_n}{k_{en}} \right) \quad ,$$

$$\frac{d\ Q_n}{d\ \ell n(F)} = k\ T\ \ell n \left(\frac{\nu_n}{k_{en}} \right) \frac{d\ \ell n(T)}{d\ \ell n(F)} \Bigg|_{k_{en}} \qquad (22)$$

Rearranging and solving for $\ell n(\nu_n/k_{en})$ results in

$$\ell n \left(\frac{\nu_n}{k_{en}} \right) = -S_T\ S_k\ . \qquad (23)$$

In principle, the experimental determination of both the rate sensitivities, S_T and S_k, from relations (19) and (23), respectively, will allow Q_o and ν_n to be measured. Brandon$^{(32)}$ followed such an approach and calculated a ν_n value of $5x10^{10}$ layers/sec for tungsten from experimental S_T and S_k values. This value was the same order of magnitude as the atomic vibrational frequency (10^{12}-10^{13}/sec) if one uses Müller and Tsong's$^{(39)}$ suggestion that the number of atoms on the surface exposed to an evaporating field may be as much as three orders of magnitude less than the total number of surface atoms. Müller and Tsong$^{(39)}$ used this same technique with tungsten specimens and obtained values of $6x10^8$ layers/sec. The discrepancy between the two values indicates the magnitude of experimental error and emphasizes the need for more experimental and theoretical work.

Another means to determine ν_n experimentally involves using temperature sensitivity measurements and relation (16). The most difficult part in this experiment involves keeping the field constant as the tip evaporates. Using blunt tips helps because as the evaporation occurs the average radius of curvature will not be reduced as drastically as if sharp tips were used. Perhaps an inert gas with a known "threshold ionization field" could be used to provide a means to monitor the field strength at the tip.(40)

Experimental determination of Q_o is achieved also by measuring the evaporation field and the ionic charge. The evaporation field can be determined from relation (10) providing the average field at the tip is known. The applied potential and tip radius are directly related to the average field by relation (11) and can be experimentally measured. The tip radius can be established from transmission electron microscopy(41) (TEM) and scanning electron microscopy (SEM) profiles of the tip and by averaging the local tip radii measured from field-ion micrographs.(42) Tip radii can also be measured from average work functions determined from Fowler-Nordheim plots(22) of $\log(I/V^2)$ vs $1/V$ which yield straight lines whose slopes are proportional to $\phi^{3/2}/F$. Since this field emission technique requires ultra-high vacuum, it usually has limited application with ordinary field-ion microscopes. Although the ionic charge was normally assumed, accurate values of n can be determined currently with the atom probe field-ion microscope. Perhaps if these different experimental means are used to accurately measure the evaporation field and ionic charge, a more reliable measure of Q_o and ν_n can be obtained.

Imaging Gas Effect

Although the previous discussion considers the evaporation to occur in a vacuum, experimental observations are made usually in the presence of an imaging gas. The evaporation field was observed with tungsten to decrease as the helium gas pressure was increased. This effect was more obvious when neon was used. Nishikawa and Müller(43) accounted for this effect by stating that a sufficient probability existed for the imaging gas atoms to penetrate the high field region surrounding the tip without ionizing. When they strike the surface atoms of mass M with an average kinetic energy, $\frac{mv^2}{2} \approx \frac{3}{2} kT + \frac{1}{2} \alpha F^2$, they transfer a considerable fraction, $4mM/(m+N)^2$, of their kinetic energy. This gas impact promotion effect on lowering the evaporation field was formulated by Brandon(32) as

$$\frac{-\Delta F}{F} = \frac{2kT^*}{Q_o} \ell n \frac{\nu^*}{k_e} , \qquad (24)$$

where ν^* is the bombardment rate and T^* is the effective temperature which relates the tip and imaging gas temperatures with the classical accommodation coefficient. Since the bombardment rate is proportional to the image gas pressure, the observed evaporation fields were unchanged, if k_e/p was constant, for various W, Mo and Pt tips.(43) In addition, this imaging gas impact effect was observed to alter the evaporated end form during the transition from a vacuum evaporation and permitted the preparation of uniformly shaped tips. Also, if hydrogen was introduced to the tip, it promoted field evaporation and ionization at a significant reduction in field.(44) Consequently, this hydrogen promotion effect afforded another promising experimental technique to observe nonrefractory metals with the field-ion microscope.

Recent atom probe F-IM results were obtained for the promotion of field evaporation with noble imaging gases and suggest that the gas impact mechanism is insufficient. For instance, the adsorption of the imaging gases(45) and the detection of molecule ions formed from the image gas and surface metal atoms(7,45) was attributed to an electronic rearrangement whereby the binding of the metal atom is reduced when the surface molecule is formed by the overlap of orbitals.(16)

Pulsed Field Evaporation

Pulsed field evaporation is achieved by superimposing a high voltage pulse on the dc image voltage to produce a sufficient field strength to evaporate the surface atoms. This technique is used in conjunction with the atom probe F-IM which measures the time-of-flight for the field evaporated ionic species from the tip to the ion detector. From this value the chemical nature of the ionic species can be identified. The results obtained from the atom probe analysis were not predicted by the previously described field evaporation theory. For instance, unexpected multiply charged metallic ions and their oxide and nitride compounds were identified.(9,11,13) The observation of these higher charged ions appeared to be enhanced significantly when the evaporation rate was increased to 10^9 atom layers/sec. Other significant results include the observation of noble imaging gas adsorption(15,45) and the evaporation of molecular ions formed with the noble image gases and metal atoms.

Pulsed field evaporation was used by Hren et al.(46) to produce images of tungsten at 78°K which contained bright bands of variable width parallel to the <111> zones. The influence of the experimental variables was studied, while the amplitudes of the pulses were adjusted to achieve a constant evaporation rate, for example, when 5 to 10 pulses were desired to remove one (110) plane. A two-mechanism model for field evaporation was proposed to explain the observed difference in the field evaporated end forms. The high field evaporation rates produced a more hemispherical tip, while the slow rates developed an anisotropic-shaped tip.

These reported experimental results for pulsed evaporation rates, particularly the atom probe analysis, indicate that the current theoretical models for field evaporation still need modification. The importance of the field evaporation rate for both the pulsed and dc evaporation techniques prompted Tsong and Müller(34) to develop a detailed procedure for measuring the relative field evaporation rates.

When these proposed methods are tediously followed, fewer discrepancies will exist and the field evaporation theory can become more quantitative.

Atom Probe F-IM Application

Since the experimental observations of field evaporation seem contradictory, the need for more experimental data is obvious. However, the complexity of the field evaporation process requires that sophisticated experimental techniques and intricate instrumentation be developed to gather useful experimental data. The capabilities of the atom probe field-ion microscope(7,45,47) merit its potential application to this particular problem.

The initial accomplishment of the atom probe was the detection of the highly charged metallic ions and their oxide and nitride compounds.(9,10,11) Also, the amount of these unexpected ionic species was observed to increase as the field evaporation rate increased. Another unexpected result was that the noble imaging gases, helium, neon and argon, adsorbed to the metal surface and that their required evaporation field was sufficient to evaporate the metallic atoms simultaneously. Another important observation with the atom probe was the detection of field evaporated molecular compounds(7,14) comprised of the imaging gas and surface metal atoms. Thus, the atom probe appears most useful in obtaining data about the influence of the environment on the field evaporation of surface atoms, particularly on the influence of polarization, solute atoms, the geometric location of atoms, and the presence of imaging gases. The atom probe enables accurate measurement of both the evaporation field and ionic charges of the evaporated species required to make rate sensitivity determinations of Q_o and ν_n. In addition, if the atom probe has an ultra-high vacuum capability, work function values for selected regions of the specimen surface can be obtained and may be correlated to the electronic configuration of the surface.

CHAPTER III

ATOM PROBE FIELD-ION MICROSCOPE

Introduction

Difficulties encountered in identifying the chemical nature of specific surface atoms in an F-IM image served as an incentive for Müller and Panitz(8) to develop the atom probe F-IM in 1967. This instrument is the combination of a standard F-IM and a time-of-flight mass spectrometer. The objective of this instrument is to select and identify individual surface atoms which have been field evaporated. The atomic resolution of the F-IM and the single-atom analysis by the time-of-flight mass spectrometer has created one of the most powerful tools currently available to study the nature of surfaces. For instance, other devices currently being used for surface studies, such as the electron microprobe or the LEED-Auger spectroscope, analyze a minimum of 10^9 atoms.

The principle of operation of the atom probe is illustrated in Figure 5. The specimen is positioned in the atom probe's specimen holder and imaged normally on a phosphorus-coated screen with a central probe hole. By manipulating the specimen holder, the image of an individual surface atom

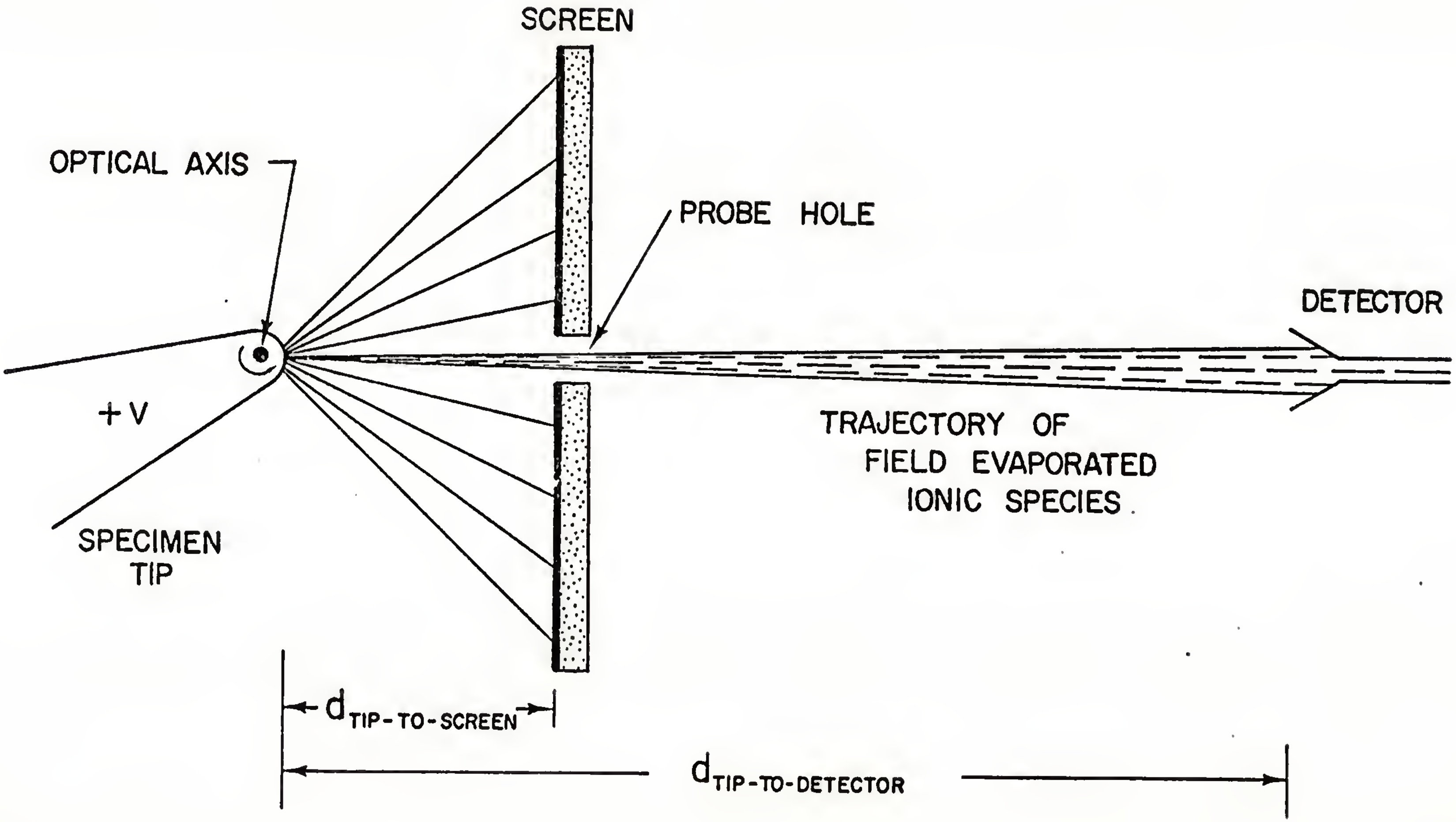
SCREEN
OPTICAL AXIS
PROBE HOLE
DETECTOR
+V
TRAJECTORY OF FIELD EVAPORATED IONIC SPECIES.
SPECIMEN TIP
$d_{\text{TIP-TO-SCREEN}}$
$d_{\text{TIP-TO-DETECTOR}}$

Figure 5. Principle of operation of the atom probe field-ion microscope.

or molecule can be aligned with the probe hole. By superimposing a short time, high voltage pulse on the steady dc imaging potential, the surface atoms can be field evaporated. During the field evaporation process the surface atoms or molecules will lose one or more of their electrons and the resulting ionic species will accelerate radially toward the phosphorus screen. If an entire layer of surface atoms were stripped off during field evaporation, only those ions whose trajectories are aligned with the probe hole would be allowed to enter the drift tube. These ions will travel down the drift tube and strike the detector which also is aligned with the screen's probe hole. By determining the time interval between the initial evaporation pulse and the detector signal, the time-of-flight of the ions can be measured.

Since the ion travels from the tip to the detector in a region essentially at ground potential, its kinetic energy can be expressed as

$$\frac{1}{2} m v^2 = neV \quad , \tag{25}$$

where m and v are the mass and velocity of the ion, n notes the degree of ionization, e is the electronic charge and V is the sum of the high voltage pulse and dc imaging potential, i.e., $V = V_{dc} + V_{pulse}$. Also, the ion reaches its final velocity within a few radii away from the specimen's tip and can be determined from

$$v = d/t \quad , \tag{26}$$

where d is the distance from the tip to the detector and t is the measured time of flight. Units normally used are: kilovolts for V, centimeters for d and microseconds for t. Substitution of (26) into (25) to eliminate v results in the following relations for the mass to charge ratio of the ion:

$$\left(\frac{m}{n}\right) = 2eV\left(\frac{t}{d}\right)^2 \tag{27a}$$

or

$$\left(\frac{m}{n}\right) = 2e(V_{dc} + V_{pulse})\left(\frac{t}{d}\right)^2 \tag{27b}$$

The preceding relations reflect the assumption made that the positive high voltage pulse be superimposed on the dc imaging potential to achieve field evaporation. This method has been supported by Müller, Panitz and McLane,(9,48) Stolt,(49) Tong(50) and Hren and Stoltz.(51) However, another technique that achieves a similar field evaporation effect is reported by Brenner and McKinney.(52) These researchers used a negative voltage pulse applied to an open-ring cathode located in front of the field-ion tip and kept the screen at a potential different from ground. This means that the kinetic energy of the ion is equivalent to only the dc imaging potential, i.e., $V_{dc} = V$.

Although the principles involved with the atom probe F-IM appear relatively simple, the complexity of design, construction and instrumentation, plus the associated expenses have prevented widespread utilization of this instrument for surface studies. Prior to the publication of the current review articles by Brenner and McKinney(52) and Müller and Tsong(11) which describe various technical design and construction problems related to the atom probe, the development and availability of the instrument depended upon the ingenuity of the individual researchers. Consequently, at this time there are only three research facilities in the world which utilize the atom probe.

Several material problems that exist in current F-IM studies appear amenable to study with the atom probe. For instance, work has been initiated for the identification of bright spots in F-IM images attributed to adsorbed gases, deposited metals, self-interstitial atoms, bulk impurities and corrosion products, investigation of short range order and visibility problems in alloys, interpretations of lattice defects and determination of solute atom distribution. From a theoretical standpoint, important data can be obtained to improve current field evaporation theories. In particular, the charge and composition of field evaporated and desorbed species can be determined for single particles.

Technical Design and Material Selection

One of the most important capabilities desired in the atom probe is a bakeable, ultra-high vacuum system. When pressures of 1×10^{-9} Torr and less are obtained, the atom probe can be utilized in both the field ionization and field emission modes. Another vacuum consideration includes the need for a titanium sublimation pump to remove gaseous impurities and to maintain the "clean" surfaces produced by field evaporation. To prevent scattering of the field evaporated ions it is necessary to differentially pump the drift tube below the imaging gas pressure.

The image formation and alignment are critical factors in the atom probe. To provide possibilities for imaging with a wider range of materials and imaging gases, a microchannel-plate image intensifier device is needed. In addition, an optically flat viewing screen, imaging gas ports and observation of the image are required. To improve the image resolution,provisions must be made for cryogenically cooling the specimen and surrounding imaging gases. Utmost consideration must be taken to align the specimen simultaneously with the probe holes in the viewing screen and mirror, orifice of the drift tube and the time-of-flight detector. In addition, to allow selection of individual image spots it is necessary to locate the specimen tip at the center of a goniometer-type assembly that can be tilted approximately 45° and rotated 360°.

The electrical connection for the high voltage dc potential must be well insulated and connected to the high voltage pulse transmission line. Critical impedance matching of the high voltage pulse to the tip is required to provide a well-defined pulse shape and amplitude at the tip.

Since single particle events must be monitored, a very sensitive detector is needed for the time-of-flight mass spectrometer. In addition, appropriate electronic circuitry and a storage facility are required to measure accurate time-of-flights for the field evaporated ions.

In order to obtain a high rate of data collection despite frequent specimen failures, it is highly desirable to provide convenient specimen exchange and rapid pump down to a vacuum below $3\text{x}10^{-9}$ Torr. Also, extra ports must be available for pressure gauges, viewing ports, means to irradiate the tip and means to evaporate material onto the "clean" tip.

The actual construction of the atom probe represented a compromise between the desired design features, material selection and fabrication limitations. In general, any one or a combination of the following materials were used for each component in the completed unit: Type 304 stainless steel, OFHC copper, ultra-pure aluminum, sapphire, glass and gold. Techniques used to fabricate the precision machined components included: gas tungsten-arc welding in protective argon atmosphere, resistance spot welding, high temperature brazing in either air or protective hydrogen atmosphere and electroplating. Following their fabrication, the components were separately cleaned in the following consecutive solutions: toluene, boiling deionized water, acetone, methanol and ethanol alcohol (85 and 99 percent solutions). Ultra-sonic cleaning was utilized when the size of the component permitted. After drying the components with a heat gun, they were assembled in a clean area and all handling was done with protective gloves. During assembly, any open ports were closed to prevent possible dust contamination.

Description of Atom Probe

From the previous discussion concerning the requirements for the atom probe, it becomes evident that each component represents a particular problem in design and fabrication. Consequently, the important components of the constructed atom probe, shown in Figure 6, will be discussed individually in the following order: 1) ultra-high vacuum system, 2) specimen holder, 3) internal microchannel-plate image intensifier, 4) time-of-flight detector, 5) high voltage feedthrough, 6) high voltage supplies, and 6) the electronic circuitry used to measure ionic time-of-flights.

Vacuum System

A metal system comprised of Type 304 stainless steel, with the necessary glass viewports and ceramic high voltage feedthroughs, was designed and constructed to provide a bakeable, ultra-high vacuum system. Figure 7 represents a block diagram of the completed system. Two Varian vacsorb pumps were installed to rough down the system from atmospheric

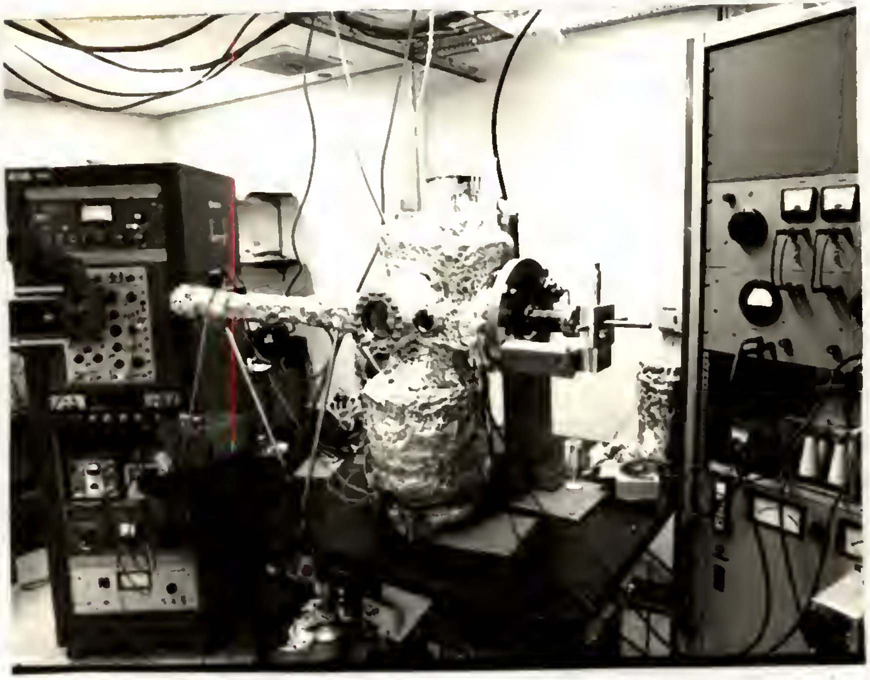

Figure 6. Atom probe field-ion microscope.

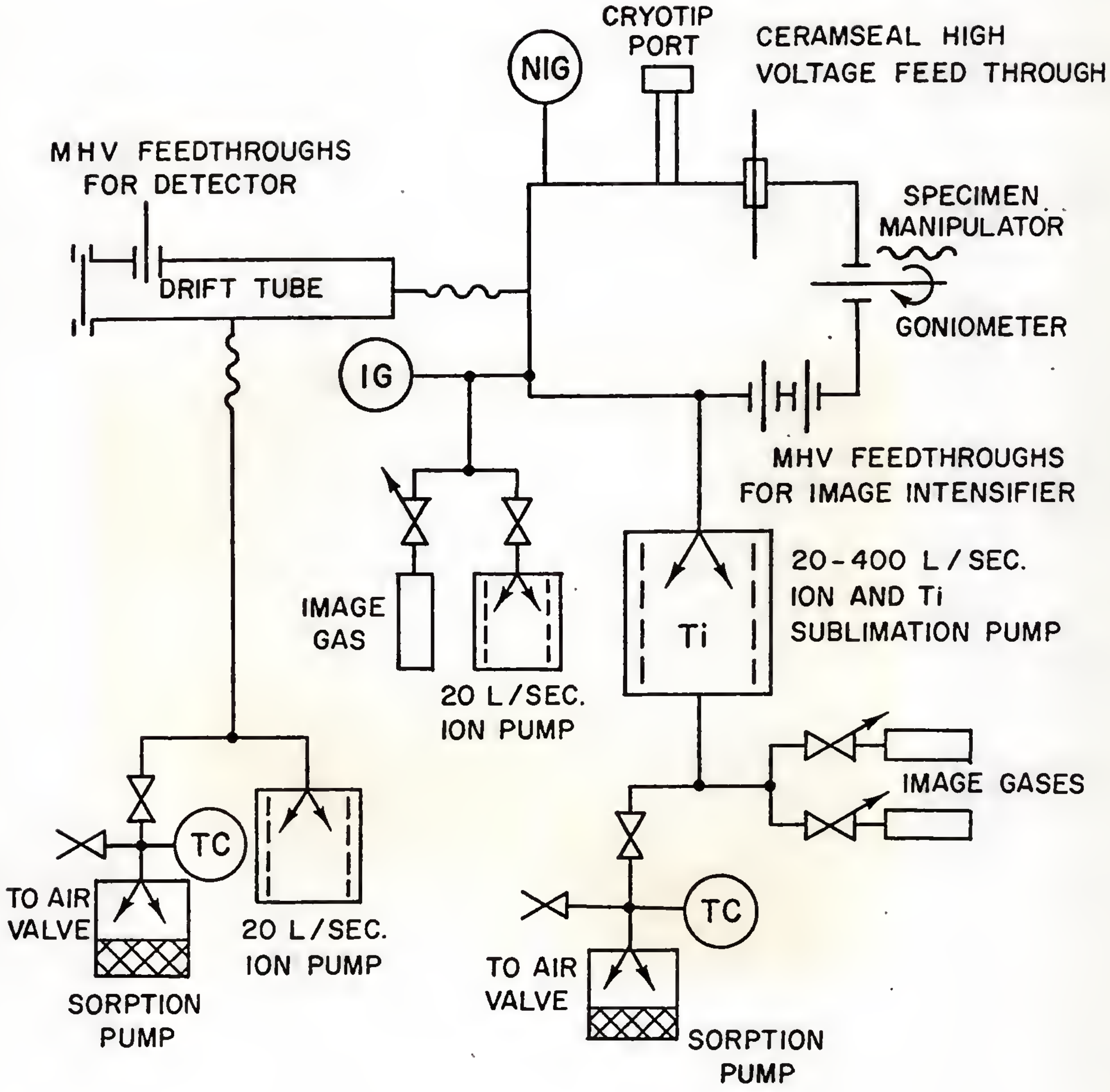

Figure 7. Ultra-high vacuum system for atom probe.

to less than 10 microns pressure. Besides physically adsorbing the gaseous constituents (except inert gases) on the liquid N_2 cooled xeolite, these pumps afforded the advantage of eliminating the backstreaming of a mechanical forepump's oil. Coupled with the vacsorb pumps are four 20 ℓ/sec Ultek DI-pumps. Three of these noble gas ion pumps are located on ports in the atom probe body and the remaining one is located on the drift tube. The three pumps provide maximum pumping speed for the large atom probe body which houses the internal microchannel-plate image intensifier and specimen holder. It must be noted that the 35μ diameter microchannel-plate and the specimen holder's flexible copper cooling cable represent approximately 10 square meters of surface area. Because of this enormous area the three pumps were necessary to insure sufficient pumping capacity to reduce the atom probe body to UHV pressures within a reasonable time. From Figure 7, it is noted that two of the Ultek DI-pumps can be isolated from the system while remaining at UHV pressure. This feature reduced significantly the time needed to pump down the system from atmospheric to UHV pressure.

Once the vacuum system proved capable of reaching pressures in the 10^{-10} Torr range, then it became adaptable for both the field ionization and field emission modes. Since both modes required final specimen tip cleaning by field evaporation and field ionization, necessary design features for imaging were considered. First, it was desirable to keep the drift tube pressure about two orders of magnitude less than the image gas pressure in the atom probe body to prevent scattering of the field evaporated ionic species. To accomplish this differential pressure between the two sections, a 2.8 mm diameter orifice of length 5 cm was machined for the drift tube. In addition, the fourth 20 ℓ/sec noble gas ion pump was attached to the drift tube section as shown in Figure 7. The second consideration for imaging the tip involved the means of introducing the imaging gases to the atom probe body. Three Varian bakeable leak valves were used. Two of these were located purposely so that the imaging gases must pass over freshly deposited titanium before entering the atom probe body. This feature allowed the gaseous contaminants within the imaging gases to be initially gettered by the titanium to reduce their subsequent coverage of the tip. Imaging gas mixtures were possible since the vacuum gauges in the atom probe body allowed monitoring of the partial pressure of each constituent. In addition to introducing imaging gases, the third leak valve can be used to return the system to atmospheric pressure with ultra-pure dry nitrogen. This feature was important for minimizing the time needed to reach UHV conditions after the specimen exchange.

The third important factor of imaging that was included in the vacuum system was the titanium sublimation pump. As reported by several researchers,(7,10,11,52) the titanium sublimation pump provides means to eliminate gaseous contaminants and to maintain the desired imaging gas pressure. From Figure 7 it is observed that the Varian titanium sublimation pump was enclosed in a water-cooled chamber and its 6-inch diameter flange was directly coupled to the atom probe body. Due to this large conductance path a conservative 400 ℓ/sec pumping speed was realized. Once the field evaporated tip has developed a "clean" surface, the titanium pump also provided means to retain its cleanliness when the field was removed and during the time required to reach the necessary UHV pressure for the field emission determinations.

Other vacuum considerations featured in the atom probe include available view ports for observing the image and specimen holder, specimen exchange port, monitoring of atom probe body with milli-torr and nude ion gauges, flexible coupling of drift tube and atom probe sections to alleviate alignment of time-of-flight detector with the precision aligned specimen tip, image intensifier probe holes and drift tube orifice, high voltage feedthrough ports, cryogenic cooling port, extra ports for specimen irradiation and evaporation sources, plus electroplating gold on the interior surface of atom probe body to maintain vacuum cleanliness. In addition, with a special procedure developed for the removal and insertion of the atom probe specimens, routine times of approximately four hours are required to return the atom probe to pressures of 1x10^{-9} Torr and less. This short time actually doubles the number of specimens normally observed, as reported by workers with similar instruments,(7,9,10,16) and emphasizes the efficiency of the vacuum system for the atom probe.

Specimen Holder

Since it is desirable to maneuver any section of the tip's image to the probe hole, the specimen holder must be capable of tilting and rotating the tip while it images. This requirement meant that the specimen holder must provide simultaneously cryogenic cooling, electrical insulation, UHV vacuum conditions and the necessary mechanical manipulation of the specimen tip. This difficult design problem was accomplished initially with the specimen holder shown attached to the support yoke and upper flange in Figure 8(a). Figure 8(b) shows the specimen holder linked to the mechanical manipulator. The physical arrangement of the specimen holder and manipulator is shown schematically in Figure 9.

With the initial specimen holder the liquid hydrogen was poured in the top of the flange into the stainless steel cold finger and passed down through the flexible stainless steel bellows to the specimen holder. In the specimen holder the liquid hydrogen cooled the entire holder and particularly the tip which was mounted in an OFHC copper holder that was intimately secured between a pair of sapphire disks. The

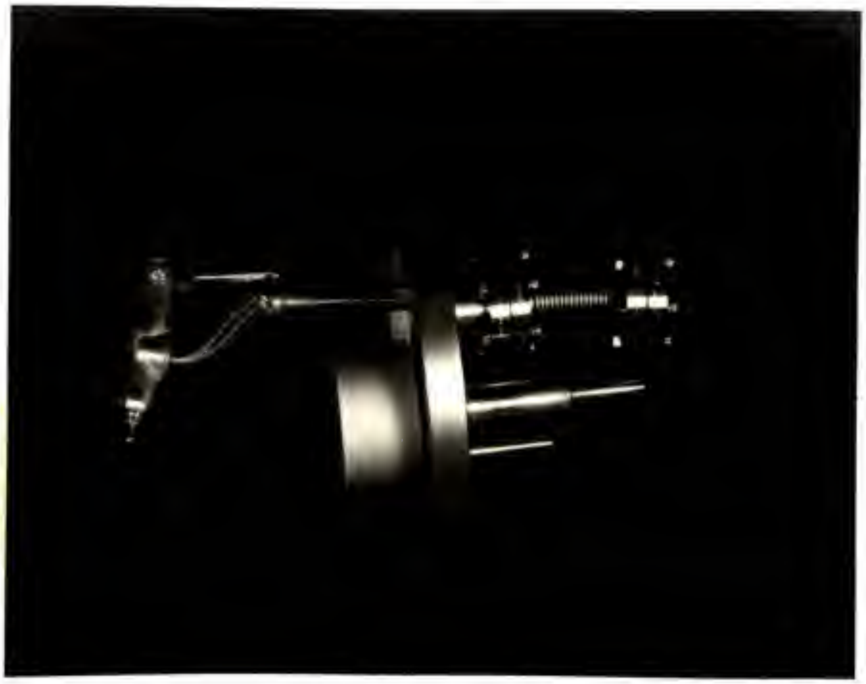

(a) Specimen holder attached to support yoke and upper flange.

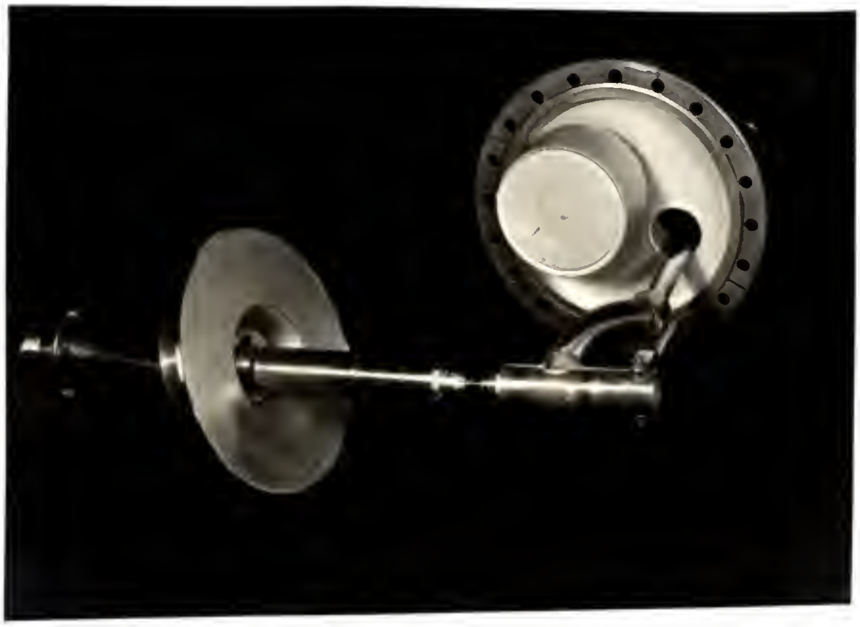

(b) Specimen holder linked to mechanical manipulator.

Figure 8. Initial atom probe specimen holder.

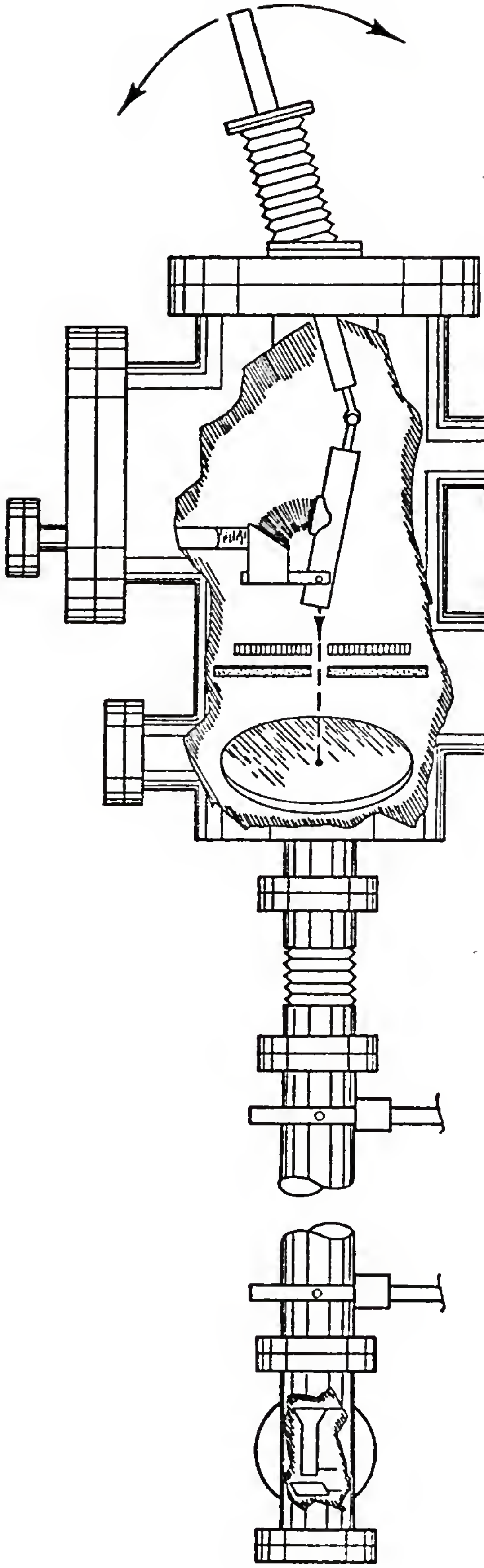

Figure 9. Physical arrangement of specimen holder and manipulator in atom probe.

electrical lead was incorporated into the manipulator assembly with a coaxial cable extending solidly from the power supply to the ball joint. The tip was loaded by removing the entire specimen holder on the large 8-inch flange. To do this the high voltage lead housed in the manipulator rod and ball joint assembly was disconnected from the specimen holder. Once the specimen holder was outside the vacuum chamber, the specimen tip was installed and aligned by optical means to center the tip within 0.3 mm.

Unfortunately, after limited service the stainless steel bellows used for cryogenically cooling the specimen holder developed vacuum leaks. Also, a sufficient amount of stress was developed in the manipulator assembly to fracture the ceramic insulators that shielded the 30 kV dc potential. In addition, the time required to exchange specimens prevented more than one specimen to be examined daily.

Consequently, several design modifications were investigated and tested prior to selecting another workable model. This specimen holder and mechanical manipulating assembly are shown in Figure 10(a) and (b). In Figure 10(a) the stainless steel bellows used to cryogenically cool the specimen holder was replaced with a flexible bundle of gold-plated OFHC copper wires. Attached to both ends of the flexible copper wires were two machined OFHC copper pieces that were brazed with a BAG-19 (silver-copper alloy) in

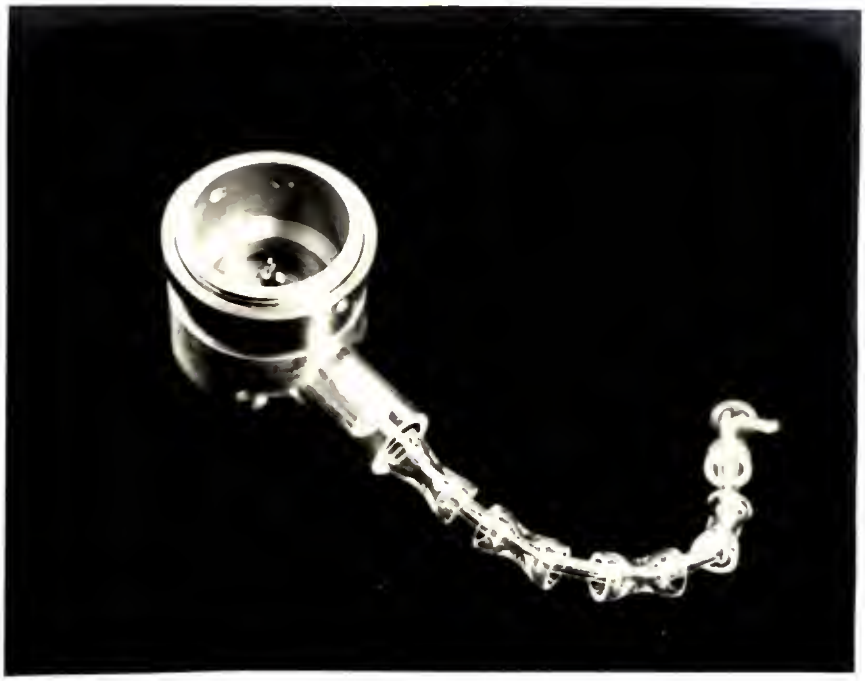

(a) Specimen holder.

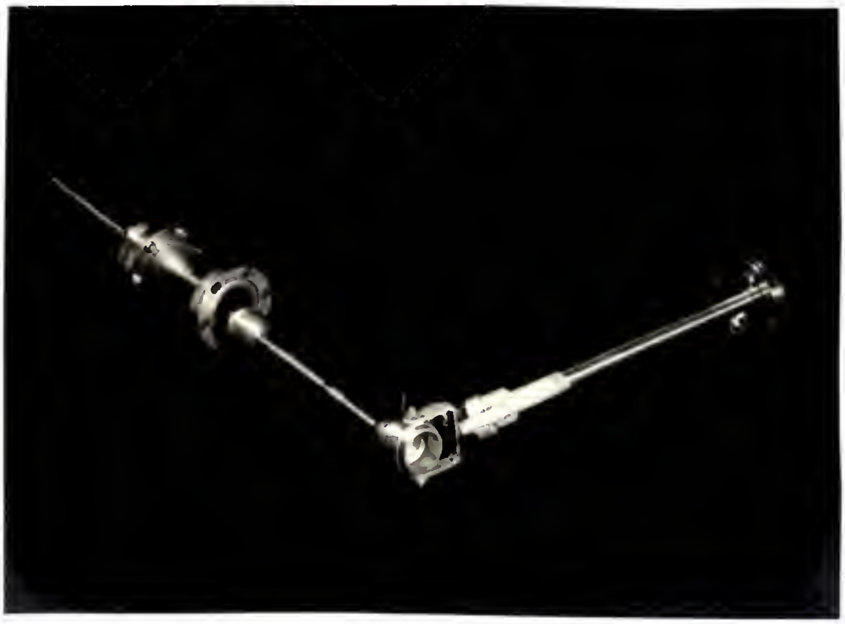

(b) Specimen holder linked to mechanical manipulator.

Figure 10. Final specimen holder and mechanical manipulating assembly.

protective hydrogen atmosphere. These end pieces were fastened with respect to the specimen yoke (OFHC copper) and the specimen holder. Because of the intimate contact of these end pieces, excellent thermal conductance from the stainless steel cold finger to the specimen holder was assured. In addition, if extended manipulation of the specimen holder caused the flexible copper wires to work harden and fracture, another flexible copper bundle with similar machined end pieces can be installed without removing the specimen holder from its precision aligned position in the atom probe body.

The mechanical manipulator assembly was modified to eliminate the weak ceramic electrical insulators. In fact, the new internal slotted tube and outside manipulator rod were machined from stainless steel and were copper brazed in dry hydrogen to the precision machined stainless steel ball joint. Since another ball joint connection was located on the back portion of the specimen holder, the necessary linkage between the ball joint in the outer flange and the specimen holder was provided with a push rod sliding in the slotted tube. Due to the location of the two ball joints, the desired motion of the specimen holder was achieved with a minimum motion of the outside manipulator rod. Vacuum integrity was maintained with a flexible stainless steel bellows..

The high voltage lead was introduced to the specimen holder from a Ceramseal 40 KV vacuum feedthrough. Electrical insulation of this flexible OFHC copper lead was provided with specially designed glass beads. The flexibility of this insulated lead enabled the specimen holder to be tilted a minimum of 45° and rotated 360° by the external manipulator rod while imaging the specimen tip. Precise translational movement of individual image spots to the probe hole was realized with the two-axial micrometer assembly. This aluminum structure was mounted to the large 8-inch end port on roller bearings for easy rotation. Sequentially, the specimen holder is manuevered to a central position and the micrometer stage is clamped. Next, the two micrometers are adjusted to align the desired image spot with the screen's probe hole. Continuity of the coaxial shielding was maintained by keeping the specimen holder and chassis at common ground, while isolating the tip holder and flexible lead. The tip holder was isolated electrically from the specimen holder's shield with 2.5 mm thick sapphire disks. These disks also provide thermal conductance to the tip, since they are in intimate contact with the cryogenically cooled specimen holder.

Another important aspect of this particular specimen holder is illustrated in Figure 11. In this figure one notes that the specimen holder and manipulator rod assembly are biased into a position that faces the small port adjacent to the large view port. This means that the specimen tips can be inserted and removed through this port rather

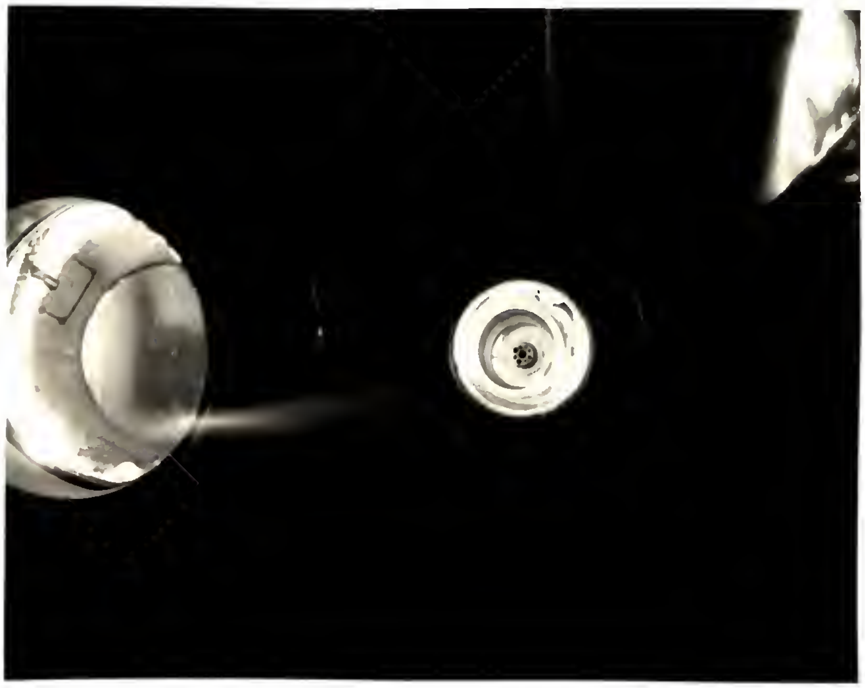

Figure 11. Specimen holder and manipulating rod assembly in biased position.

than removing the entire specimen holder as required previously. The biggest gain in this modification was the reduction in time needed to exchange specimens.

Special care was taken to assure precise tip alignment with the probe holes in the microchannel-plate, screen and mirror and the drift tube orifice. An alignment stand with a flexible stainless steel bellows was mounted on the large upper flange of the atom probe body to support and provide precise alignment of the pivoting specimen holder's yoke. With an optical source located outside the drift tube orifice the specimen tip was positioned within 0.1 mm of the previously aligned probe holes in the microchannel-plate image intensifier and reflecting mirror. Further electronic alignment was undertaken during field evaporation and is described later.

Internal Microchannel-plate Image Intensifier

A microchannel-plate image intensifier was constructed and mounted in the mirror assembly unit located inside the atom probe body. This device improves the observation and photography of the helium-, neon- and argon-ion images plus it affords the possibility of imaging a greater number of materials. Similar devices have been reported by Turner and Southon,(53) Von Oostrom and Manley,(53) Brenner and McKinney(52) and Hren *et al.*(54) Briefly, the principle of its operation is illustrated in Figure 12. The ions

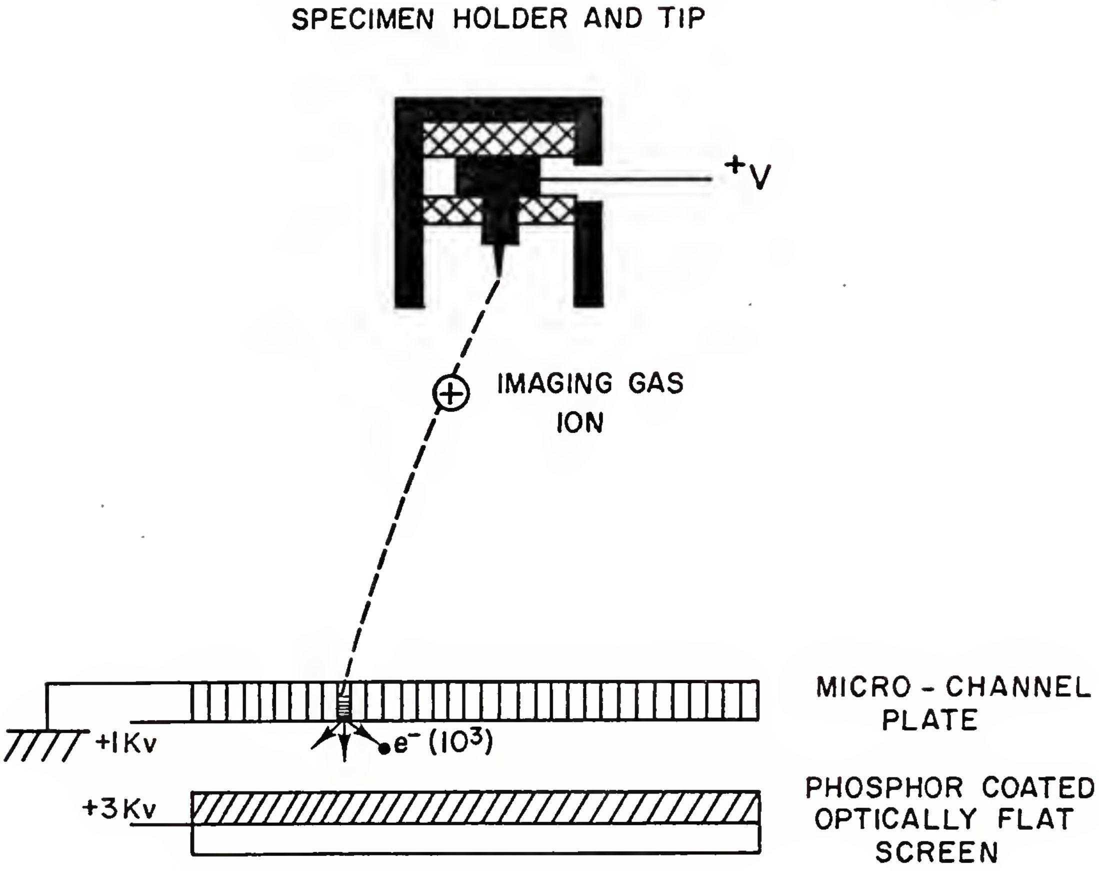

Figure 12. Principle of microchannel-plate image intensifier.

repelled from the specimen tip during field ionization strike the incident surface of the microchannel-plate and generate secondary electrons. These secondary electrons cascade through the individual channels of the plate and are proximity focused onto the ground phosphor screen. Typically, measured gains of 10^2 to 10^3 are reported(55) for these microchannel-plate irrespective of the imaging gas used.

Figure 13 (a) and (b) depicts, respectively, the device schematic and the assembled unit prior to its installation in the atom probe body. The 37.5 micron diameter microchannel-plate and phosphor-coated screen were mounted in a gold-plated stainless steel holder. Four stainless steel bolts fastened the device's components. Electrical insulation was provided for these bolts with precision ground glass cylinders. Because the emerging electrons are proximity focused, the glass insulators were carefully ground to maintain a 1.8 mm separation between the microchannel-plate and phosphorus-coated screen. Hat shaped glass insulators were used to shield the four stainless steel springs needed for supporting the phosphor screen. The high voltage leads extending from the Ceramseal MHV vacuum feedthroughs to the mounted device were insulated with glass to prevent possible arcing when the 1 to 1.2 KV and 3 to 5 KV potentials were applied to the bottom of the microchannel-plate and screen, respectively.

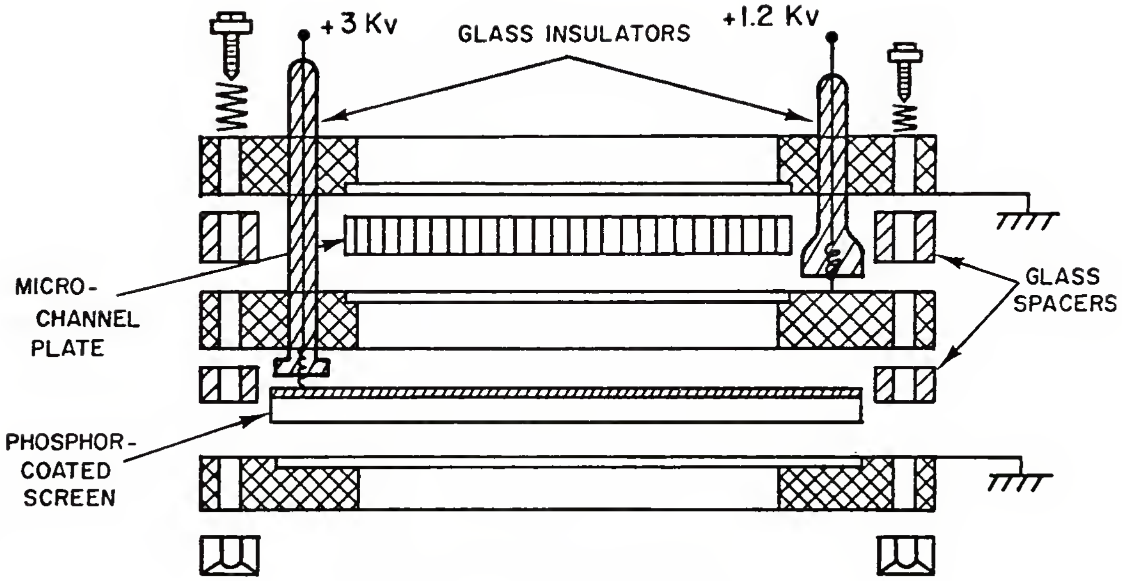

(a) SCHEMATIC DIAGRAM

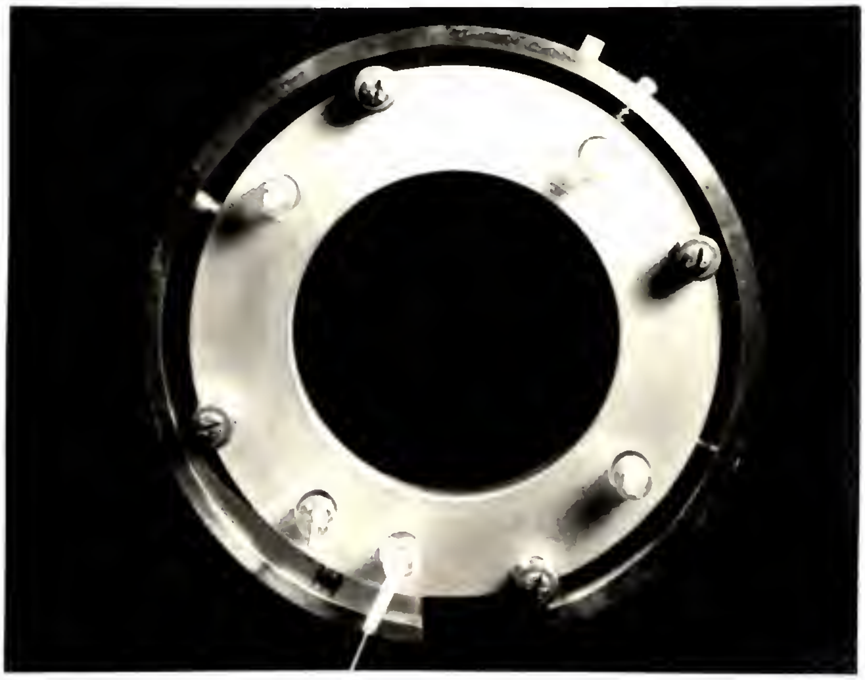

(b) ASSEMBLED DEVICE

Figure 13. Microchannel-plate image intensifier for atom probe.

To assure precise alignment of the centered 1.5 mm diameter holes in the microchannel-plate, phosphorus-coated screen, aluminum-coated reflecting mirror and drift tube orifice, a particular procedure was devised during the device's assembly and mounting in the mirror support assembly. Initially, the 1.5 mm diameter holes in the microchannel-plate and phosphorus-coated screen were aligned with a light source prior to fixing their positions in the holder. Once the holder was tightened, the device was mounted in the mirror support cylinder. Two threaded supports with oppositely positioned spring supports in this polished aluminum cylinder were used to position the probe holes in both this device and the reflecting mirror. Thus, when the light source was located at the drift tube orifice, the holes in the reflecting mirror and microchannel-plate image intensifier could be aligned with respect to each other and the drift tube orifice simultaneously. Following this alignment, the complete mirror assembly was installed in the atom probe body and the movable specimen holder was properly positioned.

Bendix Spiraltron Detector

The detection of either selected field-ion image points or field emission regions is an important requirement for the atom probe. The Bendix Spiraltron electron multiplier was chosen for this function. Bendix(56) developed this detector to be windowless and sensitive to electrons, ions, short wavelength ultraviolet radiation and soft x-rays with the spectral range of 2 to 1,500 Å. Laboratory and space experimental results(57) indicated that these devices have a minimal gain of $5x10^7$ with a 3 KV dc applied potential difference, low background noise, narrow pulse height distributions and low power consumption. In addition, the special semiconducting interior coating of the Spiraltron can be exposed to air when not operating without degradation in performance.

The large conical input aperture (10 mm diameter) of the Bendix Spiraltron CEM-4028 presented a slight accuracy problem in defining the tip-to-detector distance. This uncertainty was reduced to less than 1 mm by tilting the detector 45° with respect to the incident radiation. This tilting, however, reduced the effective input area by 30 percent of its maximum value (perpendicular to incident radiation). The Bendix Spiraltron was housed at the end of the drift tube in a standard Varian tee. The detector was supported by connecting its two nickel leads to two vacuum sealed MHV high voltage feedthroughs. Alligator clips were used to allow optimum positioning of the input aperture with respect to the drift tube orifice, reflecting mirror and microchannel-plate image intensifier probe holes and the specimen tip. A third MHV high voltage feedthrough was connected to an OFHC copper anode that was carefully positioned within 1 mm of the output orifice of the Spiraltron CEM-4028.

The alignment of the Spiraltron's input aperture with the previously aligned probe holes and specimen tip is very critical and influences the detector's efficiency. This alignment was performed initially by optical means. A blank copper gasket with a central 1 mm diameter hole was attached to the input port of the vacuum connection which supported the detector and a light source was positioned behind it. Once the detector's incident aperture was centrally positioned, the Spiraltron's supporting stainless steel flange was rotated 45° and fixed permanently. Next, the tee was attached to the drift tube and a light source was aimed at the 2 mm diameter drift tube orifice from the atom probe body. Since the drift tube was connected to the atom probe body and vacuum roughing lines with flexible metal bellows, the end of the drift tube could be manuevered until the input aperture of the Spiraltron was optimally located. This position of the detector was fixed rigidly with the adjustable support tripods. In the following chapter, the final laser and electronic alignment of the detector and its calibration will be discussed.

Pulse and dc High Voltage Feedthrough

Two primary concerns in designing and constructing this atmospheric high voltage feedthrough were to minimize the uncertainty of the mass resolution of the field evaporated species and to reduce the severity of tip "flashing." In order to reduce the reported uncertainties in the mass resolution,(48) it is desirable to have a square pulse with a very fast rise time and short duration. In general, the time of flight for the field evaporated species is 5 microseconds, so pulse durations of 50 nanoseconds or less are necessary. Also, the rise time of the square pulse signal should be less than 1 nanosecond to preserve its sharp leading edge.

Since the high voltage pulser, Microwave Associates Nanosecond Pulser, is a transmission line type, it was necessary to match its impedance with the high voltage feedthrough circuitry. Consideration was also given to the fact that the line terminated with an open end, the specimen tip, which created reflections up and down the line and further complicated the mass resolution of the field evaporated process. Sharp bends and discontinuities of the transmission line and shielding were avoided to reduce shunt capacities and lead inductances.

The circuitry for this high voltage feedthrough is shown in Figure 14(a). Resistor, R_1, provides the proper impedance termination (50Ω) of the transmission line of the Microwave Associates Nanosecond Pulser. Capacitor, C_1, is a coupling capacitor for the evaporating pulse between the high voltage pulser and the specimen tip. Resistor R_2

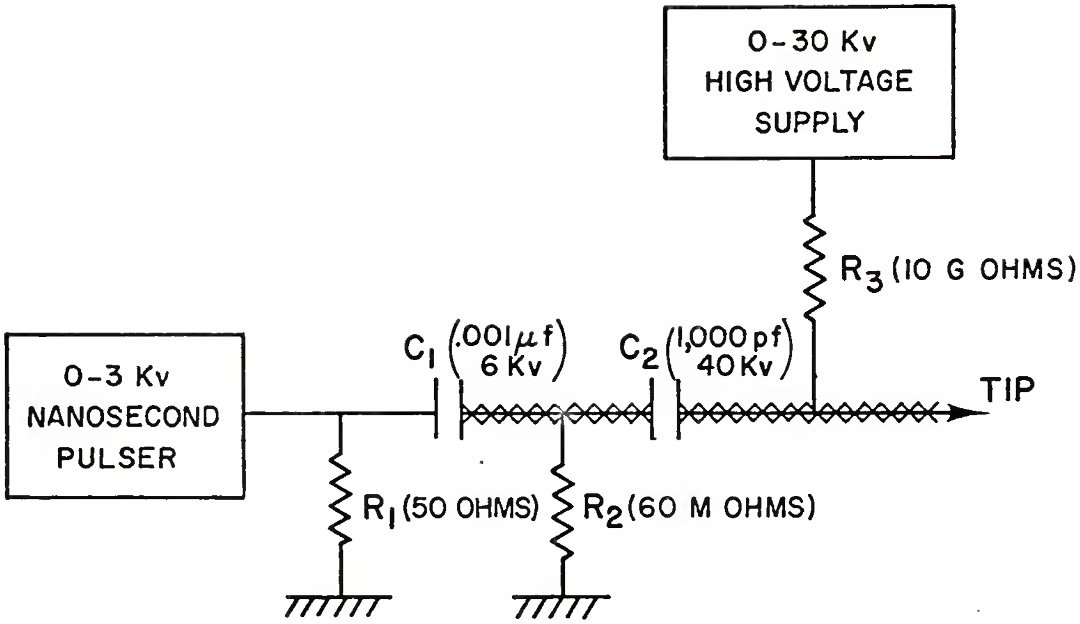

(a) CIRCUIT DIAGRAM

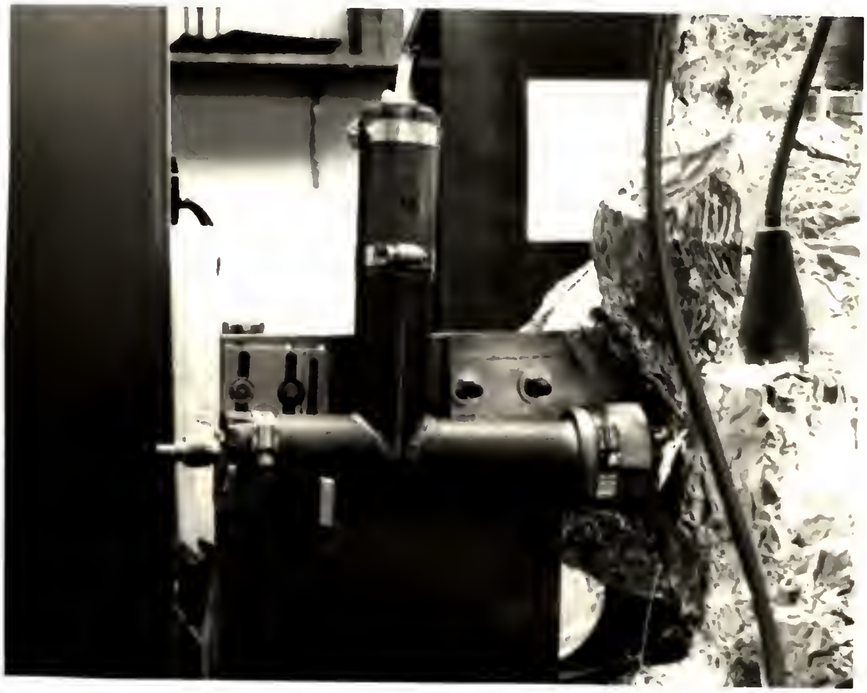

(b) COMPLETED UNIT MOUNTED ON ATOM PROBE

Figure 14. Atmospheric high voltage feedthrough for atom probe.

is included in this circuit to reduce the amount of discharging of capacitor C_2 through the specimen tip upon its "flashing." For instance, if the tip "flashes" the time constant is considerably greater with R_2 since it is determined by multiplying C_2 times the sum of R_2 and the tip resistance rather than just C_2 times the tip resistance. When the tip flashes, the potential decreases and slowly builds up to its initial discharge potential. The time required for this increase is given by $\tau = C_2R_3 = 10$ seconds. Normal operation indicated that this estimated time is conservative. Experimental measurements made with the electrostatic voltmeter indicated a recharging time of 40 seconds.

The primary purpose of the 40 KV, 1,000 pf capacitor C_2 is to isolate the high voltage pulser from the 0-30 KV dc high voltage supply. Resistor R_3 can withstand a 40 KV potential and maintain a 10^{10} ohm resistance. This resistor limits effectively the current available to the tip and diminishes catastrophic "flashing" of the tip. This limited current is equivalent to the applied tip potential divided by R_3 (10^{10} ohms).

Other steps taken to maintain the field evaporation pulse's sharp leading edge and short duration are shown in Figure 14(a). The cross-hatched lines were minimized in length to reduce possible shunt capacitances and lead inductances. Also, the transmission line contained a minimum number of interfaces and sharp bends. The continuous shielding that housed this circuitry was made from OFHC copper and was terminated securely to the atom probe body. Since this feedthrough must be capable of withstanding potentials of 30 KV in atomsphere, it was necessary to line the interior surface of the copper tee with acrylic tubing plus construct special high voltage connectors insulated with Teflon to prevent discharging. Other features of this component include: quick connect and disconnect coupling with the UHV Ceramseal 40 KV feedthrough, unit can be easily removed while baking out atom probe body, and provisions for exchanging the electrical components to achieve maximum restoration of the incident high voltage pulse at the tip. The completed unit is shown attached to the atom probe body in Figure 14(b).

High Voltage Power Supplies

Generation of high voltage square pulses with durations less than 50 nanoseconds can be accomplished by at least two methods.(52) After evaluation, it was decided to purchase the commercially available Microwave Associates Nanosecond Pulser. This particular model 961E produces square high voltage pulses by discharging a transmission line into the output line with a mercury switch. The electrical pulses are produced with an impedance level of 51 ohms either manually or at a repetition rate of 60 cps. Primary positive features of this supply(52) include: a positive square pulse shape with a half nanosecond rise and fall time and an adjustable width of 2 to 20 nanoseconds; pulse amplitude range of 0 to 3,000 volts with a jitter of less than 4 percent; and a simultaneously produced trigger pulse with an amplitude of about 2 percent of the high voltage pulse; and either a positive or negative leading edge with a half nanosecond rise time. Although the mercury-wetted switch is asynchronous,(52) the trigger pulse has sufficient energy to initiate the horizontal sweep of the Tektronix 549 Storage Oscilloscope used in the electronic circuitry to identify the field evaporated species.

The dc high voltage for imaging the specimen tip was provided with a Kilovolt Corporation's Model KVR30-1S. This particular power supply produces a highly regulated positive or negative dc potential that ranges from 0 to 30 KV. Following an initial 30-minute warmup, the stability is within 0.01 percent per day. A high voltage electrostatic voltmeter was used to determine the deviation of the indicated potential and the actual output value. No deviation was measured up to the 10 KV limit of the voltmeter.

Electronic Circuitry

To reduce the uncertainty in measuring the m/n (i.e., mass to charge) ratios of the field evaporated ionic species, it was necessary to obtain the best possible resolution for the individual displays of the Tektronix Type 549 Storage

Oscilloscope. Noticeable improvement was obtained when a preamplifier was located adjacent to the collector of the Bendix Spiraltron detector. This unit was designed and constructed to minimize shunt capacitances and lead inductances associated with the collector and coaxial leads to the storage oscilloscope. A schematic diagram of this preamplifier is shown in Figure 15. Physically, this integrated circuit board was mounted in a solid copper box. All the MHV feedthroughs were soldered to the copper box to assure proper termination.

After completion the preamplifier was tested to check its performance. The output signal had a characteristic 50 ohm impedance which was consistent with the remaining circuitry. Generated square wave pulses were sent through the preamplifier and the resulting oscilloscope traces indicated that the output pulses retained the leading sharp edge and duration of the incident signals without evidence of ringing. The amplitudes of the output pulses, however, were reduced by approximately 10 percent.

The individual electronic components of the atom probe were arranged as shown schematically in Figure 16 to form the control circuitry for identifying the evaporated species. With this arrangement the field evaporation pulse and trigger output pulse are initiated simultaneously from the Microwave Associates Nanosecond Pulser. The high voltage pulses ranging from 100 to 3,000 volts with two or twenty

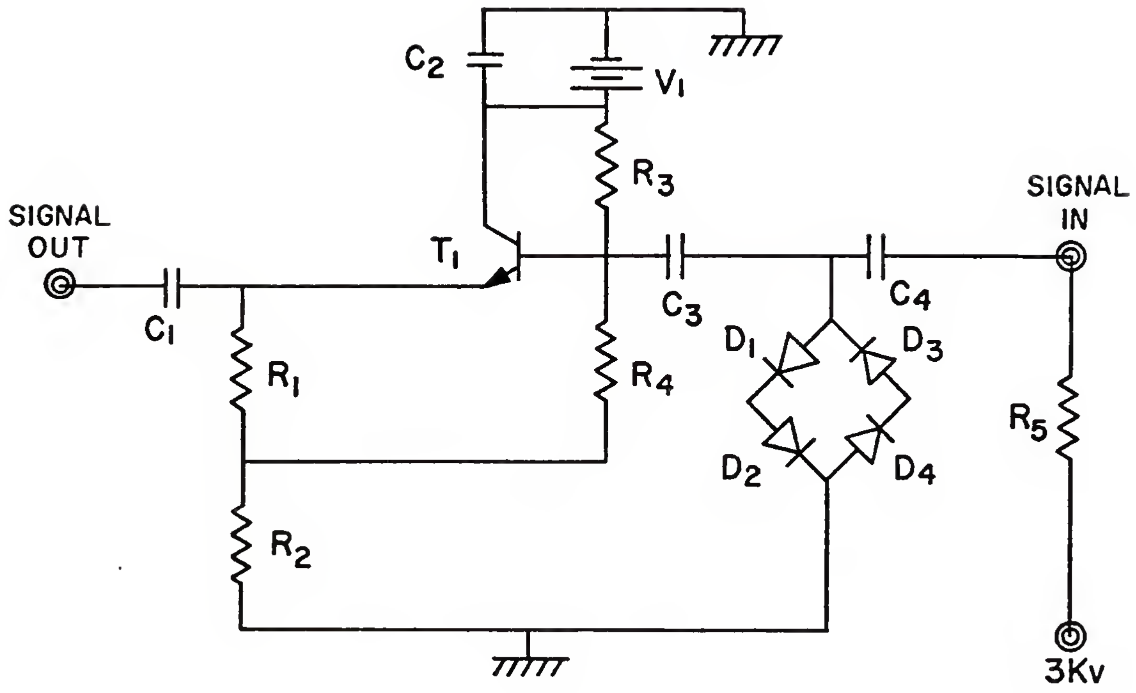

R_1: 100 OHMS
R_2: 100 OHMS
R_3: 100 K-OHMS
R_4: 220 K-OHMS
R_5: 1 M-OHM
V_1: 9 VOLT BATTERY

C_1: 0.1 μf 100 VDC
C_2: 0.01 μf 35 VDC
C_3: 0.1 μf 100 VDC
C4: 0.001 μf 6 Kv
T_1: 2N930
D_1, D_2, D_3 & D_4: 5A6-D

Figure 15. Circuit diagram of preamplifier.

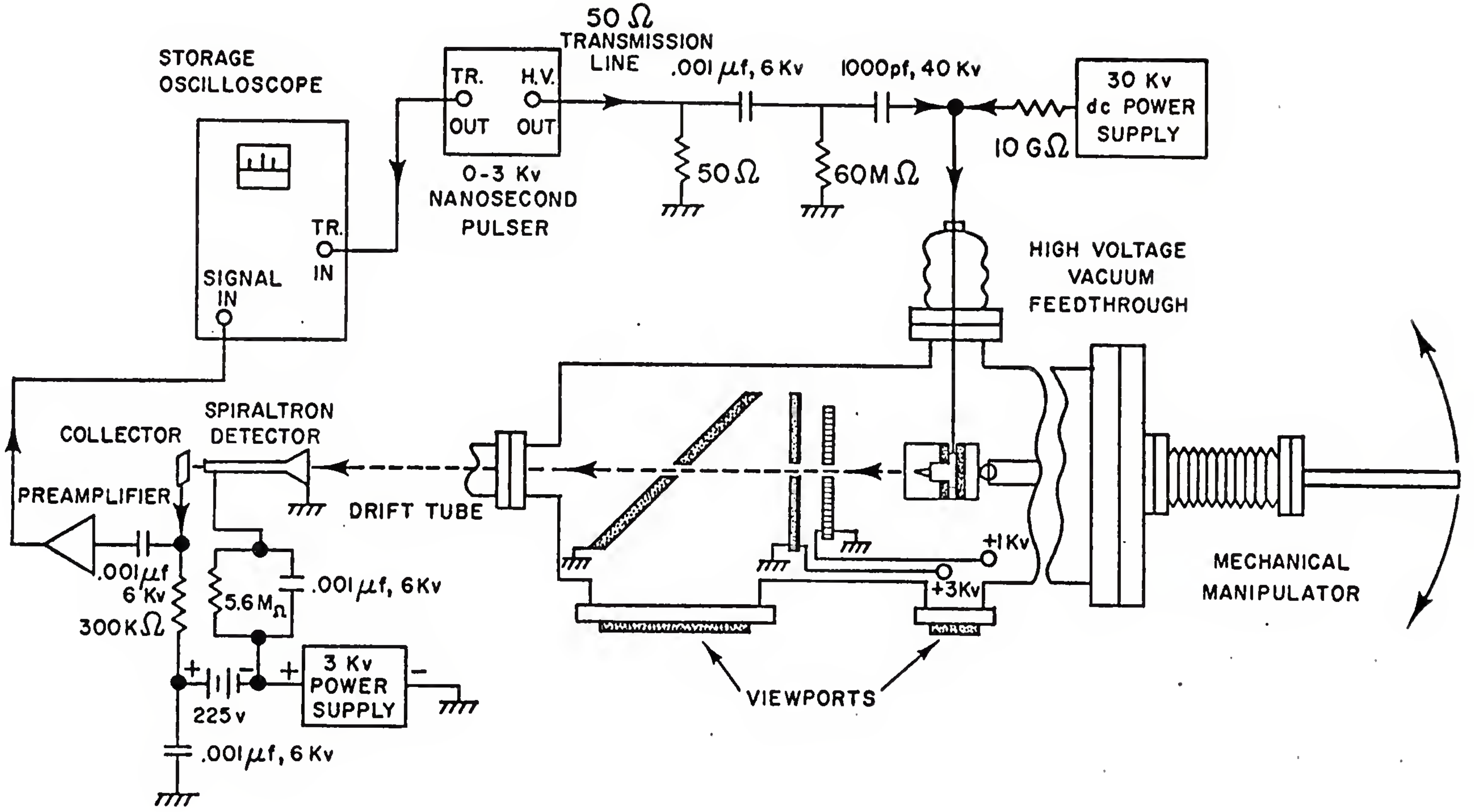

Figure 16. Detection circuitry for atom probe.

nanosecond durations are transmitted from the Microwave Associates Pulser through the pulse circuit section of the high voltage "tee" feedthrough to the tip. Meanwhile, the dc high voltage signals travel through the 10^{10} ohm resistor in the high voltage "tee" feedthrough and are coupled to the high voltage pulses before reaching the specimen tip.

The trigger output pulse in the meantime is sent by a short coaxial transmission line to the oscilloscope where it initiates the horizontal sweep. The following procedure was used to determine the necessary oscilloscope settings for identifying the ionic species. The delay time multiplier of the oscilloscope can be adjusted to produce a full spectrum display of the expected evaporated species. This is accomplished by first setting the desired width of the spectrum on the A sweep time/cm control. Next, the expected time of flight for the fastest species is divided by the setting on the B sweep time/cm control. By putting this value on the Delayed Time Multiplier the beginning of the spectrum is located at the left edge of the screen. For example, suppose a normal time spectrum extends from 5 to 6 microseconds. The width of the screen represents 1 microsecond, so the A sweep time/cm dial is set at 0.1 microsecond/cm, nonmagnified. To begin the time flight display at 5 microseconds the B sweep time/cm is set at 2 microseconds/cm. By dividing this value into the expected time of flight for the fastest particle, one obtains

$$\frac{2\ \mu sec/cm}{5\ \mu sec/cm} = 0.40$$

which is set on the Delay Time Multiplier.

To distinguish the mass resolution of an expected individual ionic particle from others in the spectrum, one subtracts half the length of the A sweep time/cm from the expected time of flight and divides this value by the setting on the B sweep time/cm dial. This value is then set on the Delay Time Multiplier. For instance, if the evaporated specie's expected time of flight, calculated from relation (3), is 5.2 μsec, the A sweep time/cm switch is set at 0.1 μsec/cm, magnified. This gives a screen width of 0.2 μsec. Half of this width is 0.1 μsec. Subtracting 0.1 μsec from the expected time of flight, 5.2 μsec, results in 5.1 μsec. Dividing 5.1 μsec by the 2 μsec/cm B sweep time/cm setting gives 2.55 which is set on the Delay Time Multiplier. This arranges the spectrum so the expected 5.2 μsec event will be recorded at the center of the screen.

From the control circuit, Figure 16, one observes that the field evaporated surface atoms aligned with the 1.5 mm probe holes in the microchannel-plate intensifier and screen pass through the drift tube orifice, travel the length of the drift tube and strike the Bendix Spiraltron detector. To avoid possible divergence of this trajectory, the applied potentials on the microchannel-plate image intensifier are removed prior to the pulsing. When each of the ionic species strike the Spiraltron, the produced secondary electrons are accelerated with a +3 KV potential to the end of the detector. A positive 225 potential is used between the detector's output and the collector to prevent significant path divergence of the emerging electrons. From the collector the signal passes through a short lead to the preamplifier and along a coaxial line to the input of the Type 549 Tektronix Storage Oscilloscope. After each pulse, the trace position is relocated on the storage oscilloscope until the accumulated individual signals completely fill the storage screen. These are photographed and the individual signals identified.

CHAPTER IV

ATOM PROBE CALIBRATION

Introduction

After the atom probe F-IM was assembled and its vacuum capabilities determined, it was necessary to calibrate the instrument and evaluate the performance of the individual components. Since so many components and different functions were evaluated, the procedures and results will be discussed separately. For instance, the specimen holder, high voltage feedthrough,microchannel-plate image intensifier and Spiraltron detector will be discussed in the component section, while the observed defocusing effect, detector efficiency and mass resolution will be described in the operational performance and calibration section.

Performance of Individual Components

Specimen Holder

Since the specimen tip must be precisely positioned within 0.3 mm of the optical axis, it was necessary to initially align the center of the specimen holder's support yoke with the probe holes in the microchannel-plate, phosphor-coated screen and drift tube orifice. The arrangement of these components was shown in Figure 16 in the previous chapter. This was accomplished by placing a high intensity light source at the end of the drift tube and maneuvering the yoke with the adjustable support assembly until the centrally positioned crosshairs on the yoke coincided with the center of the light beam passing through the 1.5 mm diameter probe holes. After the support assembly was rigidly fixed, the specimen holder was installed by carefully adjusting the support bolts to assure the centers of the specimen holder and yoke coincided. After the specimen holder was attached, the glass-insulated, flexible copper high voltage lead was connected to the Ceramseal high voltage vacuum feedthrough. Finally, the ball joint was fixed to the specimen holder and connected to the push rod. After the push rod assembly was positioned properly to allow the specimen holder to rotate to its biased position, it was guided into the slotted manipulator rod which in turn was fixed to the atom probe end flange.

The atom probe body was evacuated to the 10^{-3} Torr range and high voltage was applied to determine the effectiveness of the specimen holder's electrical insulation. This pressure was selected because it represents the highest possible image gas pressure used during operation. As the dc potential was carefully applied to the specimen holder, observations were made to detect possible voltage breakdown.

Up to 15 kV no visible breakdown occurred. Between 15 and 24 kV, small discharges were observed, but after repeated discharging at a particular position and potential they would disappear. Apparently, sharp surface asperities of dust and surface conductance caused these discharges and with repeated discharging "healed" themselves. Testing was discontinued at 24 kV, since this would be the maximum dc potential normally applied to the specimen tips. Also, the operational imaging gas pressure for the atom probe does not exceed $1x10^{-5}$ Torr and this two-order improvement in vacuum will allow a conservative 30 percent increase in the effectiveness of the electrical insulation.

Cryogenic cooling of the specimen holder was achieved by connecting the OFHC copper cooling block to the specimen holder with a firmly attached bundle of flexible 0.75 mm diameter copper wires. Due to the amount of copper wire in the bundle and the minimal heat conductance losses, the tip temperature is less than 2°K above the cryogenic coolant's temperature. If the specimen tip temperature needs to be monitored during field evaporation studies, platinum or carbon thermocouples can be attached to the electrostatic shield of the specimen holder. By prior correlation of this thermocouple's temperature with the temperature of a similar thermocouple mounted at the tip position, a reasonably accurate description of the specimen temperature is achieved. After the initial cooling of the specimen holder, the cold finger will maintain liquid nitrogen temperature for at least 30 minutes before being refilled.

In order to replace the specimen tip the following procedure was found to be the most efficient. The heating tapes were turned on prior to introducing ultra-pure nitrogen to the atom probe. After the atom probe reached a minimum of 160°C and its pressure reached 1 atmosphere, the view port was removed and the specimen holder was maneuvered to its biased position, as shown in Figure 11 in the previous chapter. The copper piece that contains the specimen tip is removed from the specimen holder and the new specimen is carefully installed. After the specimen holder is returned to a position facing the microchannel-plate, the view port is replaced and the bakeout temperature increased to 280°C. After 10 to 15 minutes, the system is evacuated by standard vacuum methods. Repeated specimen exchanges indicate that four to five hours are required to return the atom probe to less than 1×10^{-9} Torr.

It is essential that the rotating specimen tip remain axially aligned with the probe holes and Spiraltron detector, as the individual atomic sites are translated to the probe hole. To accomplish this the optical axis position in the specimen holder was determined. In particular, the distance from the end of the tip to the bottom of the copper mounting sleeve must be positioned within 0.001 cm. This distance must be ascertained prior to crimping the tip securely into the copper sleeve. In order to assure the tip will be aligned within 0.3 mm of this axis, the mounted specimen is inserted in an exact duplicate of the specimen holder's hat. This unit is then rotated slowly and the tip position adjusted to its center of rotation. Following these mechanical alignments the tip is observed optically to check for possible bending or breaking.

The rotational range of the specimen holder is best illustrated by Figure 17. In this figure the probe hole is positioned on the (110), (111) and (112) planes of a tungsten tip imaged in a helium-10 percent neon mixture with an applied potential of 8.5 kV. If the average tip radii had been larger the (100) plane could also be rotated to the probe hole center. The angular motion of the specimen holder is easily controlled within a few tenths of a degree by careful translation of the manipulator rod with the two micrometers mounted in the goniometer stage. During atom probe analysis the desired region of the specimen surface is located first and if the analysis of individual atomic sites are desired, these image spots are translated to the center of the probe hole.

High Voltage Feedthrough

Another important factor in the atom probe performance is an accurate measure of the applied dc potential at the tip. To establish the uncertainty of the dc potential at the tip the high voltage feedthrough was connected to the

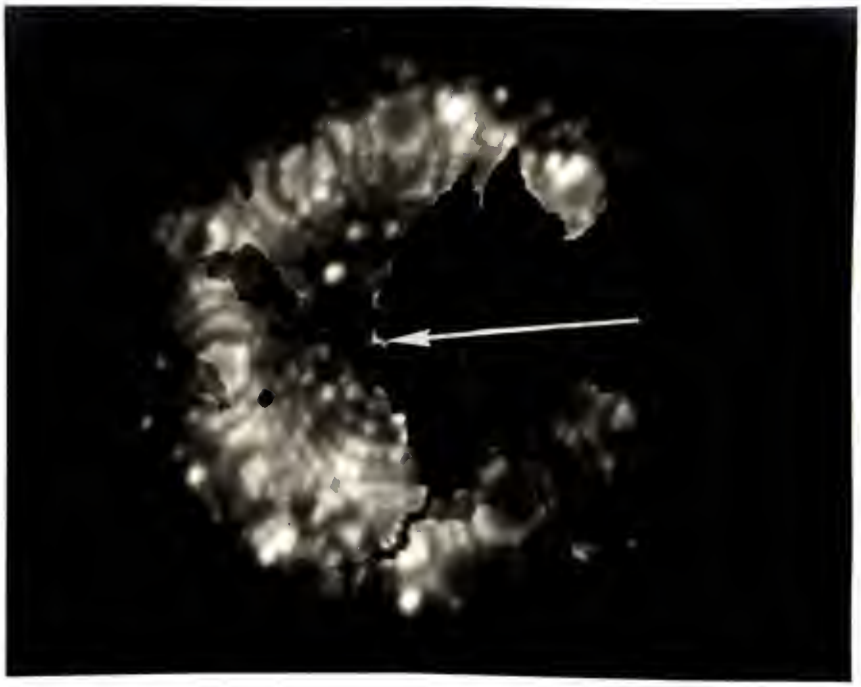

(a) Probe hole positioned on (110) plane.

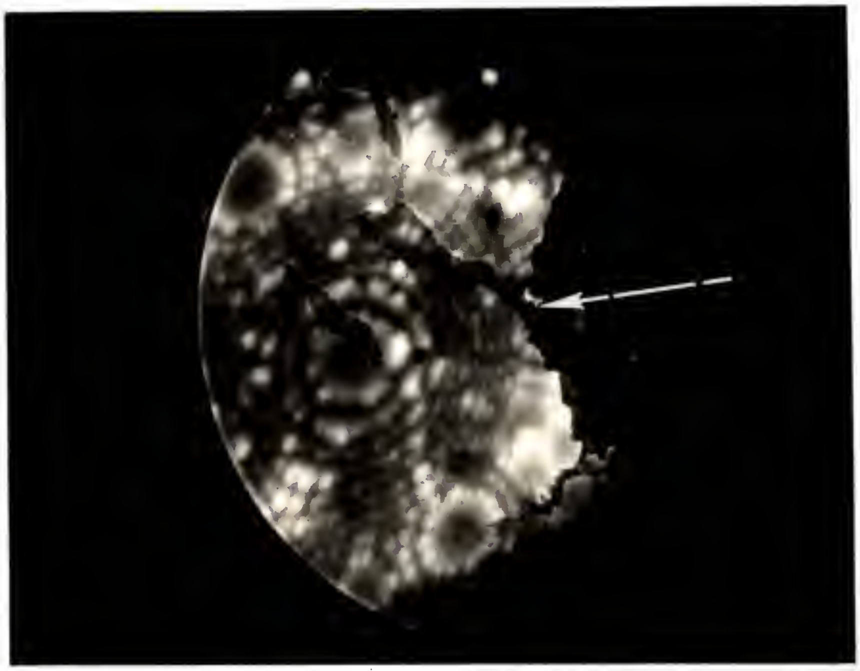

(b) Probe hole positioned on (111) plane.

Figure 17. Specimen manipulation provides observation of nearly entire surface of tip.

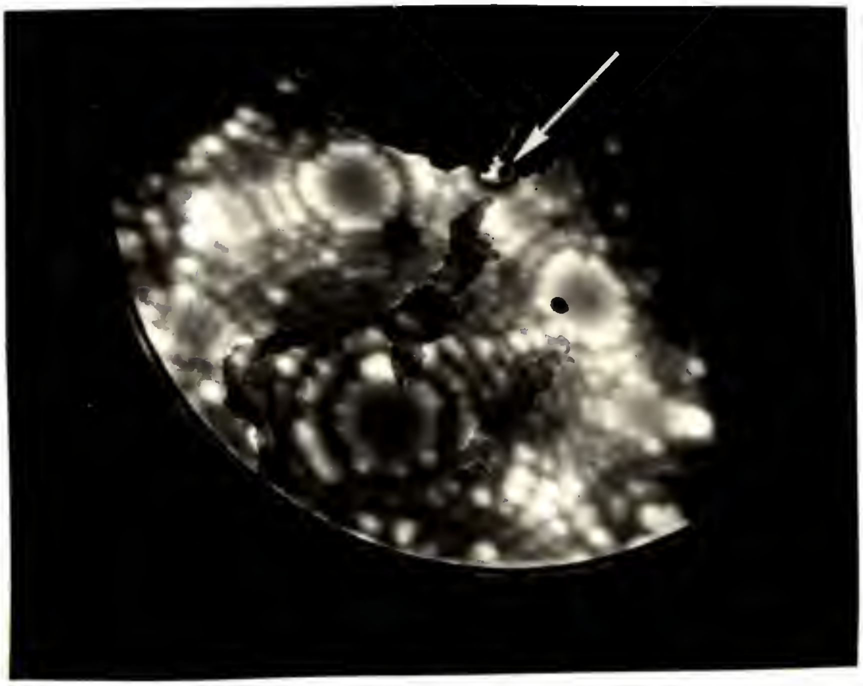

(c) Probe hole centered on (112) plane.

Figure 17. (cont.)

atom probe and a high voltage electrometer was connected to the tip position. Calibration was conducted by comparing the applied dc potential to the potential measured at the tip position. From zero to 10 kV the high voltage dc supply and the measured tip potential appeared identical. Calibration of higher potentials was not possible due to the electrometer limitation; however, deviation from the extrapolated results would be less than 0.1 percent, based upon the stability of the high voltage supply.

Another concern for the high voltage feedthrough was its capability to withstand potentials above 10 kV at one atmosphere. The applied potential was increased slowly to 24 kV to test for possible high voltage discharging. Although small discharges occurred above 20 kV, these were quickly "healed" and the dc potential remained steady. Also, at the 24 kV dc potential the pulsing portion of the feedthrough circuitry was adequately protected by the high voltage blocking capacitor, C_2, as shown in Figure 14(a).

Microchannel-plate Image Intensifier

Initially, the microchannel-plate image intensifier was tested for possible electrical breakdown. The gas pressure of the atom probe was again maintained at 10^{-3} Torr and the applied positive potential was slowly increased to 1.2 and 5 kV for the microchannel-plate and phosphor-coated screen respectively. No electrical discharging was observed with repeated application, so the glass-insulated assembly appeared satisfactory. Next, the atom probe was evacuated to less than $2x10^{-9}$ Torr and a tungsten specimen was imaged in the field emission mode. With the appropriate potentials applied to the intensifier a bright image resulted. Also, it was observed that the pressure increased to $7x10^{-9}$ Torr. Apparently, there remained gaseous species in the optical fibers of the microchannel-plate after the atom probe bakeout and upon electron excitation these were outgassed. After two hours, the system pressure was in the 10^{-10} Torr range and the field emission image appeared much sharper in contrast.

Image formation parameters were established for the microchannel-plate image intensifier for helium, neon and helium-neon mixtures. In particular, the applied positive potentials to the microchannel-plate and phosphor-coated screen were varied to establish the best image for the different imaging gases. For example, no image intensification was evident unless 600 volts were applied to the microchannel plate. If the potential exceeded either 950 volts at $1x10^{-6}$ Torr image gas pressure or 900 volts at $1x10^{-5}$ Torr gas pressure, the resolution of the image diminished. Since the image intensifier depends on proximity focusing of the secondary electrons emitted from the microchannel-plate, it was necessary to establish the best focusing potential for the phosphor-coated screen. Visual observation indicated that the optimum image resolution was obtained at 3.5 kV. Noticeable improvement in the observed images was obtained with the helium-10 percent neon mixture. This particular composition afforded improved atomic resolution over both the elemental gases and confirmed recent results reported by Chen and Seidman.(58)

Spiraltron Detector

In order to predict the sensitive area of the specimen tip that can be analyzed by the Spiraltron CEM-4028 detector, it was necessary to determine the following geometric factors for the atom probe. First, it was necessary to measure the listed distances: tip-to-microchannel-plate, 86.9 mm; tip-to-screen, 88.9 mm; tip-to-mirror, 122 mm; and the tip-to-detector, 100 cm. Since the tip-to-detector distance was determined within 1 mm the uncertainty for this parameter for the time-of-flight measurements is 0.1 percent. With the above distances and the diameters of the microchannel-plate (1.5 mm) and Spiraltron orifice (10 mm), it was calculated that the specimen tip must be located within 0.3 mm of the optical axis to allow the field evaporated ionic species to strike the Spiraltron cone. In addition, it was noted that the sensitive area of the tip to be analyzed was not limited by the probe hole diameter, but by the size of the incident aperture of the Spiraltron. Brenner and McKinney(52) estimated this value from the following relation

$$A_T = A_D\left(\frac{R_T}{R_D}\right)^2 \beta^2 \tag{28}$$

where A_T is the sensitive area of the tip, A_D is the area of the detector incident aperture, R_T is the tip radius, R_D is the tip-to-detector distance, and β is an image compression factor dependent upon the tip geometry and usually ranges from 1.5 to 1.8. Substituting appropriate values for the atom probe, the sensitive tip area ranges from 31.4 to 50.2 Å^2 with respect to assumed tip radii of 400 and 800 Å. This A_T value indicates that the number of atoms analyzed from a surface will depend upon their crystallographic orientation. For instance, if the atoms are in the (110) plane, four could be analyzed, whereas if they were located in the (111) plane, only two could strike the detector.

The Bendix Spiraltron CEM-4028 can be operated in either the analog or pulse counting modes. The analog current mode, illustrated in Figure 18, was used to measure both the ion and electron currents depending upon the selected atom probe's mode of operation, i.e., field ionization or field emission. Schmidt(56) reported that the CEM-4028 was linear in operation for output currents below approximately 10 percent of the bias current, i.e., ($V/10^9 \times 0.1$) amps, where V is the applied potential. Examination of the analog circuitry indicates that the measurement of both types of currents (electron and ion) requires an appropriate

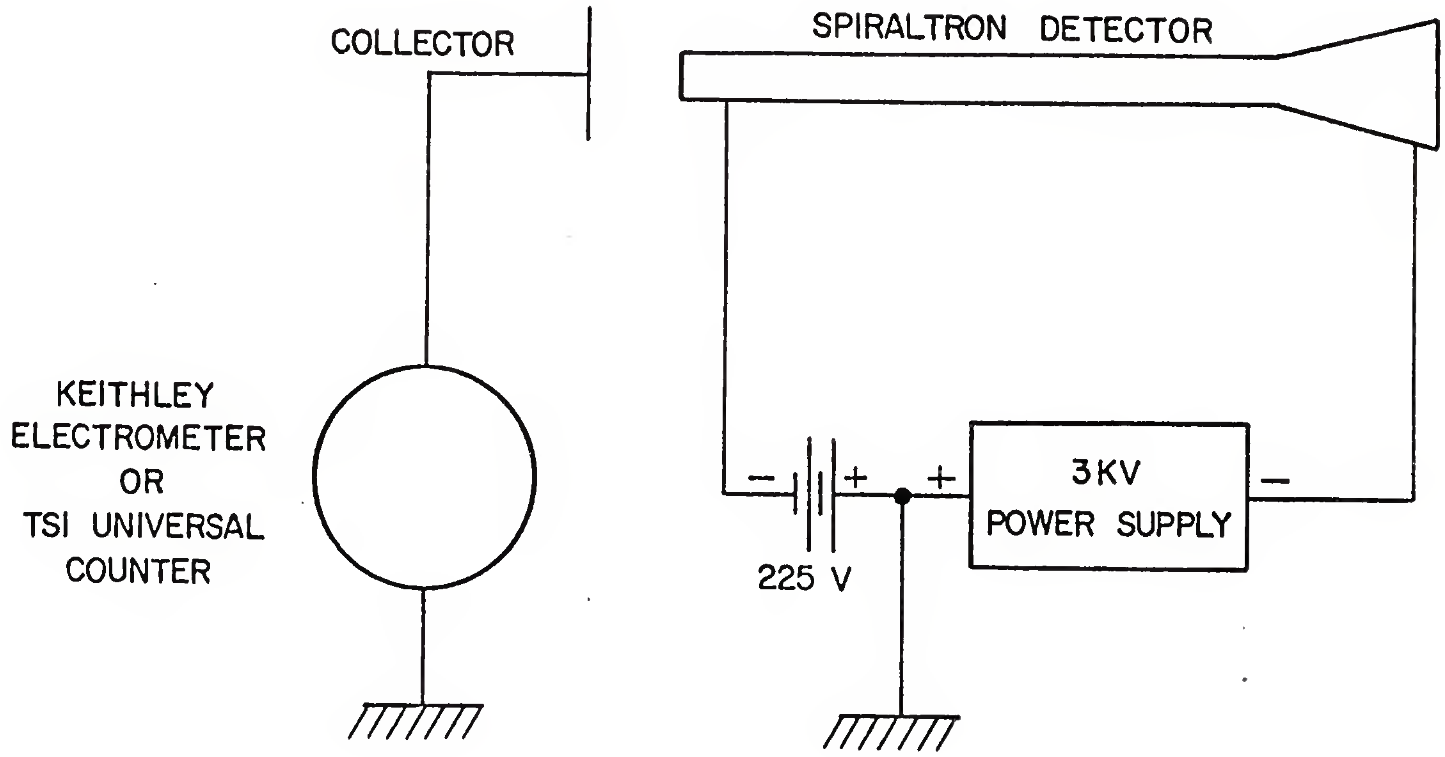

Figure 18. Analog mode circuitry for Spiraltron detector.

selection of polarity input and output apertures and maintenance of a 225 volt bias between them and the output orifice and the collector. The pulse counting mode, refer to Figure 16 Chapter III, is used primarily for the time-of-flight measurements. Results from this mode will be discussed later.

Prior to performing the final electronic alignment of the Spiraltron with the tip position, it was necessary to determine the best operational parameters for the Spiraltron's two modes of operation. The analog mode was analyzed with an iridium tip imaged at 10 kV with a neon gas pressure of 5×10^{-4} Torr. The resulting ion current was detected by the Spiraltron that was differentially pumped in the drift tube to 5×10^{-7} Torr and recorded by a Keithley electrometer. The observed current represented the actual current times the gain achieved by the Spiraltron, i.e., $I_{measured} = CI_{actual}$, where C is the gain. Electro-Optics Division of Bendix(56) reported a gain of 10^8 was obtained during normal operation and this value was assumed for the actual current calculations. The resulting data are plotted in Figure 19. Note the linear increase in neon current as the applied potential increases from 500 to 2,750 volts. Above 2,800 volts, the current fluctuations were so extreme that it was impossible to obtain a steady state value. The range of the actual current extended from 10^{-17} to 10^{-14} amps. These current values were comparable with reported

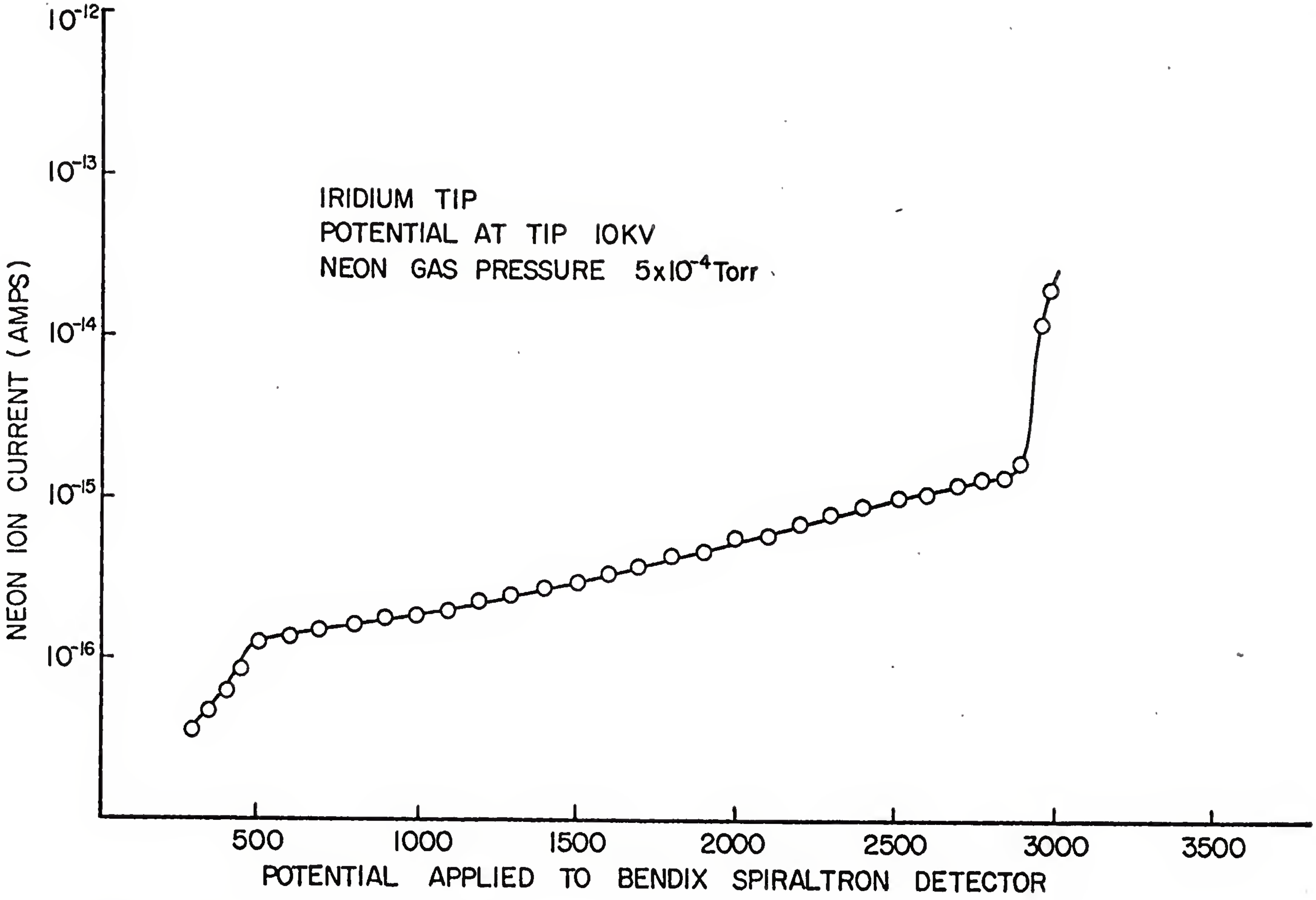

Figure 19. Neon ion current vs. applied potential to Spiraltron detector in analog mode.

data by Brenner and McKinney(52) for helium currents obtained with a similar Spiraltron detector.

The neon imaging gas pressure was reduced from $5\text{x}10^{-4}$ to $1.4\text{x}10^{-4}$ Torr and the resulting ion current indicated that the linear portion of Figure 19 was extended to 3 kV. Also, the tip potential was decreased from 10 to 9 kV and the image gas pressure remained constant at $5\text{x}10^{-4}$ Torr. These changes indicated no alteration in the actual current plot of Figure 19. Apparently, the 1 kV tip potential drop did not affect noticeably the ionization efficiency.

From these ion current measurements, it was established that the initial optical alignment between the tip and detector was sufficient to allow the emitted ion current to be detected by the Spiraltron. Next, the phosphor-coated screen was removed and the microchannel-plate image intensifier was assembled and aligned optically with respect to the drift tube orifice, as described in the previous chapter. The final alignment of the Spiraltron detector with the specimen tip and probe holes in the microchannel-plate, phosphor-coated screen, reflecting mirror and drift tube orifice was accomplished by two means. The first method (refer to Figures 9 and 16 in previous chapter) involved the following steps: remove the Spiraltron detector and end blank flange from the drift tube, locate a translucent grid on the specimen holder and carefully aim a He-Ne laser from the open end of the drift tube through the drift tube orifice and the probe holes of the reflecting mirror and microchannel-plate image intensifier. By viewing the grid on the specimen holder, the specimen holder could be adjusted until the laser beam coincided with the center of rotational axis of the specimen holder. Following this alignment, another translucent grid was superimposed over the open end of the drift tube and the drift tube was maneuvered until the laser beam was centered on the grid. The aligned drift tube was rigidly fixed with the two support tripods and the Spiraltron was repositioned and fixed when its incident aperture was centered on the laser beam.

The second means to assure optimum alignment of the tip and detector was accomplished electronically by measuring both the ion and electron currents. The ion current was measured with an iridium tip at 10 kV in a $5x10^{-4}$ Torr atmosphere of neon. Prior to the measurement, the applied potentials to the microchannel-plate image intensifier were removed. Again, the drift tube section was differentially pumped to less than $2x10^{-6}$ Torr. With the flexible bellows connecting the drift tube and atom probe it was possible to adjust the Spiraltron position in two directions. Initially, the detector was moved laterally with the adjustment screws on the support tripods from the previously fixed position determined by the laser beam alignment. The actual current observed in the initial position decreased in both the lateral directions and the two height adjustment directions.

Consequently, the Spiraltron detector was locked rigidly into the optimum position established by the laser beam method.

The iridium tip was replaced with a tungsten tip and the atom probe was altered to the field emission mode. The Spiraltron was coupled to a Monsanto Counter-Timer Model 101B to determine accurately the detected electron current as a function of the field emission potential. Initial measurement of the electron current, however, was not possible unless the potential was removed from microchannel-plate and ground screen for at least three minutes. The resulting data indicated that the electron current increased from an average 4.4 to 2,009 counts per sec (cps) as the tip potential was increased from 2 to 2.7 kV. When the tip potential was decreased the previous values were reproducible. Besides further confirmation of the tip and detector alignment, these data suggest the feasibility of utilizing the atom probe to obtain work function values from previously field ionized "clean" metal surfaces. Since the sensitive area of the tip ranges from 30 to 50 Å^2, emission measurements can be made on selected regions of the tip surface. For instance, comparative work function differences can be measured in relation to crystallographic orientation, atomic location in a particular plane, region in vicinity of lattice defect emerging at tip surface, degree of surface coverage by gaseous absorbants, and effect of solute concentration.

Operational Performance and Calibration

Defocusing of Ionic Species

After the ion and electron current measurements confirmed the alignment of the tip and the Spiraltron detector, the next operation to evaluate was the application of a 2 or 20 nanosecond high voltage pulse to the specimen tip and detect the field evaporated ionic species. Prior to the pulsed field evaporation it was necessary to increase the dc potential above the BIV (best image voltage) until the surface dynamically field evaporated at a reasonably constant rate. After establishing this field evaporation strength, the dc potential was decreased approximately 500 volts and the Microwave Nanosecond Pulser was activated. The amplitude of the 20 nanosecond pulses was increased by 50 to 100 volt increments until visual observation confirmed evaporation of the selected plane. In order to maintain a constant field evaporation rate for the selected plane, the amplitude of the pulse was adjusted until an atomic layer could be removed repeatedly by a certain number of pulses. After the parameters were established, the positive potential applied to the microchannel-plate and phosphor-coated screen were turned off. Müller(7) and Brenner and McKinney(52) report that these high potentials must be switched off prior to pulsing the tip or they will divert the trajectory of the field evaporated species and reduce the detector efficiency and mass resolution.

It was puzzling to observe that the magnitude of the emitted ion current from the tip to the Spiraltron detector was reduced significantly after the ground screen was replaced by the microchannel-plate image intensifier. For instance, the measured ion currents were an order of magnitude less than the expected value of 10^3 ions/sec at the imaging gas pressure of 1×10^{-5} Torr. However, the current was adequate from the previously described alignment to produce a sufficient amount of random single particle events on the triggered 100 μsec/cm sweeps of the Tektronix 549 Storage Oscilloscope. The expected time-of-flights for the evaporated species ranged between 1 to 20 μsec, providing the sweep of the Tektronix 549 Storage Oscilloscope was triggered simultaneously with the applied high voltage pulse. Continued application of the pulses failed to produce any signals in the expected time-of-flight interval, so the pulse amplitude was increased to produce a faster field evaporation rate, i.e., a smaller number of pulses to remove an atomic layer. Again, no signals were detected other than the random signals detected from the emitted helium ion current. Further adjustments in the applied dc and pulse potentials, imaging gas pressure, tip temperature, type of imaging gases, etc., still did not provide the expected time-of-flight signal detection following the pulsed field evaporation of the tip.

Since the image formation adjustments did not increase the low steady helium ion current or allow detection of the pulsed ionic species, other measures were taken subsequently to determine the cause of these experimental observations. While repeating and confirming the previous alignment results for the electron current measurements, it was again observed that a minimum of three minutes was required after switching off the microchannel-plate and ground screen before a reasonable electron current was detected. This extended time period suggested a possible charging effect on these glass components and a Keithley electrometer was connected to the phosphor-coated screen. After immediately switching off the applied potential to the screen, a few hundred volts were measured on the screen and even after ten minutes or longer, a considerable fraction of the initial potential remained on the screen (some tens of volts).

To further study this effect, the potential was returned to the screen for a short time while the tip potential was varied. The potential was then shut off and the high voltage lead was quickly connected to the 1,000M ohm Keithley electrometer. Again, the measured charge stored on the screen was several hundred volts and slowly decayed to a lower but still significant value with time. This dissipation time was reduced by immediately grounding the screen after removing the potential; however, a measurable fraction of the initial charge still remained. The next test involved turning on only the microchannel-plate potential during the field emission and connecting the Keithley electrometer to the screen. A negative potential buildup was observed on the screen. When the field emission and microchannel-plate potentials were removed, the observed dissipation time was similar to the previous results. These tests established that a definite charge buildup and long time constant were observed for the screen for both the ion and electron currents. Similar tests were conducted with the microchannel-plate and the same behavior was observed, except that the observed time constant was significantly higher.

Since it was determined that both the microchannel-plate and phosphor-coated screen exhibited a significant charge buildup, it is believed that this charge is concentrated at the perimeter of the central probe hole. Due to the uneven-probe hole diameter, the resulting radial field is very uneven and decays slowly toward the central region of the probe hole. If this field should contribute just 1 eV of energy to the passing ions or electrons, calculations indicate that the lateral velocity component can be increased and cause either the ion or electron to miss the input aperture of the Spiraltron by 1 cm. At this point, it is interesting to point out that Müller(7) and Brenner and McKinney(52) report that the original probe hole diameter of their atom probes was enlarged to 3 mm to achieve better mass resolution and detector efficiency. It seems that the increased probe hole diameter was a fortuitous choice because it effectively increased the diameter of the field-free portion of the probe hole which, in turn, influenced the number and trajectory of ions passing through the probe holes.

Now that the problem was established, steps were taken to remedy the effect. The most successful technique involved applying a negative potential to decrease the charge dissipation time and utilize both the microchannel-plate and phosphor-coated screen as electrostatic einzel lenses. A solenoid driven high voltage switch was constructed, so that the applied positive potential at the microchannel-plate could be switched instantaneously to a negative potential. Manual adjustment in reversing the applied potential polarity for the screen was adequate. To achieve optimum focusing of the ion stream it was necessary to establish the values of the applied negative potentials for both of the glass components. A liquid nitrogen cooled tungsten tip was imaged at 7.5 kV in helium at 5.6×10^{-5} Torr (gauge pressure). After aligning a particular region of the tip with the probe hole, the screen potential was turned off and the microchannel-plate switched from +900 volts to various negative potentials. The resulting helium ion current vs applied negative potential data are shown in Figure 20. From the curve, the optimum focusing potential for the

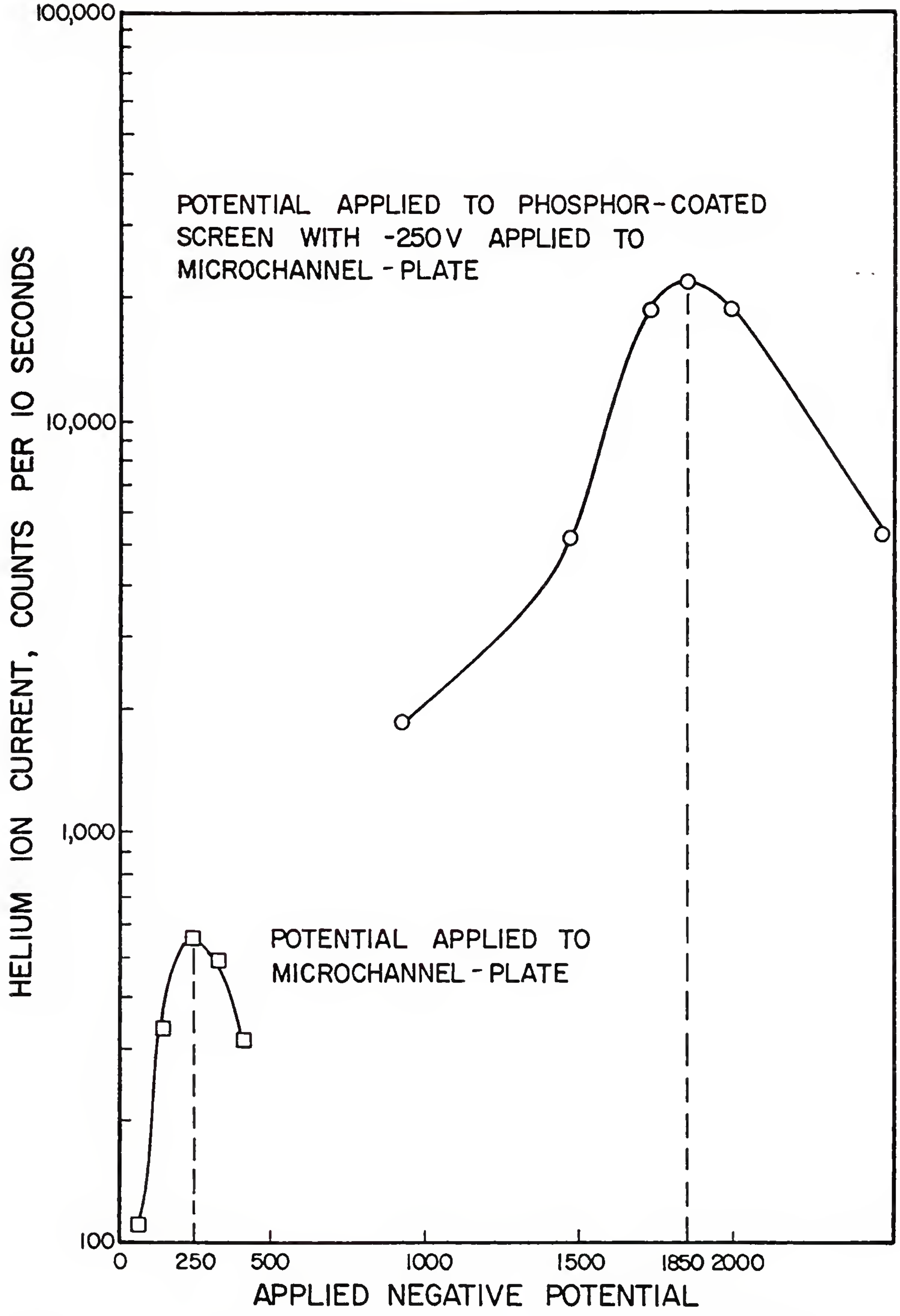

Figure 20. Optimum focusing potentials for microchannel-plate and phosphor-coated screen.

microchannel-plate was -250 volts. With this potential maintained on the microchannel-plate, the negative potential for the screen was varied. Resulting data are shown also in Figure 20. The maximum helium ion current was measured when the screen potential was -1.85 kV. This potential is approximately 25 percent of the applied potential to the tip and agrees with the reported value needed to focus the ions within a spot of 10 mm diameter at the detector.(7) Müller stated that perfect focusing was accomplished when the potential of the einzel lens was equivalent to 60 percent of the evaporation potential. As evident from the curves in Figure 20, the focusing potentials are very sharp. It is believed that the focusing potentials will need to be adjusted slightly for different imaging parameters, such as tip potential, imaging gas pressure, etc. However, this can be quickly done by monitoring the ion current with the analog mode of the Spiraltron. At this time, the electron current cannot be focused as effectively as determined for the ion current.

After correcting the defocusing effect, the maximum helium ion current exceeded 2,000 cps or $3.2x10^{-15}$ amps and was comparable to previously measured results. Although the observed defocusing effect was alleviated as described, it seems that the effect may be completely eliminated if the probe hole was enlarged from 1.5 to 3.0 mm or a quartz tube with a platinum- or silver-lined 3 mm inside diameter is inserted into 4 mm diameter probe holes of the microchannel-plate and phosphor-coated screen. To assure the interior of the metallic lined quartz tube remained field free, a small wire should be connected from this surface to the chassis ground. Both of these refinements are primarily concerned in limiting the lateral field components, as suggested by Müller et al.,$^{(48)}$ at the probe hole during the pulsing so as to obtain a well-defined ion trajectory. Other advantages inherent with the larger probe hole include the relaxation of the precision limits required in locating the tip at the optical axis, easier alignment of the tip and detector, and an increased sensitive area of the tip to be analyzed. An obvious disadvantage is the slightly decreased spatial resolution.

Detector Efficiency

Two general types of analysis are possible with the atom probe. One method involves fixing the tip's crystallographic location to be analyzed in relation to the probe hole and determining the ionic species field evaporated from this region. The second technique involves analyzing a specific image spot for the available crystallographic orientations. This means that the individual image spots are aligned with the probe hole and pulsed to identify their respective m/n ratios. The first method was utilized in the alignment of the ion detector with the tips. After correcting the observed defocusing effect, the amount of current was sufficient to monitor the field evaporation rate by this technique. This was accomplished by locating the edge of a particular plane near the probe hole and measuring the helium ion current. As the outer rings of the evaporating planes dynamically collapse past the probe hole the ion current increased to a maximum above the background current as each ring coincided with the probe hole. Providing the crystallographic lattice spacing is large enough to allow the probe hole to be positioned between two outer rings, an accurate evaporation rate can be obtained for different planes.

Single image spot sensitivity was determined from the following experimental results. A tungsten tip cooled to 78°K was imaged in a helium atmosphere ($6\text{x}10^{-5}$ Torr) at a potential of 7.5 kV. Since this potential was less than the best image voltage (BIV), large, bright image spots corresponding to the gaseous contaminates appeared stable on the tungsten surface as shown in Figure 21, where the white arrow indicates the probe hole position. The tip was carefully maneuvered until one of these large spots was visually aligned with the probe hole. The ion current for this spot was measured by the analog mode of the Spiraltron. By monitoring the current, the tip position was finely adjusted with the micrometer stage of the manipulator rod until a maximum was obtained. Next, the detector circuitry of the atom probe (refer to Figure 16 in previous chapter) was activated

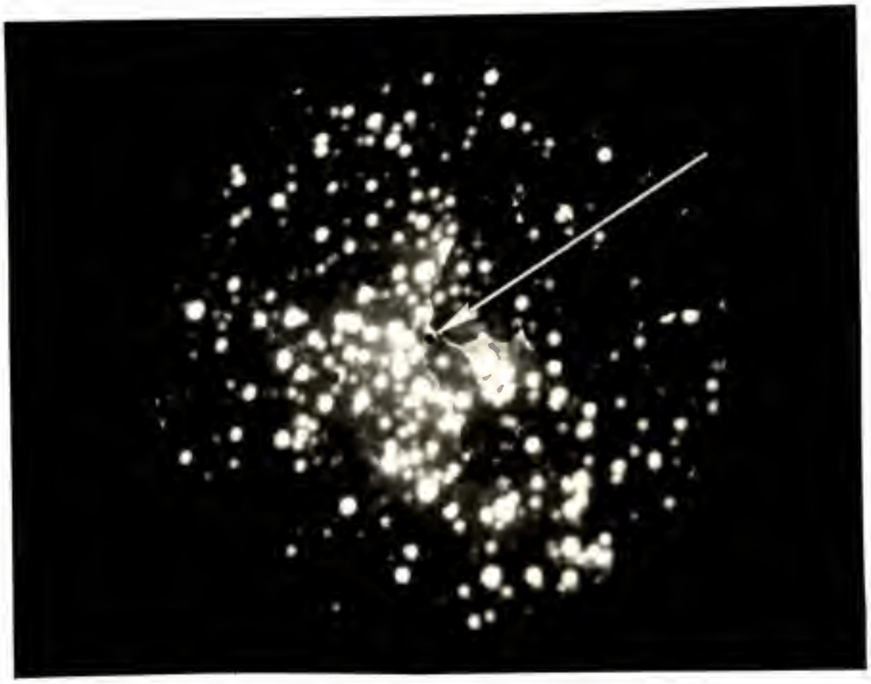

Figure 21. Micrograph of tungsten covered with gaseous contaminants at 78° K. Image potential 7.5 kV, helium $6x10^{-5}$ Torr).

to detect the random signals resulting from the helium ion current. Figures 22(a) and (b) represent the random signals observed with 500 μsec sweeps which were initiated by a trigger pulse from the high voltage pulser. From the ion current measurements and these random pulse traces, the alignment of the image spot and the probe-hole was sufficient to initiate desorption by pulsing of the tungsten tip. Prior to desorbing, the Spiraltron detector was switched to the pulse counting mode and the Microwave Nanosecond Pulser was activated. Maintaining the 7.5 kV dc potential constant, the amplitude of the 20 nanosecond pulse was adjusted until the gaseous contaminates were desorbed with a 900 volt pulse. The single spot alignment was repeated and the negative 250 and 1,850 volts were applied to the microchannel-plate and phosphor-coated screen, respectively. Now, the instrument was ready to detect the desorbed species. The 900 volt pulse to the tip and the trigger signal to the Tektronix 549 Storage Oscilloscope were initiated manually. Representative traces of the 20 μsec sweeps are shown in Figures 23(a) and (b). These particular traces were photographed with 3,000 speed Polaroid film. Notice how several of the signals obtained from the individual traces are aligned at a particular time or m/n ratio. These signals correspond to specific ionic species desorbed from the tungsten surface. It should be explained that there are approximately 10^5 ions per second associated with each image

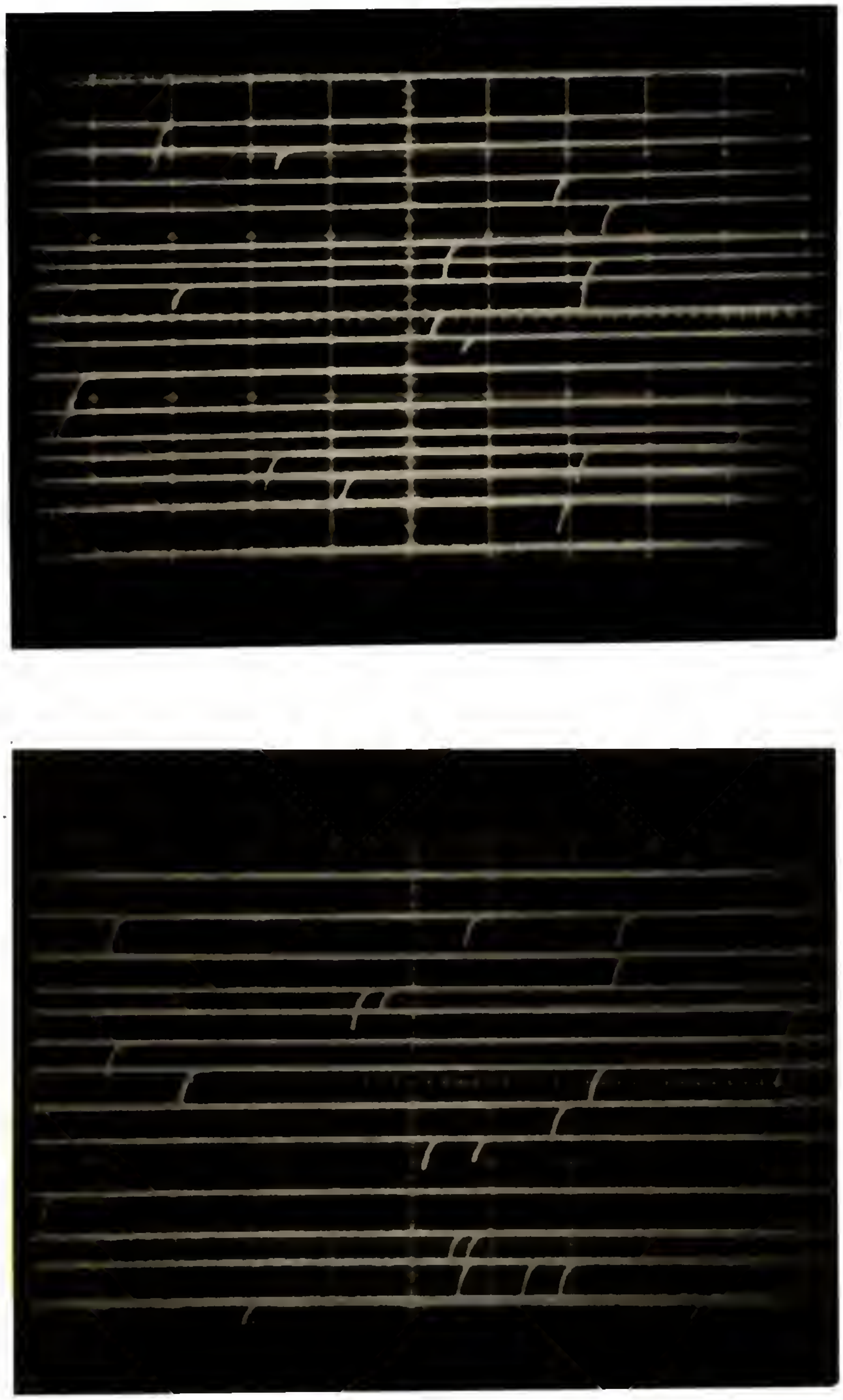

(a)

(b)

Figure 22. Random signals detected from triggered Tektronix 549 Storage Oscilloscope on 500 μsec traces.

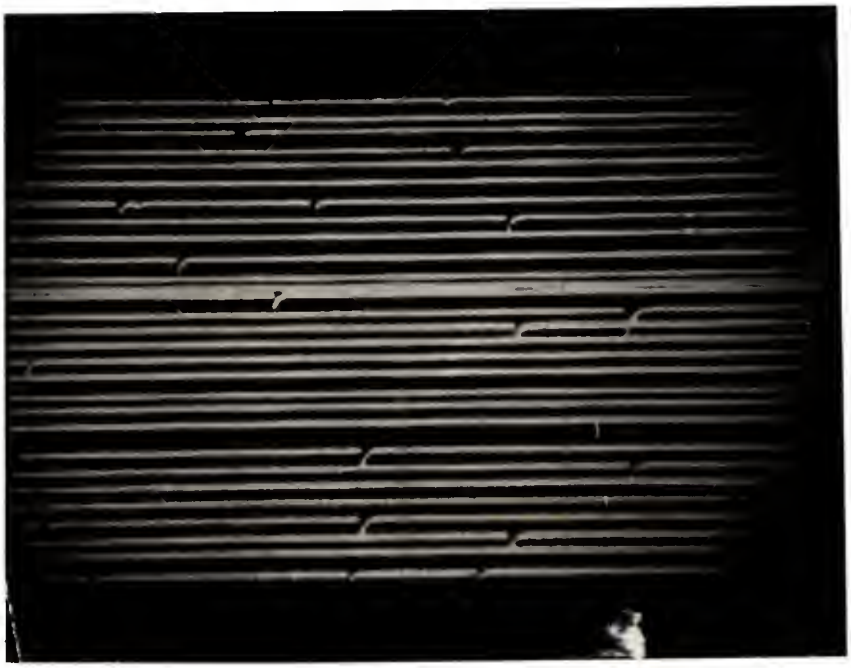

(a) Polaroid film, 3000 speed.

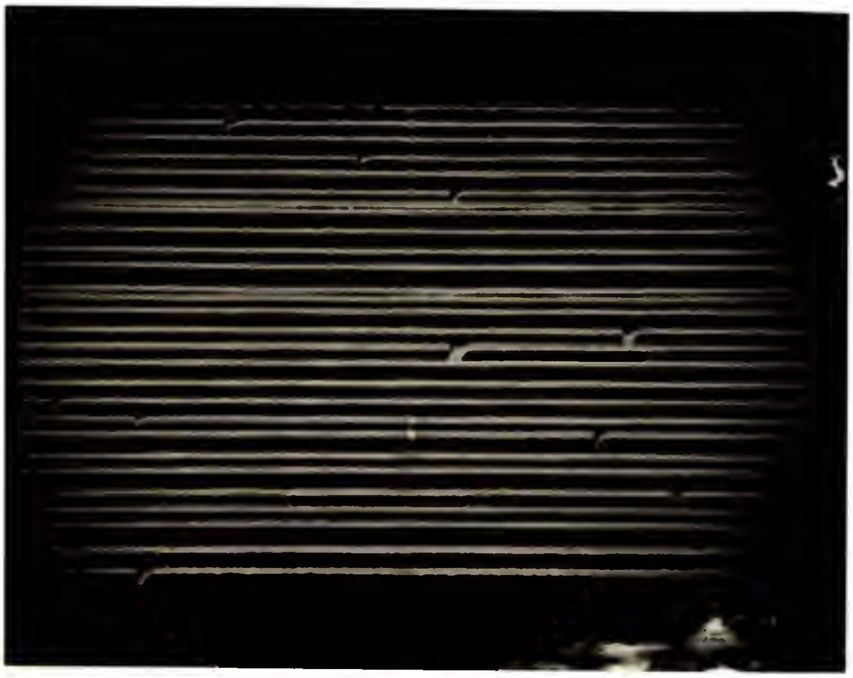

(b) Polaroid film, 3000 speed

Figure 23. Tektronix 549 Storage Oscilloscope 20 μsec traces of field desorbed species from tungsten surface, where V_{dc} = 7.5 kV and V_p = .9 kV.

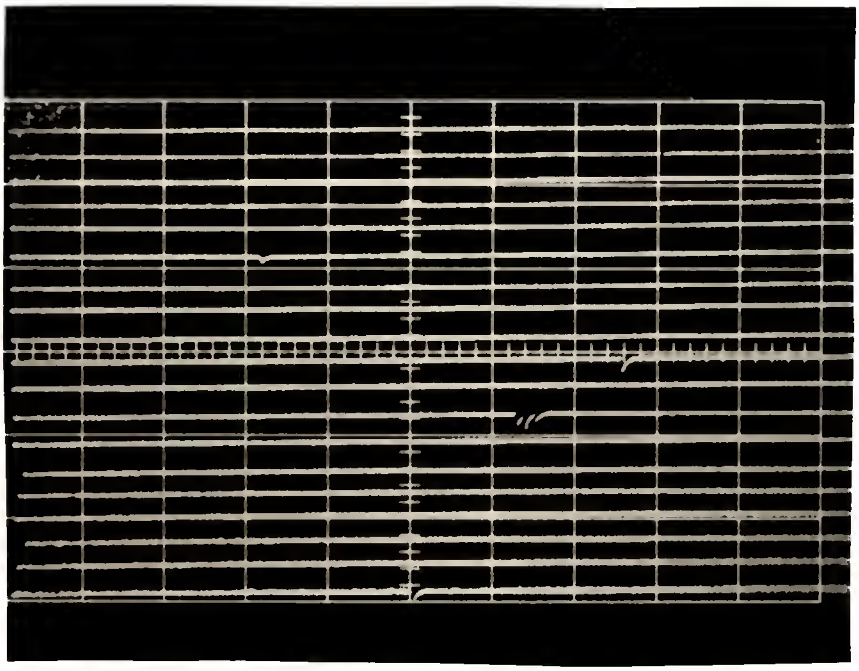

(c) Tri-X 35 mm film.

Figure 23. (cont.)

point at this particular imaging gas pressure. Consequently, there are about 10^5 random detector output pulses per second or 1 pulse every 10 microseconds. Since the travel times of the field desorbed species are usually less than 10 μsec, no more than 1 random signal should appear in the 10 μsec period. In addition, for a series of pulsings, Müller(7) pointed out that a vanishing probability exists for two random signals to arrive at the same place on the time (or mass) scale. In addition, if the amount of random signals become too high and affect the identification of the field evaporated ionic species, then the imaging gas pressure can be reduced, thereby directly decreasing the number of random signals.

From Figure 23(a), (b) and (c), the following ionic species were identified: H^+, N^{++}, N^+, O^+, O_2^+, CO_2^+, WN_2^{+++}, WN_2^{++}, WN_2^+, and possibly $W_2O_5^+$. Notice the improved resolution of the traces in Figure 23(c). Figure 23(c) was photographed with Tri-X 35 mm film, whereas Figures 23(a) and (b) were taken with 3,000 speed Polaroid film. The presence of these ions can be explained reasonably. For example, the hydrogen ion can be expected from two sources, either as an impurity in the tungsten or as a residual gaseous element contained in the all-metal atom probe body. A slight amount of CO_2 is also common in baked vacuum systems, whereas the oxygen and nitrogen indicate a leak. Coincidentally, as the data were obtained, a small leak developed in the cryogenic cold finger and a slight rise in the system pressure was observed. The two tungsten nitride species and possible oxide species indicate that even at 78°K the nitrogen and oxygen were field etching the tungsten.(11) When the pulse was applied to the tip, the field strength was sufficient to field evaporate the nitride and oxide species. Contrasting Müller's observation of helium absorption at the tungsten tip at 78°K,(14) no evidence of helium species was observed during this analysis. This indicates that at the 78°K tip temperature only a slight amount of helium was absorbed at the surface as compared to other gaseous impurities. The excessive amount of nitrogen and oxygen present, plus the field etching of the tungsten, all contributed to the absence of helium. In addition, it is believed that some of the observed spurious signals are helium or some other gaseous species that were ionized a finite distance away from the tungsten surface and consequently do not have the full kinetic energy needed to arrive at the Spiraltron detector at their expected time of flight. From these traces it was observed that the aligned single spot was detected approximately 50 percent of the time after pulsing. However, if the probe hole was fixed on a particular crystallographic plane and field desorbed, the detection efficiency was considerably less and depended upon the selected crystallographic plane. Besides identifying the individually desorbed species, these traces also proved that the crucial alignment of the single imaging spot with the probe hole can be achieved successfully 50 percent of the time.

To provide further proof of the detector's efficiency, a tungsten tip was imaged in a helium-10 percent neon gas mixture ($2x10^{-5}$ Torr) and cooled to 78°K. The resulting image is shown in Figure 24. Note that the image is significantly brighter than the helium image, as shown in Figure 17, which was photographed at the identical exposure. The probe hole is indicated with a white arrow and is positioned on the center (110) plane. The dark, irregular shaped regions are believed to be due to either a burnt phosphor screen coating or nonuniform conductive coating on the microchannel-plate. After the BIV was established, individual image spots were first visually aligned with the probe hole and finally positioned with the micrometer at a maximum current. The high voltage 20 nanosecond pulse amplitude was adjusted to achieve a constant evaporation rate that required 10 pulses to remove one (110) plane, i.e., $K_e(110) = 5x10^6$ planes/second. As previously described, the negative potentials were applied to the microchannel-plate and phosphor-coated screen prior to field evaporating the tungsten tip with the high voltage pulses.

The resulting traces were photographed with Tri-X 35 mm film at one second exposures. Two of the typical 20 μsec traces are shown in Figure 25(a) and (b). These particular traces indicate that the ionic species CO_2^+, WO_2^{+4}, WO_2^{+3},

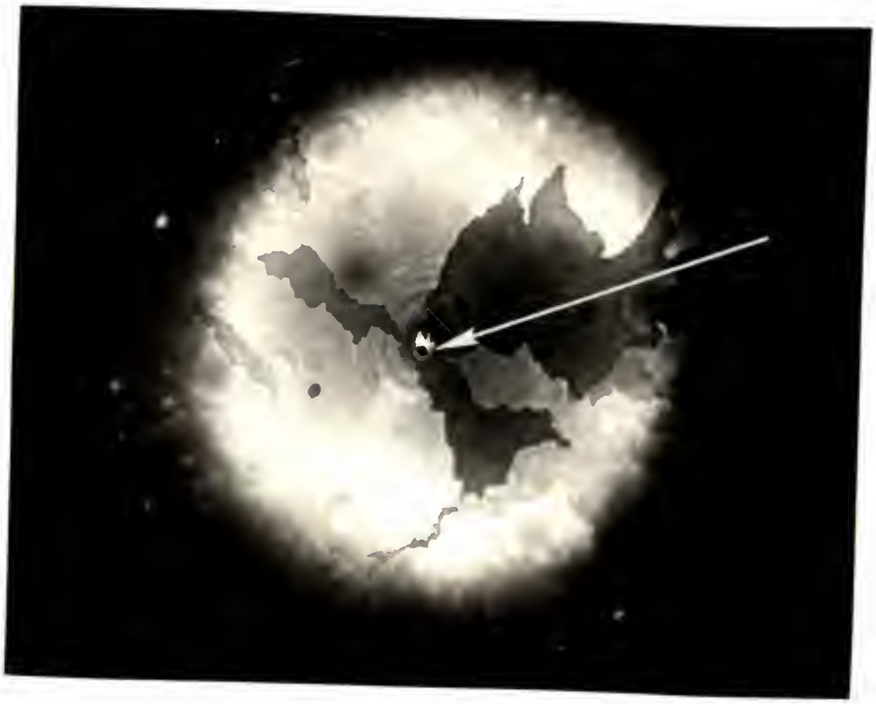

Figure 24. Micrograph of tungsten at 78°K imaged in helium-10 percent neon (2×10^{-5} Torr).

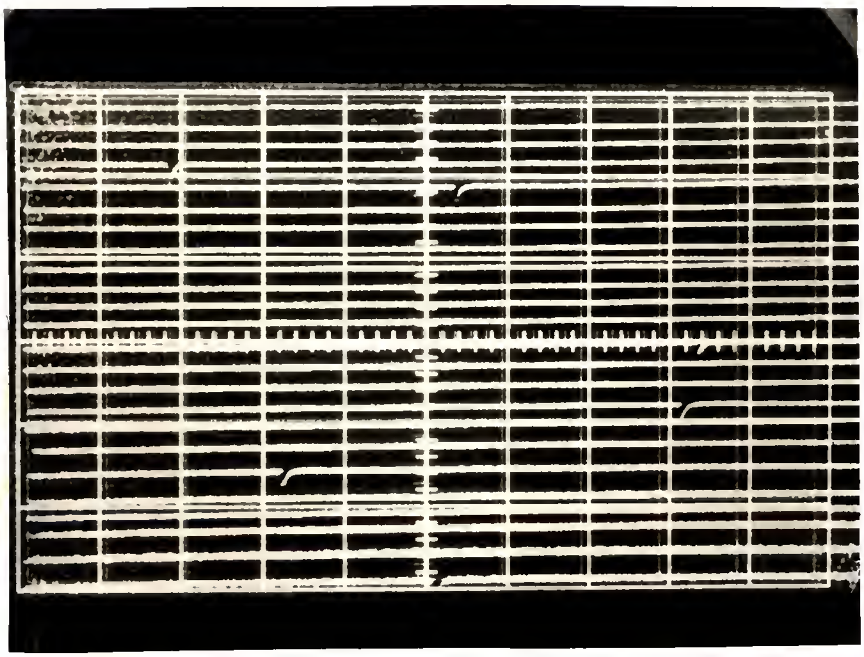

(a) 20 µsec trace.

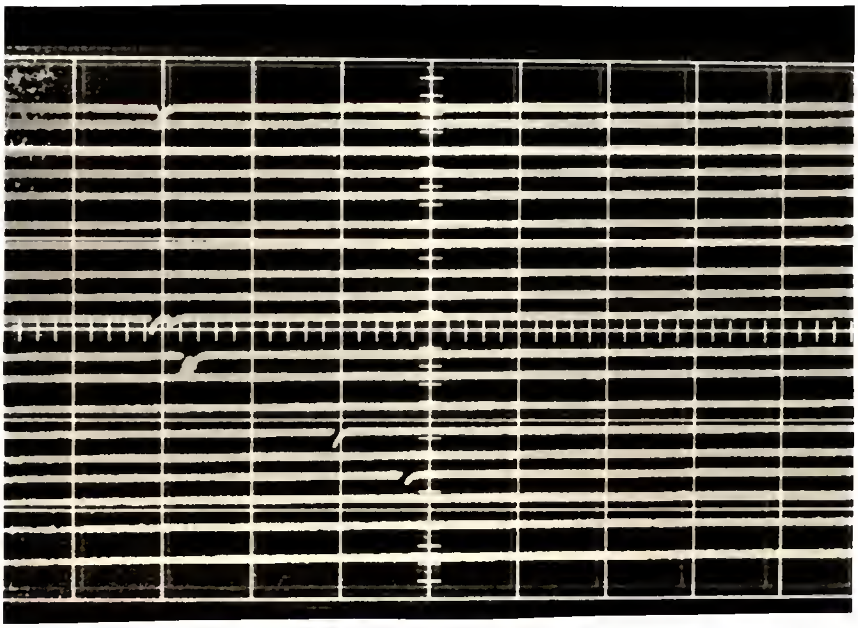

(b) 20 µsec trace.

Figure 25. Tektronix 549 Storage Oscilloscope, 20 and 10 µsec traces for field-evaporated tungsten at 78°K in helium-10 percent neon (2×10^{-5} Torr).

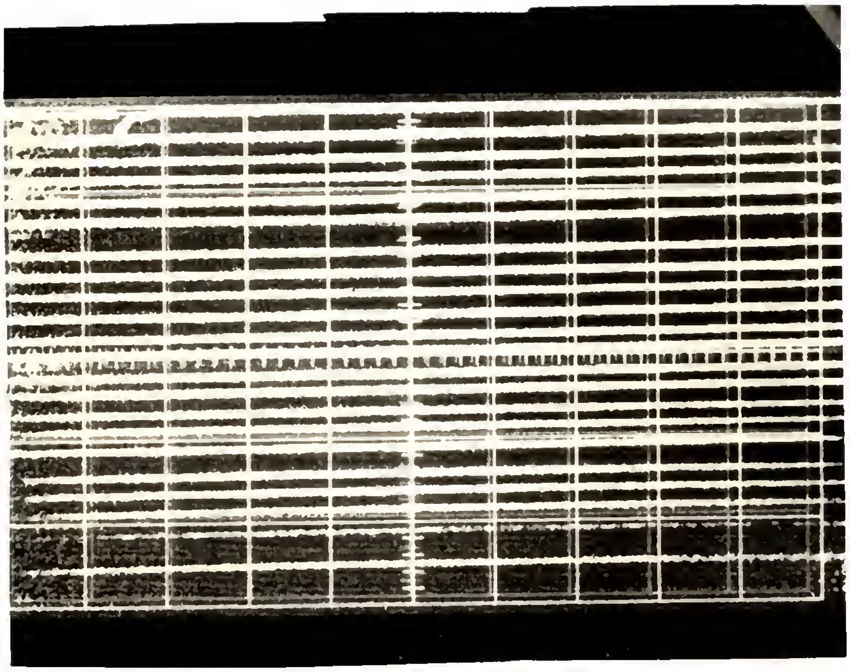

(c) 10 μsec trace.

Figure 25. (cont.)

WH_2^+, $WO_2 \cdot H_2O^+$ and possibly $W_2O_5^{+3}$ were field evaporated from the tungsten tip, while other 20 μsec traces taken at different V_e values indicated the additional species, H^+, N_e^{++}, O^+ and possibly WH_2^{+4}. Figure 25(c) represents a 10 μsec sweep and identifies a N^{++} species. Again, these tungsten-hydride species appear reasonable, since the tungsten's reaction with the residual hydrogen is expected. The neon ionic speciesis possible since it is present in the imaging gas, while the oxygen and nitrogen could result from their surface migration down the shank of the tungsten tip. Also, they could indicate that the small vacuum lead in the cold finger wasn't completely sealed. Again, the CO_2^+ could be a residual gas contaminate in the vacuum system.

At this time it appears the limited number of evaporated species prevents a proper statistical representation of the various ionic species field evaporated from the tungsten under the described imaging parameters. In addition, it seems imperative to further enhance the resolution of the detected signals by using either 500 or 200 nsec sweeps. These sweep values will allow a more accurate time or mass distinction between the evaporated ionic species. To identify the described experimental results the most abundant tungsten isotope, W^{184} (30.64 percent), was assumed to be the dominating species. Consequently, the 20 and 10 μsec traces indicated only the field-evaporated tungsten-hydride, -nitride, and -oxide ionic species, whereas the tungsten-helium and -neon molecular compounds previously reported by Müller(14) were not detected. If the other tungsten isotopes, W^{182}, W^{183} and W^{186} with respective natural abundances of 26.41, 14.4 and 28.41 percent were possibly obtained, then the distinction between the different ionic species would be very difficult because they have identical AMU values,(45) for instance, $W^{184}H_2^+$ and $W^{182}He^+$ have an identical AMU value of 186. However, if the field effect is ignored, and strict attention is centered on the available thermodynamic heats of formation for the tungsten hydrides, oxides and nitrides compounds, their formation is reasonably predicted in comparison to the tungsten-helium and -neon compounds.

The results with the tungsten field evaporation study indicate further efforts need to be made at 21°K to see if any tungsten-helium and -neon compounds exist. Also, it becomes evident that further detector efficiency tests need to be conducted with metals (and imaging and impurity gases) which have a high natural abundance of one isotope, such as Al^{27} (100 percent), V^{51} (99.76 percent), CO^{59} (100 percent), Nb^{93} (100 percent), Rh^{103} (100 percent), Ta^{181} (99.988 percent), Au^{187} (100 percent), He^4 (100 percent), Ar^{46} (99.6 percent), N^{14} (99.6 percent), O^{16} (99.76 percent), H^1 (99.985 percent) and $Ne^{20.2}$ (90.92 percent). This will allow the mass resolution to be more dependent upon the oscilloscope traces and control circuitry dead time, rather than the spread in AMU values for the various possible isotope compounds. For example, with the tungsten data, the WO_2^+ compound for the various isotopes have the following AMU values: $W^{184}O_2^+$ (216), $W^{186}O_2^+$ (218), $W^{182}O_2^+$ (214) and $W^{183}O_2^+$ (215). From the obtained traces, the mass resolution is ±.5 AMU so the distinction between $W^{182}O_2^+$ (214) and $W^{183}O_2^+$ (215) and $W^{184}O_2^+$ (216) is possible providing the correct pulse factor and electronic time were used. Further consideration of the natural abundance of the various isotopes enables a means to select particular alloy compositions for other studies involving the atom probe, such as ordering, solute atom distribution, etc. For instance, attempts should be made to select at least one of the alloying constituents to be a single isotope. This will greatly increase the detector efficiency and mass resolution of the field-evaporated species.

During the pulsed field evaporation of the tungsten in the helium-10 percent neon atmosphere at 78°K, the efficiency in detecting the evaporated species from an aligned image spot was below 50 percent. This reduction was partially due to the observed parallax between the position of the tungsten surface atom and its ionization zone.(11,52) The efficiency was considerably improved when the probe hole was positioned at the inside portion of the evaporating ring. This probe hole location agreed with that reported by Brenner and McKinney.(52) The fixed probe hole method was also evaluated and its detection efficiency was less than 30 percent.

It is believed, however, that this value can be improved if the applied dc potential is increased, and the pulse potential minimized.

Calibration and Mass Resolution

As discussed previously in the electronic circuitry section of the previous chapter, the specimen tip in the atom probe represents an unterminated end of a transmission line which is characterized by voltage reflections. Unfortunately, this line cannot be terminated because of the high dc potential. Consequently, if the amplitude and duration of the initial pulse is sufficient, the resulting reflections will reinforce themselves and produce an effective pulse at the tip which is greater than the initial pulse. This magnification factor of "pulse factor" α will range from unity to two and results in expression (27) being modified as shown:

$$\left(\frac{m}{n}\right)_o = \frac{1930}{d^2} (V_{dc} + \alpha V_p)\ t^2 , \tag{29}$$

where α is the pulse factor; also, the travel time of the field-evaporated species is not directly recorded on the Tektronix 549 Storage Oscilloscope because of the electronic delay times of the various components. Thus, the total electronic delay time, δ, can be included in the above relation as

$$\left(\frac{m}{n}\right)_o = \frac{1930}{d^2} (V_{dc} + \alpha V_p)(t \pm \delta)^2 , \tag{30}$$

where t is the observed oscilloscope time.

Since the V_{dc} and V_p were accurately measured, the previously described field desorption and evaporation traces for tungsten were analyzed by assuming different values for the pulse factor and the electronic dead time. Although insufficient statistical data were obtained to determine exact values, the calculations for the detected species indicated better than ±.5 AMU accuracy from the 20 μsec sweeps, when α and δ were assumed 2 and zero, respectively. By using the H^+ as one of the calibration ions, the time intervals between it and the other detected signals resulted in consistent AMU values within ±.5 AMU for the m/n ratio below 100 and ±.7 AMU for the m/n ratios above 100. It is believed that if the sweep time is expanded at the H^+ specie the practical resolution can be less than ±.5 AMU. Further efforts can be made with single isotope materials, such as Rh, Co and Au, and imaging gases H, He, Ne and Ar, to obtain an accurate pulse factor α as described by Müller _et al._(48) In addition, it is believed that the absolute pulse factor might be determined by calibrating the 20 nsec pulse amplitude with the measured potential at the tip. This would be difficult and would require a fast oscilloscope to detect this 20 nsec pulse, and a fast camera to record the pulse.

The accurate values of α and δ are primarily required to distinguish ionic species within 1 AMU and, at present, if the materials analyzed by the atom probe are not adjacent in the periodic table, no difficulty should exist in consistently achieving better than ±.5 AMU. Also, it appears that this value may be improved if the Tektronix 549 Storage Oscilloscope is expanded to a 200 nsec total sweep time at the location of a particular ionic specie.

CHAPTER V

FIELD EMISSION AND IONIZATION MICROSCOPE

Introduction

The field emission microscope was developed by Müller(59) in 1937. It consisted of a glass vacuum vessel in which a metallic specimen was mounted. The specimen was polished to a fine point and experienced a high electrical field of negative polarity. The magnitude of the field at the sharp tip was 0.3 to 0.5 V/Å, which was sufficient to emit electrons approximately normal from its hemispherical surface to a grounded fluorescent screen. The magnification of the resulting image was approximately a million diameters and was estimated by the ratio of the screen distance and tip radius. The reported resolution(59) limit was about 25 Å.

In 1951 Müller utilized essentially this same microscope to obtain a hydrogen ion image of the emitter surface. To accomplish this feat it was necessary to polish the metallic tip to a much smaller radius (less than 1,000 Å), apply a positive potential and fill the glass vacuum vessel with hydrogen at a partial pressure of 1×10^{-3} Torr. The sharper tip radius generated field strengths of 3 to 5 V/Å, which were sufficient to ionize the hydrogen gas. The positive hydrogen ions were repelled from the tip and radially projected from the tip to the ground phosphor screen. This image had greater magnification than the field emitted image, plus its resolution ranged from 2 to 3 Å to provide individual atomic observation.

Two basic features were needed for the field emission microscope to achieve this field ionization mode. They included the cryogenic cooling of the specimen tip and shield and the photographic recording of the weak image with a flat phosphor-coated screen. Consequently, the technical design requirements for a microscope that can be operated in both the field emission and field ionization modes are similar to those described in detail for the atom probe. The two primary exceptions required by the atom probe are the mechanical manipulation of the imaging specimen tip and the identification of the field evaporated ionic species by the time-of-flight mass spectrometer. Subsequently, only the important innovations and applications of this constructed instrument will be discussed.

Description of Microscope

The constructed microscope is shown in Figure 26. Since the various components of the microscope posed particular design, material selection and fabrication problems,

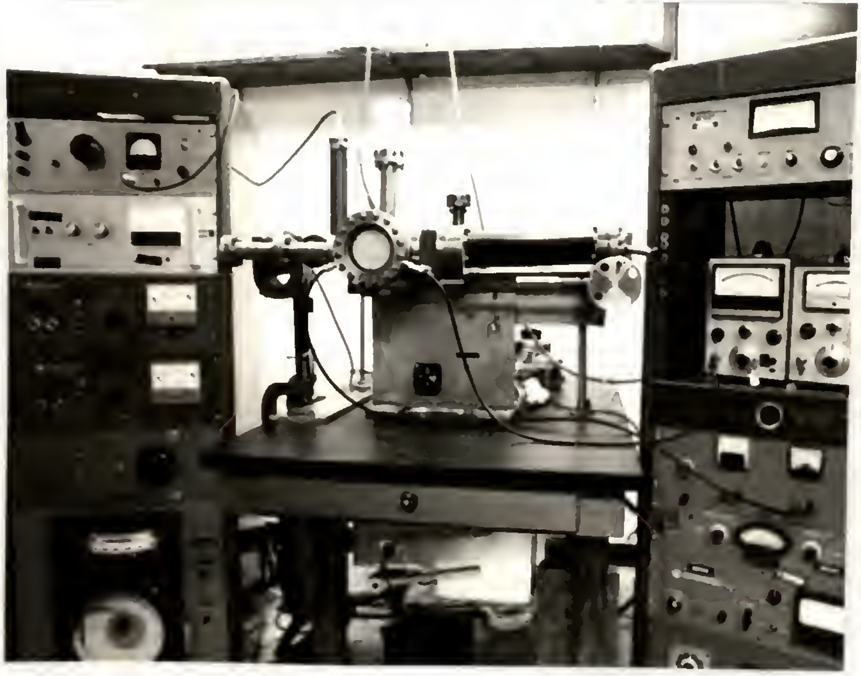

Figure 26. Constructed field emission and ion microscope.

they will be discussed individually as follows: 1) ultrahigh vacuum system, 2) specimen holder and exchange mechanism, 3) image formation, and 4) high voltage atmospheric feedthrough and power supplies. In addition, the electrical circuitry and instrumentation required to measure work function values with this microscope will.be presented separately.

Vacuum System

Type 304 and 316 stainless steel vacuum hardware, glass view ports and ceramic insulated high voltage feedthroughs were selected to construct a bakeable, rugged vacuum system. Figure 27 illustrates a schematic diagram of the completed unit. Roughing from atmospheric to less than 10 microns pressure was done with a Varian vacsorb pump. The entire system can be pumped with two 8 ℓ/sec Varian ion pumps and one 20-400 ℓ/sec Varian ion and titanium sublimation pump. However, during operation the microscope body is pumped by only one of the 8 ℓ/sec Varian ion pumps and the 20-400 ℓ/sec Varian ion and titanium sublimation pump. The remaining 8 ℓ/sec ion pump is used to evacuate the isolated specimen exchange section. The imaging gases are introduced through two Granville-Phillips leak valves so positioned that the imaging gases must pass over the freshly deposited titanium prior to entering the microscope body. This greatly diminished the amount of gaseous contaminates that reached

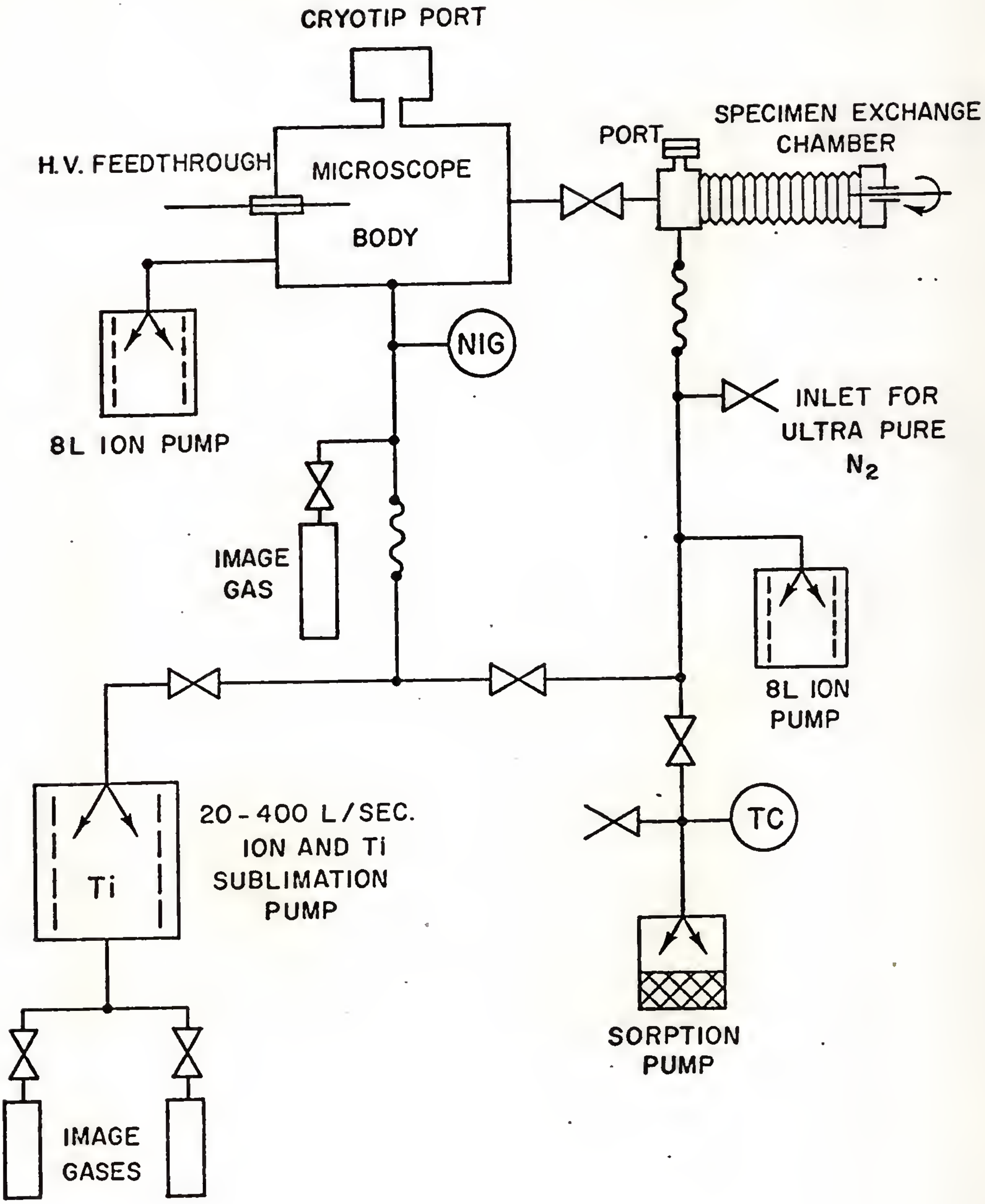

Figure 27. Ultra-high vacuum system for microscope.

the specimen tip. The pressure of the microscope body is monitored with a Varian dual nude ion gauge.

Efforts were concentrated on increasing the number of specimens observed in the normal field ionization mode for this microscope. Consequently, a bakeable $2\frac{1}{2}$-inch gate valve was procured to keep the microscope body at UHV, while the isolated specimen exchange chamber was opened to remove and insert new specimen tips. With this arrangement routine specimen exchanges were completed in less than one hour as compared to the half-day to one-day interval formerly needed.

After bakeouts at 250°C for 24 hours the microscope reached routine vacuums of $5\text{x}10^{-9}$ Torr. Subsequent periodic titanium sublimation pumping of the system for another day obtained adequate pressures for field emission measurements. Since an optical fiber viewing screen was mounted to the microscope, the heating and cooling rates of the bakeouts were controlled at one degree per minute with a cam-operated furnace. Also, the gate valve with its Viton O-ring and the microchannel-plate electron multiplier limited the bakeout temperature to 250°C. However, frequent bakeouts are avoided because the microscope body is maintained at UHV pressures and is exposed normally to pressures less than $5\text{x}10^{-7}$ Torr during the specimen exchanges.

Specimen Holder and Exchange Mechanism

To accomplish the desired quick specimen exchange, it was necessary to devise a means to mechanically maneuver the specimen holder between the microscope body and the exchange chamber. The selected method involved using a chamber made from a flexible stainless steel bellows which could be compressed and expanded linearly to insert and remove the specimen holder and allow closure of the isolating gate valve. Various features required for the final specimen exchange mechanism included the following: precise female dovetail joints for the two positions of the specimen support yoke that were carefully aligned so the male dovetail joint of the specimen holder could easily slide into each position, rigid support rods to guide the flexible stainless steel chamber, brass bearings and counterweight to assure smooth movement of this flexible chamber and a slotted push rod that was mounted to a rotary UHV manipulator to allow engaging and locking of the specimen holder during exchange.

A photographic sequence of steps involved in inserting the specimen holder into the microscope's body is illustrated in Figure 28. In Figure 28(a) the specimen holder is locked initially in the slotted push rod. Next, the specimen holder is aligned with the desired yoke position visually from the end view port. This position is shown in Figure 28(b), as photographed from the front view port.

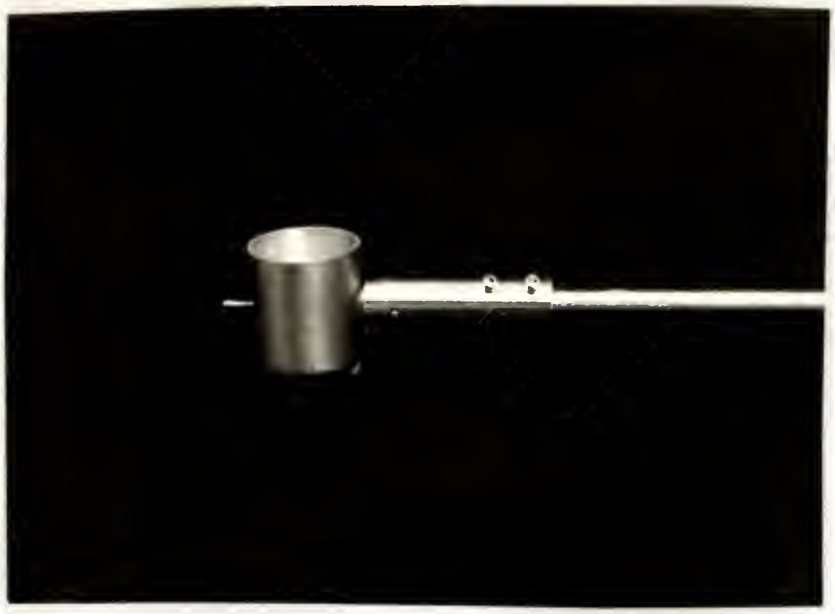

(a) Specimen holder locked in slotted push rod.

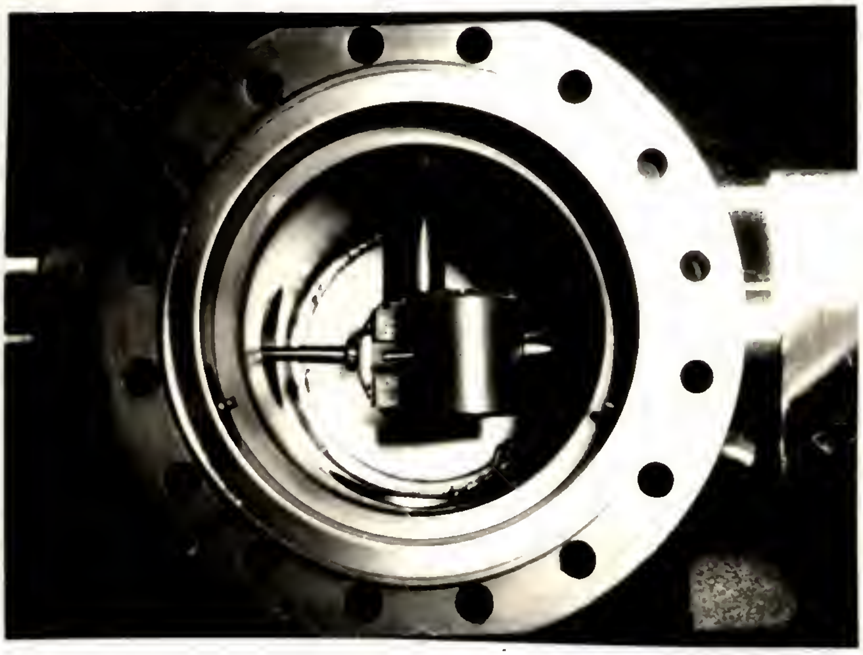

(b) Specimen holder aligned with yoke.

Figure 28. Sequence involved with specimen exchange mechanism.

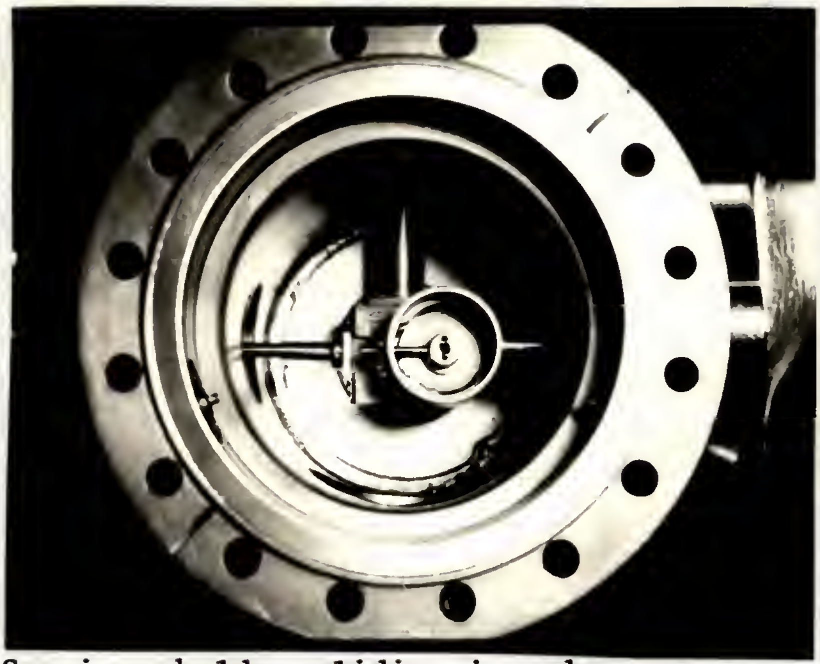

(c) Specimen holder sliding in yoke.

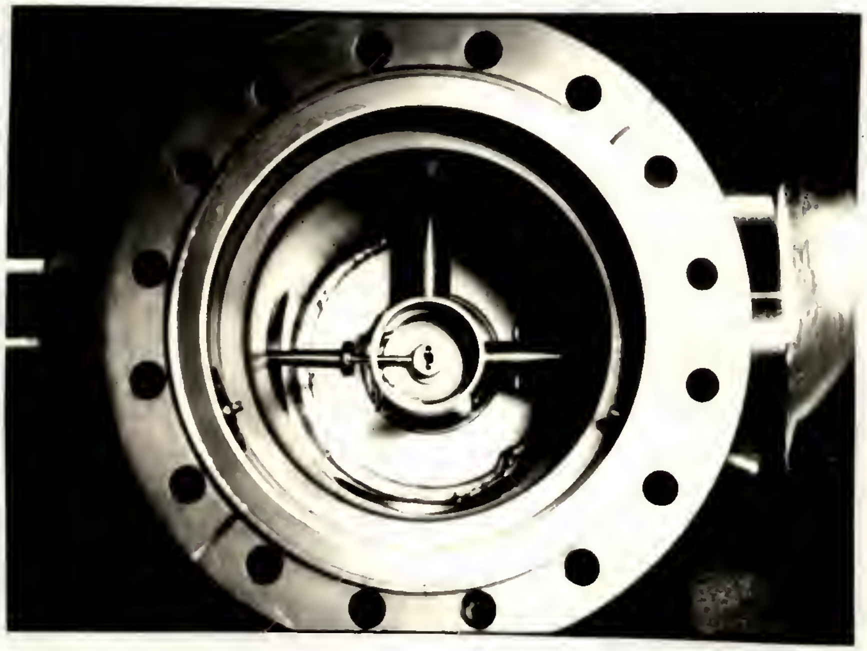

(d) Specimen holder in final position.

Figure 28. (cont.)

Figure 28(c) depicts the specimen holder sliding in the dovetail joint of the yoke toward the stainless steel spring-loaded high voltage lead. Figure 28(d) represents the final position of the specimen holder, after the slotted push rod was unlocked and retracted into the flexible chamber. Cryogenic cooling of the specimen was realized by filling the OFHC copper support yoke with liquid nitrogen or hydrogen that was developed with the Air Products Cryotip.(60) Besides the intimate dovetail joint between the yoke and specimen holder, two sapphire disks were securely tightened in the specimen holder to enhance thermal conductance from the tip. In addition, these sapphire disks insulated electrically the specimen holder from the applied high voltage at the tip.

Image Formation

The microscope body was designed to house a microchannel-plate image intensifier in the front view port. This electron multiplier device enabled easy observation and photography of the helium-, neon-, argon- and hydrogen-ion images. To obtain this intensified image, the specimen holder is inserted initially in the specimen yoke opposite this front view port. Once the specimen,imaged a high voltage pulser was utilized to determine the field evaporation potential. With the intensified image the stripping of the adsorbed species and protruding surface atoms could be easily detected. When the field evaporation process produces a "clean" atomically smooth tip, two options are available for further analysis. First, the tip can be removed from the microscope and installed in the atom probe. By obtaining the complete image characteristics of a tip and selecting a tip that exhibited the desired features, the efficiency of the atom probe analysis was markedly improved. In addition, the possibility of "flashing" the tip was diminished.

Due to the limited resolution of the image from the intensifier device, a phosphor-coated optical fiber screen was mounted to the bottom part of the microscope. Consequently, if it was desired to obtain a highly resolved image, as reported by Hren and Newman,(61) the specimen holder was manipulated to the second position of the support yoke that faced the bottom view port. In addition, the work function of the "clean" emitter surface could be measured with this optical fiber screen. This involved pumping the microscope body until adequate UHV conditions were obtained for field emission. Details of this analysis will be presented later.

High Voltage Atmospheric Feedthrough and Power Supplies

An atmospheric high voltage feedthrough similar to the one described for the atom probe was designed and constructed for the microscope. The circuit's components are arranged as shown schematically in Figure 29. Since the high voltage pulser used with this microscope was not a transmission line type, it was not necessary to match the characteristic impedance of its output line. Also, the high voltage pulser produced pulses with 50 microsecond to 1 millisecond durations and 100 to 2,000 volts amplitude. Consequently, the pulse section of the circuit contained R_1 and C_1, which were a 60 M ohm resistor and 40 kV, 1,000 pf capacitor respectively. The dc high voltage segment of the feedthrough circuit contained a 10 gegaohm resistor (R_2) to reduce possible "flashing" of the tip.

A Brandenburg high voltage power supply was selected for the 0 to 30 kV source. In order to accurately determine the tip potential, a calibration was made between the potential recorded by the instrument and the potential measured with an electrostatic voltmeter at the tip position. The results are shown in Figure 30 and indicate a slight difference between the two values. For example, a 10 kV potential was recorded at the tip position while the meter of the Brandenburg power supply read 9.5 kV.

Description of Field Emission Analysis

Field emission microscopes provide two primary types of data for studying the emitter's surface. These are the photographs of the emitted images which illustrate differences in the work function and/or local field over the

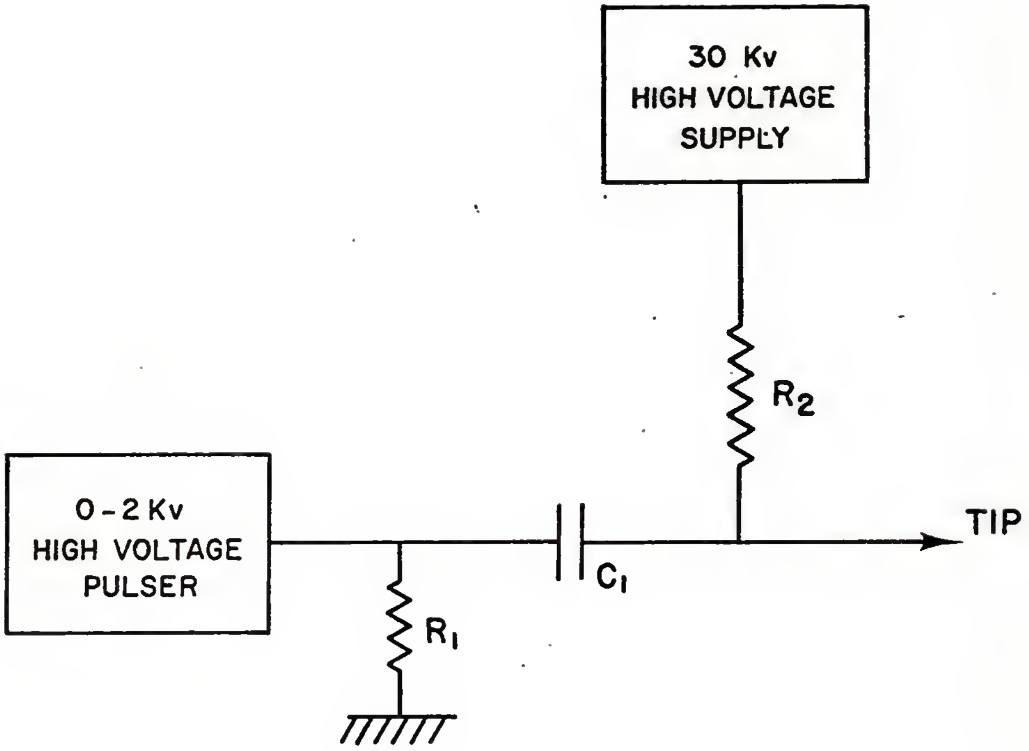

R_1 = 60 M OHMS

R_2 = 10 G OHMS

C = 1,000 pf, 40 Kv

Figure 29. Atmospheric high voltage feedthrough circuitry for microscope.

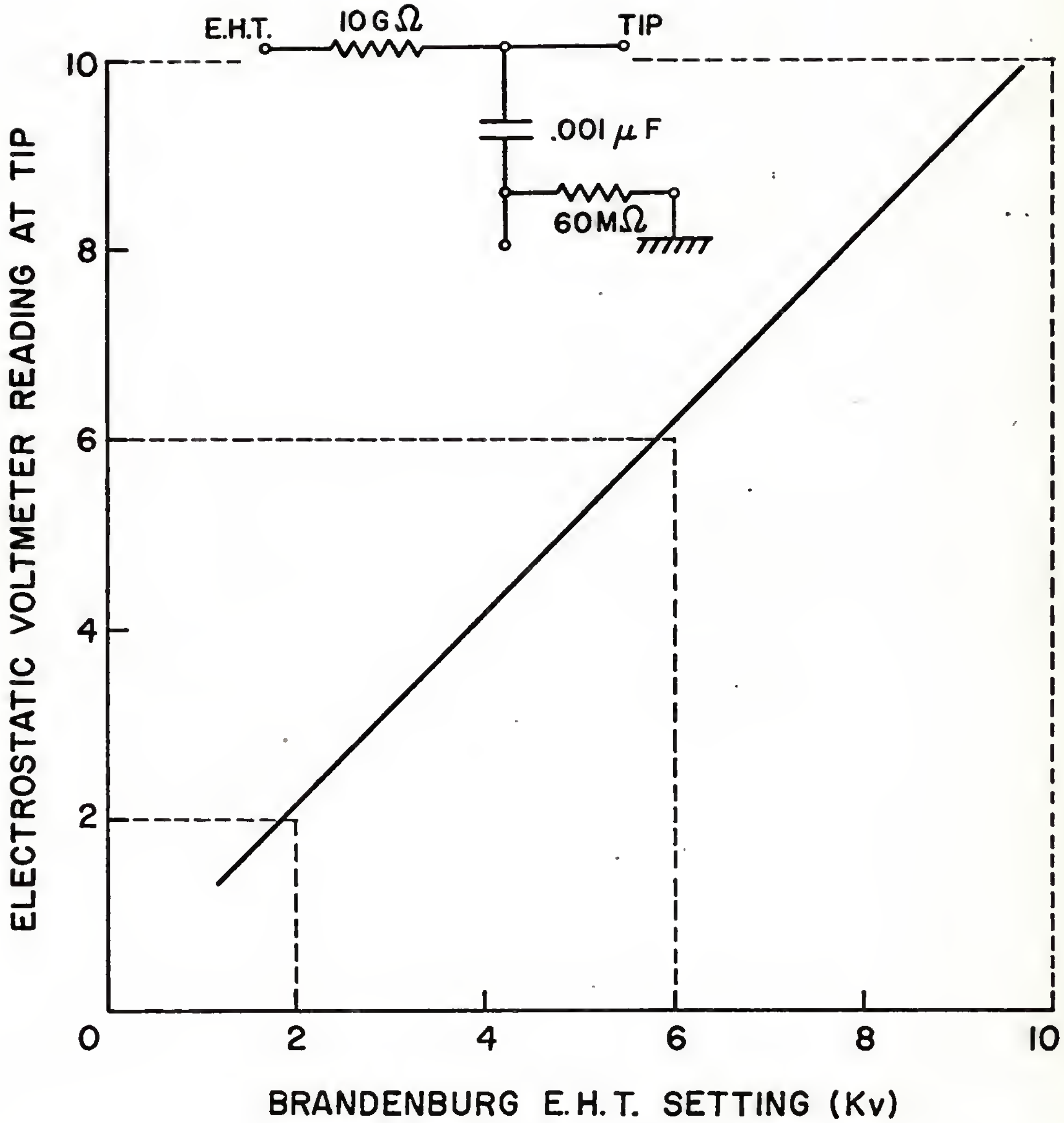

Figure 30. Calibration of Brandenburg high voltage supply.

emitter surface and current-voltage data that are plotted as ℓn I vs. 1/V in accordance with the Fowler-Nordheim relation.(22) Detailed emission patterns were obtained by photographing the emission image at the 6 micron diameter optical fiber screen. In addition, current-voltage data were obtained from the optical fiber view port by the circuitry shown in Figure 31.

Providing theoretical behavior is exhibited, the ℓn I vs. 1/V plot is linear with the slope proportional to $\phi^{3/2}$, the work function. Experimentally, the total emission current I was measured for the various crystallographic regions as a function of the inverse of the cathode potential. In Figure 31 the section of the circuit supplying the potential to the emitter was coupled to a Keithley 610B electrometer to monitor the total current emitted at the tip. As illustrated in Figure 31, the emitted electrons will diverge radially away from the tip and strike the flat optical fiber screen. Most anode viewing screens(22) in field emission microscopes are spherical to include all the emitted electron current from the tip. However, the resultant emission patterns taken from the flat screen appeared axially symmetric and compared favorably with reported emission patterns.(22)

The emission current striking the phosphor-coated optical fiber screen was measured with a flexible light bundle of 10 micron glass fibers. This bundle was encased in a black vinyl jacket and mounted in a plexiglas support

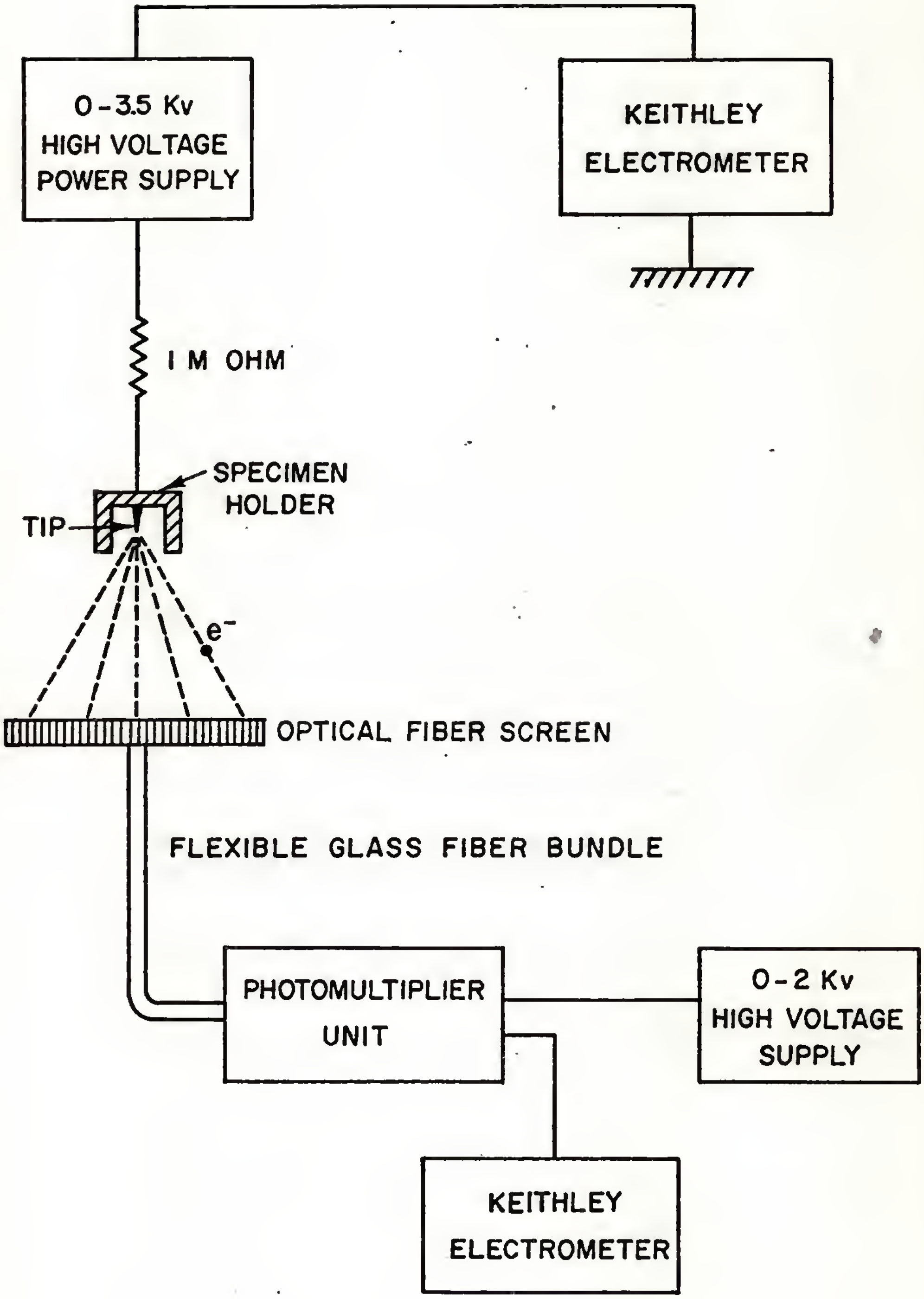

Figure 31. Circuit for point-by-point measurement of $\ln I$ vs. $1/V$.

stand. A Viton O-ring was compressed at the junction of the light bundle and optical fiber screen to minimize spurious light sources. The flexible light bundle was connected to a photomultiplier unit (see Figure 31). The resultant emission current was determined with a Keithley 600B electrometer and an atomic high voltage power supply provided the necessary potential to the photomultiplier unit.

The 3 mm diameter flexible light pipe enabled numerous measurements at various positions of a particular crystallographic pole to obtain a statistically valid average work function value. The manual adjustment of the high voltage power supply at preselected potentials and the recording of the corresponding current values required a significant amount of time. Since the pressure of the microscope body determined the time allotted the measurements from a "clean" emitter surface, it was necessary to field desorb(22) this chemisorbed monolayer before continuing the current-voltage determinations. For instance, the microscope was pumped normally to a minimum of $5x10^{-9}$ Torr which allowed the "clean" emitter to remain pure for 5,000 seconds, when a sticking coefficient of 0.1 was assumed.

In order to speed up the current-voltage data collection a simple analog circuit, as reported by Ehrlich(62) and Arthur,(63) was built to record ℓn I vs. 1/V data directly on an X-Y recorder as shown in Figure 32. The output potential of the high voltage supply was automatically

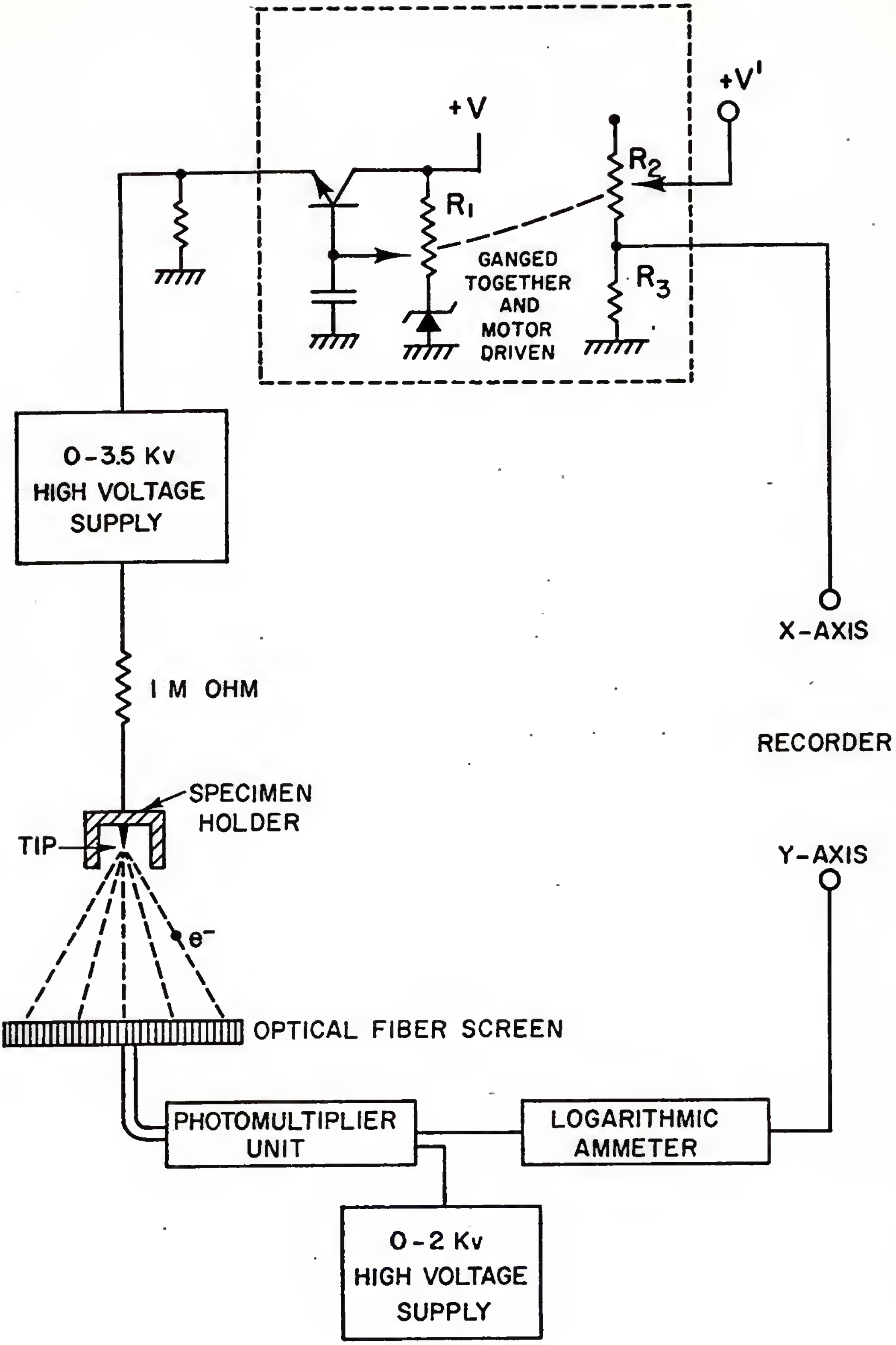

Figure 32. Circuit for automatic measurement of ℓn I vs. 1/V.

varied over a selected range and coupled to the X-axis of the recorder. The photomultiplied current was measured by the logarithmic ammeter which was connected in turn to the Y-axis input of the recorder. With this arrangement the complete Fowler-Nordheim plot over a current range of 10^{-11} to 10^{-6} amperes was recorded in less than 30 seconds. In addition, the work function values were determined with decreased computation. The values obtained by this method agreed with the data compiled by the point-by-point technique.

Calibration of Field Emission and Ionization Microscope

To assure accurate current measurements the photomultiplier unit and attached flexible light bundle were calibrated with a monochromatic light source with a wavelength of 0.54647 micron. This corresponds to the green light associated with the P-1 phosphor coating present on the optical fiber screen. The circuit scheme and results are shown in Figure 33. The two parallel lines at 730 and 990 volts represent data obtained when the positions of the Quantum Radiometer and photomultiplier tube were alternated. The linear behavior of these data above 10^{-7} watts indicates that the photomultiplier values correspond exactly to the Quantum Radiometer values over the selected range of incident beam intensity. The divergence in the lower region of the graph below 10^{-7} watts is attributed to the

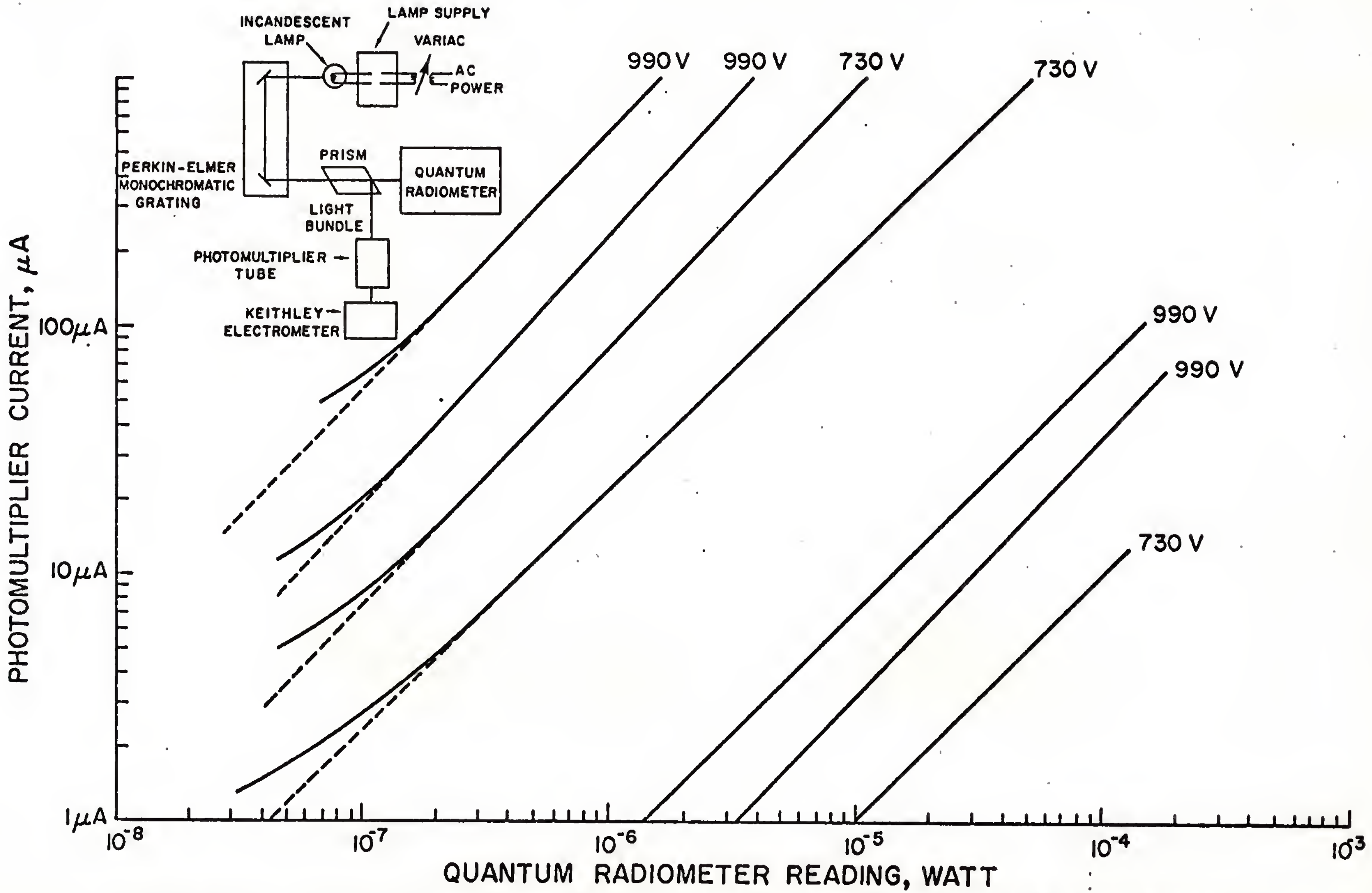

Figure 33. Calibration of photomultiplier current vs. Quantum Radiometer.

inaccuracy of the Quantum Radiometer for the low intensity incident light. On the other hand, if the divergence had appeared at a particular current value of the photomultiplier tube, then the inaccuracy would be due to the photomultiplier unit.

Tungsten specimens were imaged at 78°K in helium at $4.2x10^{-4}$ Torr and photographed at the optical fiber screen with Kodak Tri-X plates which were developed in accufine to effectively double the film speed. One of the interesting structures observed is shown in Figure 34(a). Notice that a boundary intersects the surface as indicated by the arrows. Also, note the improved image resolution as compared to the previous atom probe intensified images. From this photograph it was possible to count the number of net plane rings from the (011) plane to the center of the (112) plane and multiply by 16(11) to give an average tip radius of 432° Å. Local radii were also determined from the data summarized by Müller(11) for calculating the radius of curvature between two different planes. After accurately determining these radii values, the helium was removed and the microscope was switched to the field emission mode. When the pressure was less than $5x10^{-9}$ Torr, the positive potential was removed and the negative potential was applied. The field emission image obtained for this specimen is shown in Figure 34(b). The black spots in the image are molydisulfide

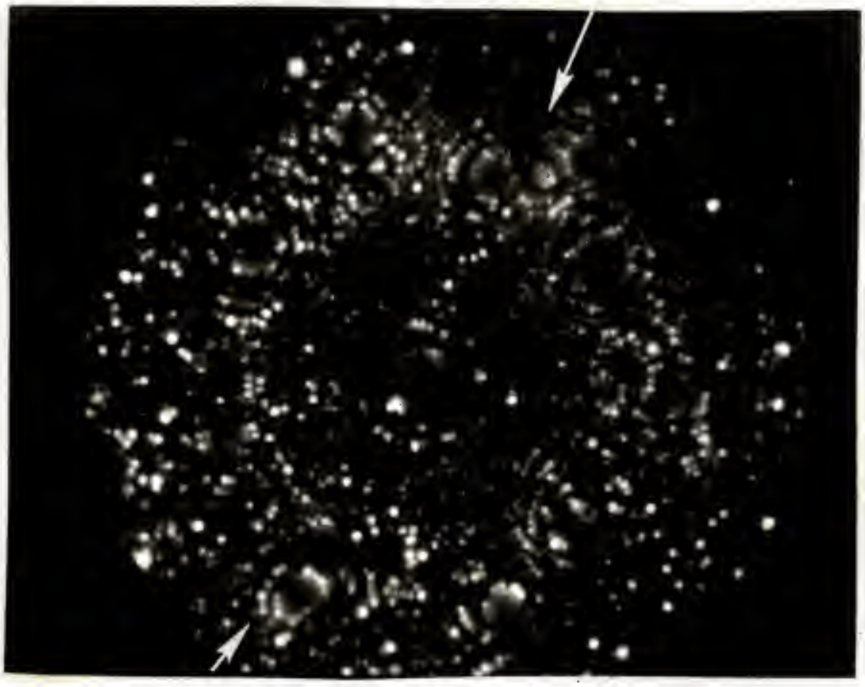

(a) Field-ion image.

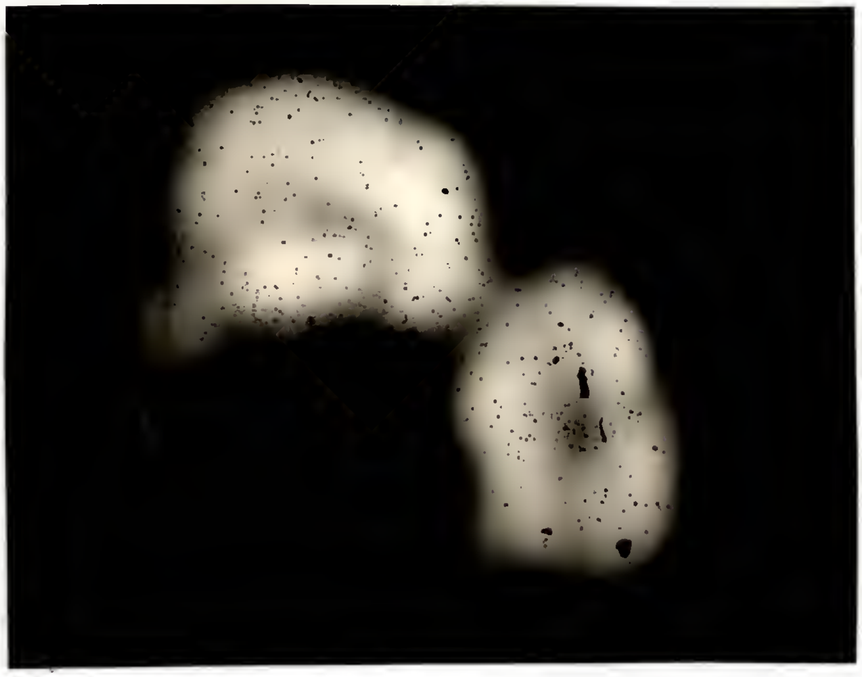

(b) Field emission image.

Figure 34. Field-ion and field emission images of tungsten obtained from fiber-optic screen.

particles which have fallen from the specimen holder's support yoke onto the phosphor-coated optical fiber screen. Because of the boundary present in this tungsten tip, one observes two symmetrical images separated by the boundary. The light regions in the image indicate the low work function regions such as the (111) poles, whereas the darker regions correspond to the high work function regions, i.e., the (011) and (112).

The resulting emission data for this specimen are shown in Figure 35, as a plot of $\ell n\ I/V^2$ vs $10^4/V$, where I and V are the measured current and emitter potential, respectively. The Fowler-Nordheim relation can be rearranged into the following form

$$\frac{I}{V} = \frac{6.16\mathrm{x}10^{-8}F^2A}{R^2} \exp\left\{-3.415\mathrm{x}10^8 \frac{R\phi^{3/2}}{V}\right. \left. v\left(\frac{1.8\mathrm{x}10^{-4}V^{1/2}}{R^{1/2}\phi}\right)\right\}, \qquad (31)$$

where ϕ is the work function in eV, F is the electric field in V/cm, v is a tabulated function, and A is the emitting area. This expression can be further simplified to

$$\frac{I}{V^2} = \frac{a}{R^2} \exp\left\{\frac{-bR}{V}\ v\left(\frac{cV^{1/2}}{R^{1/2}}\right)\right\}, \qquad (32)$$

where the constant values of a, b and c are evident. From the $\ell n\ I/V^2$ vs 1/V plot, the nearly straight line has an intercept $\ell n\ a/R^2$ and a slope -bRv. Substituting the slope

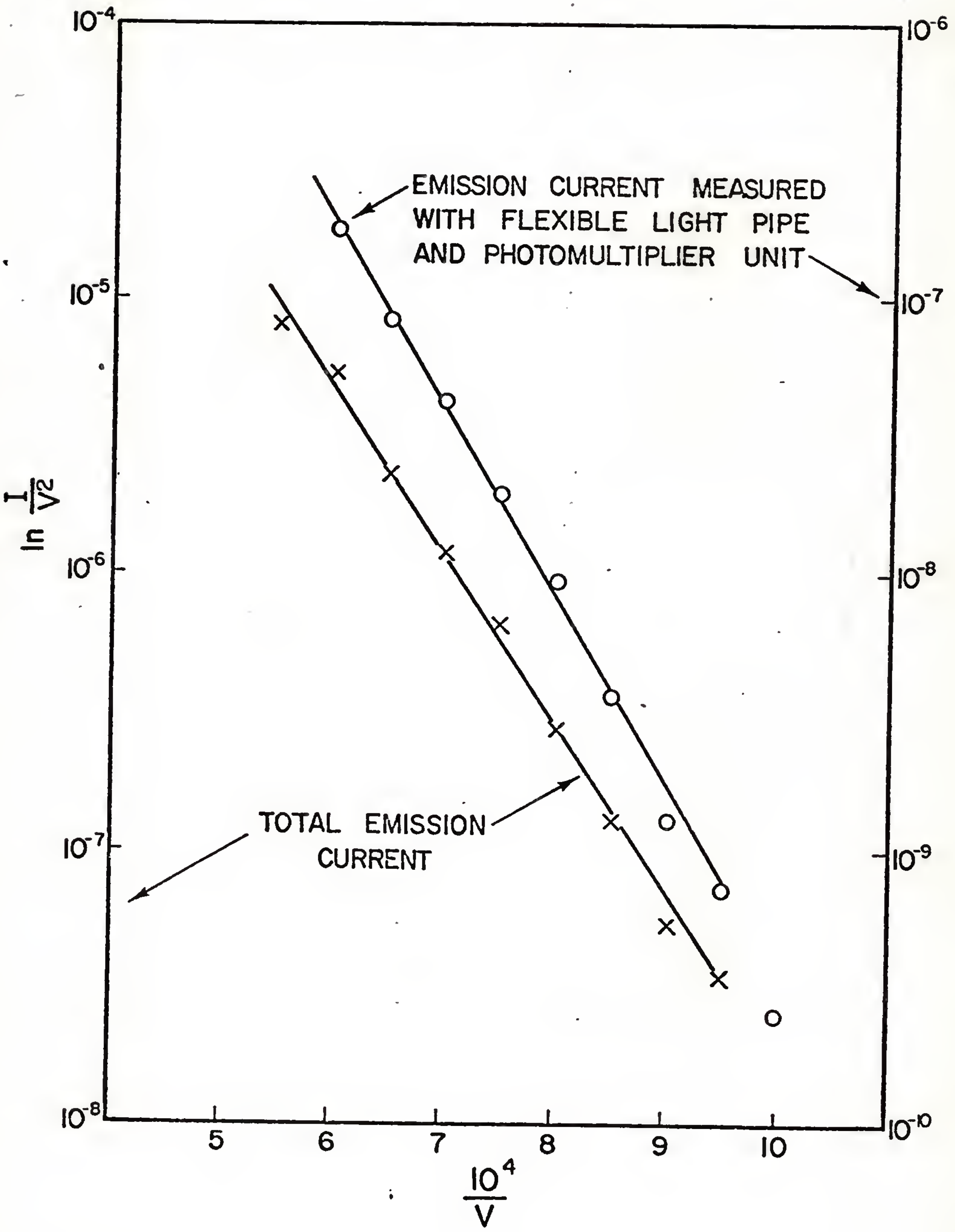

Figure 35. Field emission data for tungsten.

obtained from Figure 35 and the measured local radius of 196 Å for the (111) region, the calculated work function was 4.5 eV. This value is reasonable when compared to the reported value$^{(64)}$ of 4.39 eV for the (111) plane of tungsten. The slightly higher measured value can be attributed to an adsorbed layer of gaseous species. .

Feasibility of Analyzing Silicon

The importance of dislocations and their influence on the distribution of solute atoms in silicon has steadily grown evident in the past decade. Up to this time, however, there have been no studies conducted to determine the electronic nature of either a single dislocation or its solute atom atmosphere. It seems that these characterizations can be achieved with both the atom probe and field emission and field ionization microscopes. For instance, the available atomic resolution will allow observation of the emerging dislocations at the surface and the single particle mass spectrometry will provide identification of the solute atoms and their location in the structure. Consequently, work was conducted with 10^{14} to 10^{16} phosphor-doped silicon to establish if it could be polished to the required tip size (less than 1,000 Å), withstand the applied high electric field and form an image in the field ionization mode.

The first step required in making an acceptable silicon tip involved cutting 2 mm square-ended bars from (111) oriented wafers. It was determined that symmetrically shaped tips were only produced if the 2 mm cross-sections were precisely polished within ±0.001 mm. Tests were conducted to determine the rate and uniformity of the silicon removal for various HF-HNO_3 solutions selected from the literature.(65-68) The results are shown in Figure 36. From these data and visual observations of the etched silicon discs, the following scheme was devised to prepare an acceptable tip. First, the square-ended bars were polished in the 35 percent HF-HNO_3 solution until a uniform cylinder was formed. Next, the piece was inserted into either the 10 or 20 percent HF-HNO_3 solutions and held steadily in place until the immersed end falls in the solution. If the tip was quickly removed and washed in distilled water to prevent further etching, an adequate tip radius was normally produced better than 50 percent of the time. To verify if the tip was acceptable, it was observed optically at 430X magnification. If the birefringent lines were not continuous around the tip, then according to Müller(11) the tip radius was less than 1,000 Å. If the tip is unacceptable, a lacquer droplet can be put on the end and repolished in either the 10 or 20 percent HF-HNO_3 solutions. It is interesting to point out that current polishing of the silicon indicates an acceptable tip can also be achieved in the 35 percent HF-HNO_3 solution, providing the tip is quickly removed and rinsed with distilled water immediately after the immersed end falls.

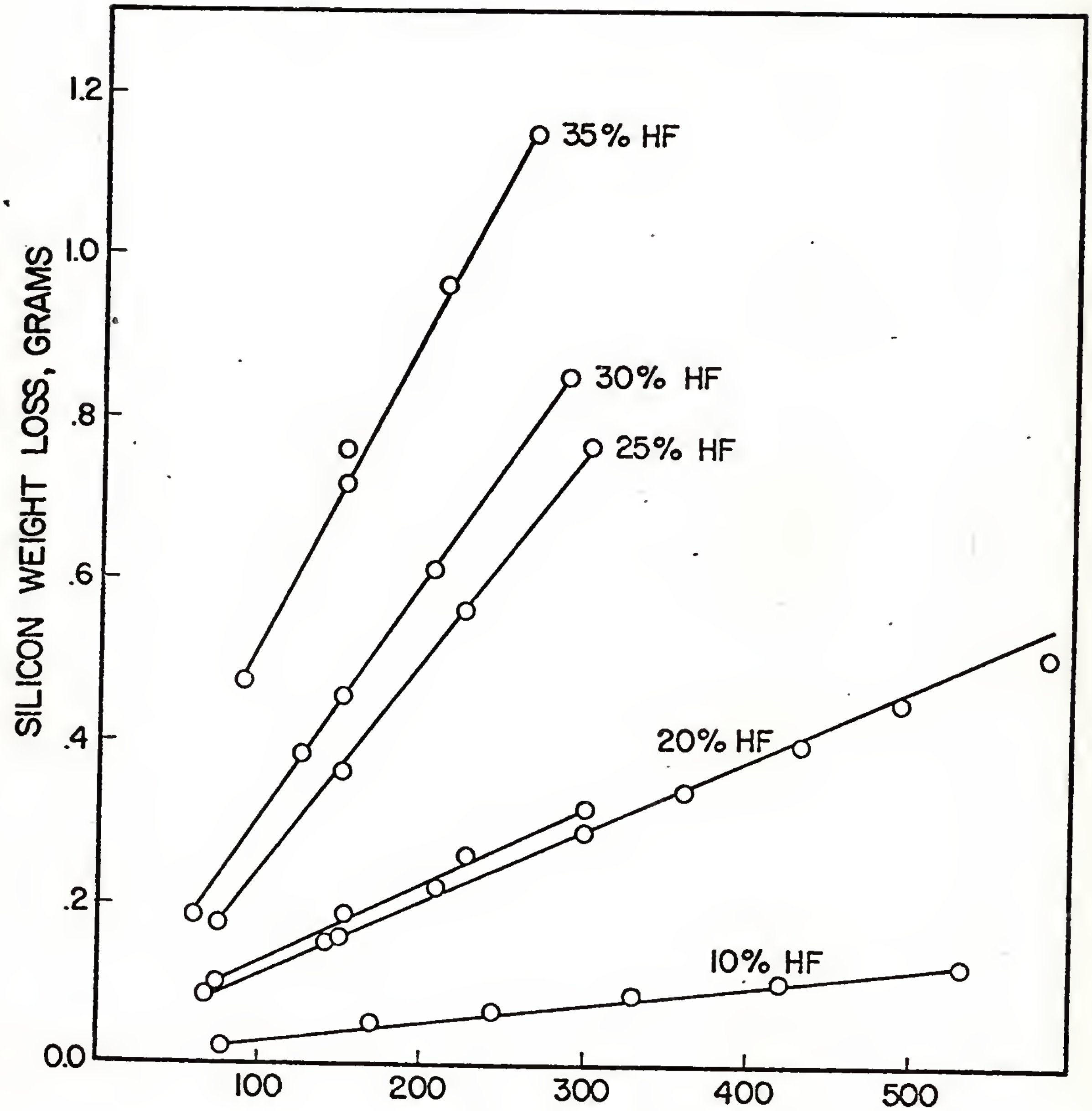

Figure 36. Silicon weight loss vs. time for different $HF-HNO_3$ solutions.

Initially, the shank of the silicon tip was cleaned with HF and plated with an electroless Nickelex solution to form an ohmic contact. The first mounted tip is shown in Figure 37. Note the evenly polished taper of the tip and the BT solder joint that connected the silicon to the nickel wire. Tests were made on this junction and the results indicated an ohmic contact. In addition, mounted tips that were plated with the electroless Nickelex solution were carefully crimped into new copper sleeves that were designed for the atom probe and field-ion microscope. Also, the tips can be vapor-coated with a 200 Å thick gold layer to assure ohmic contact.

Initial attempts to image the silicon were encouraging. For instance, in Figures 38(a), (b), (c) and (c), an image was developed at 11 kV in a helium-10 percent neon mixture with the tip temperature of 78°K. This particular sequence was taken during the field evaporation of the tip to produce a more symmetrically shaped tip. Notice the large elongated bright spots and streaking in Figure 38(a). As the field evaporation proceeded, dynamic observation of the ring formation and initiation of poles were observed. In Figure 38(b) the bright elongated spots mask out the grayer toned image spots which are believed to be the silicon surface atoms. However, at the outer boundaries of the image the white arrows point to these gray spots which are arranged in a circle and indicate the formation of a pole.

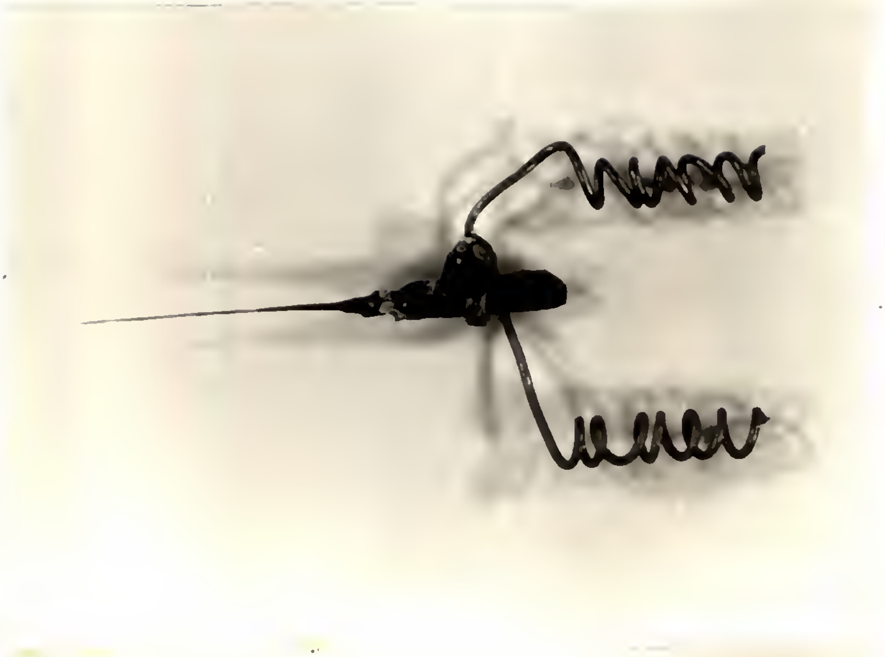

Figure 37. An acceptable silicon tip mounted to a nickel lead.

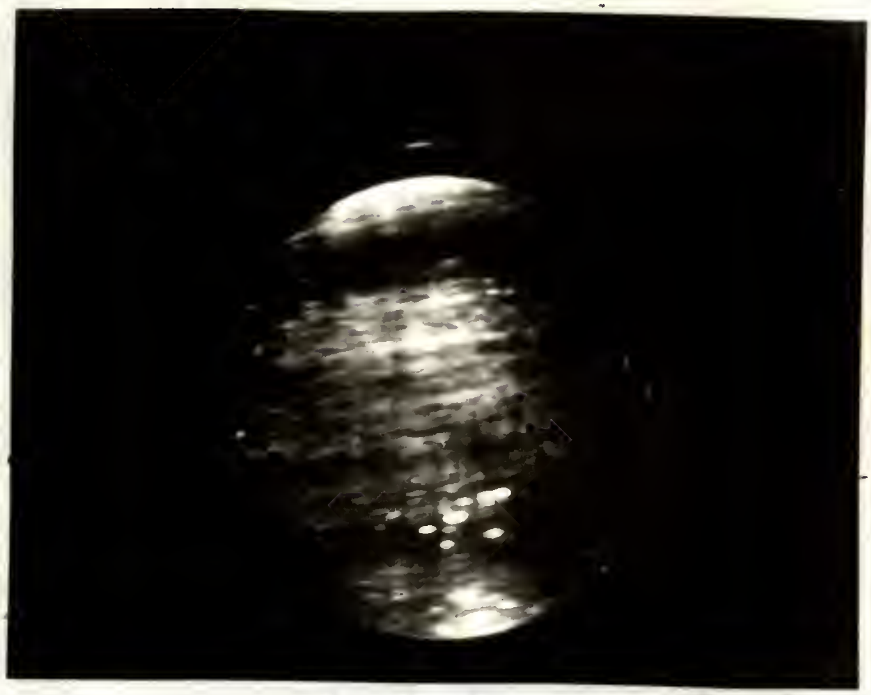

(a) Tip potential, 11 kV.

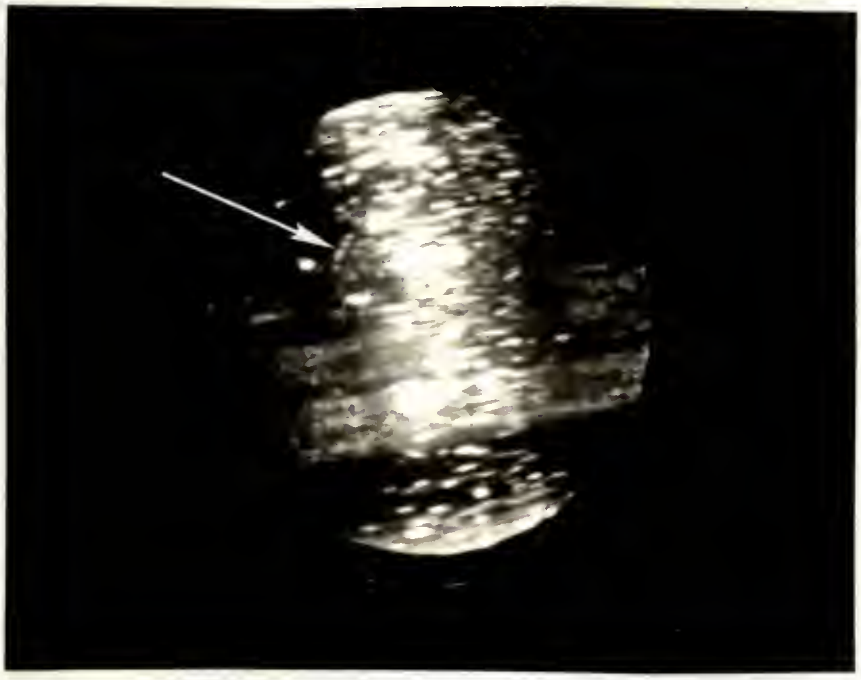

(b) Tip potential, 12 kV.

Figure 38. Field-ion micrographs of phosphor-doped silicon imaged at 78°K in a helium-10 percent neon mixture at 5×10^{-4} Torr.

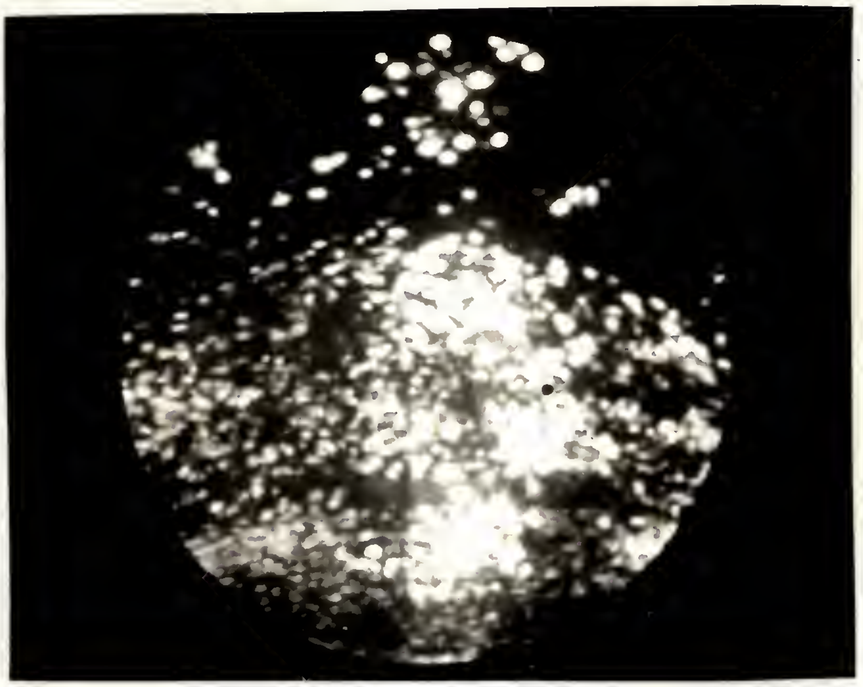

(c) Tip potential, 22 kV.

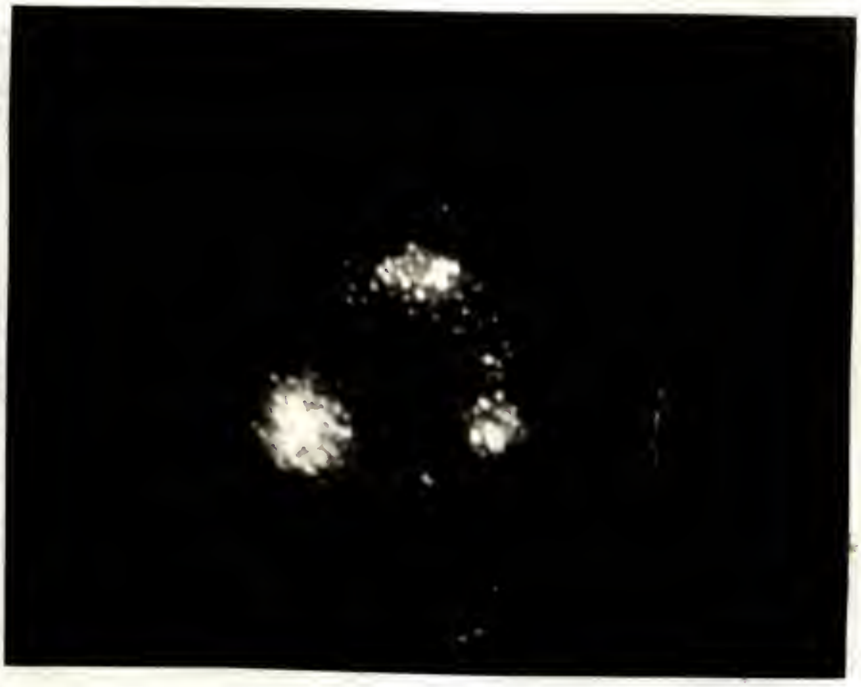

(d) Tip potential, 15 kV.

Figure 38. (cont.)

Figure 38(c) represents the silicon tip after the field evaporation potential was increased to 22 kV. Notice that the mean tip radius is more uniform and that distinct rings are becoming evident. The applied potential was decreased to 15 kV and the image, shown in Figure 38(d), indicates the formation of the three distinct (100) poles.

This sequence of micrographs of the phosphor-doped silicon tip indicated several important factors. First, the mechanical strength of the silicon at 78°K was sufficient to withstand the stress created by the applied potential. Next, the bulk electrical conductivity at 78°K and ohmic contact were adequate to produce field ionization of neon and helium gas mixtures. In addition, the tip withstood field evaporation potentials from 11 to 22 kV without flashing. Since the micrographs indicate an abundance of oxide image spots and their size appears adequate for alignment with the probe hole of the atom probe, future studies could be initiated to establish the chemical character of these image spots.

In order to aid interpretation of the silicon images, a computer simulation of the various important poles of the diamond cubic structure was developed. The shell and neighbor models developed by Sanwald and Hren(69) for the FCC structures were modified to the DC structure. The appropriate crystal information for the silicon was inserted in the shell model because it only maps one pole at a time and is less time-consuming than the neighbor model. Since the shell model is based primarily on a geometrical interpretation of the imaging surface, the radius of the tip is chosen arbitrarily to be less than 1,000 Å. The perfect silicon crystal structure was generated by assuming a perfect hemisphere at the tip and storing these (X,Y,Z) points in a fixed Cartesian coordinate system where X = $(1\bar{1}0)$, Y = (110) and Z = (001). The imaging criteria were based upon a thin shell which was cut from the outer limits of the tip surface. All the points whose radii lie in the thin shell are classified as image points. The program then expanded the image points and transformed them into a two-dimensional F-IM pole.

Successful simulated images were obtained for the (100), (111) and (112) poles when a radius of 360 lattice parameters was used. These images indicated the change in atomic surface structure as a function of the position in the crystal lattice. Once more, descriptive field-ion images of silicon are obtained, the radius of these computer simulations can be altered until the two images are similar. Since the field evaporation process was observed, the (100) pole was selected to simulate this process. The radius of the tip was changed from R = 362.15 to 361.90 in a 0.05 increments and the resulting images are shown in Figure 39. With this sequence of images the collapsing of the (100) plane is evident. At this time it appears very

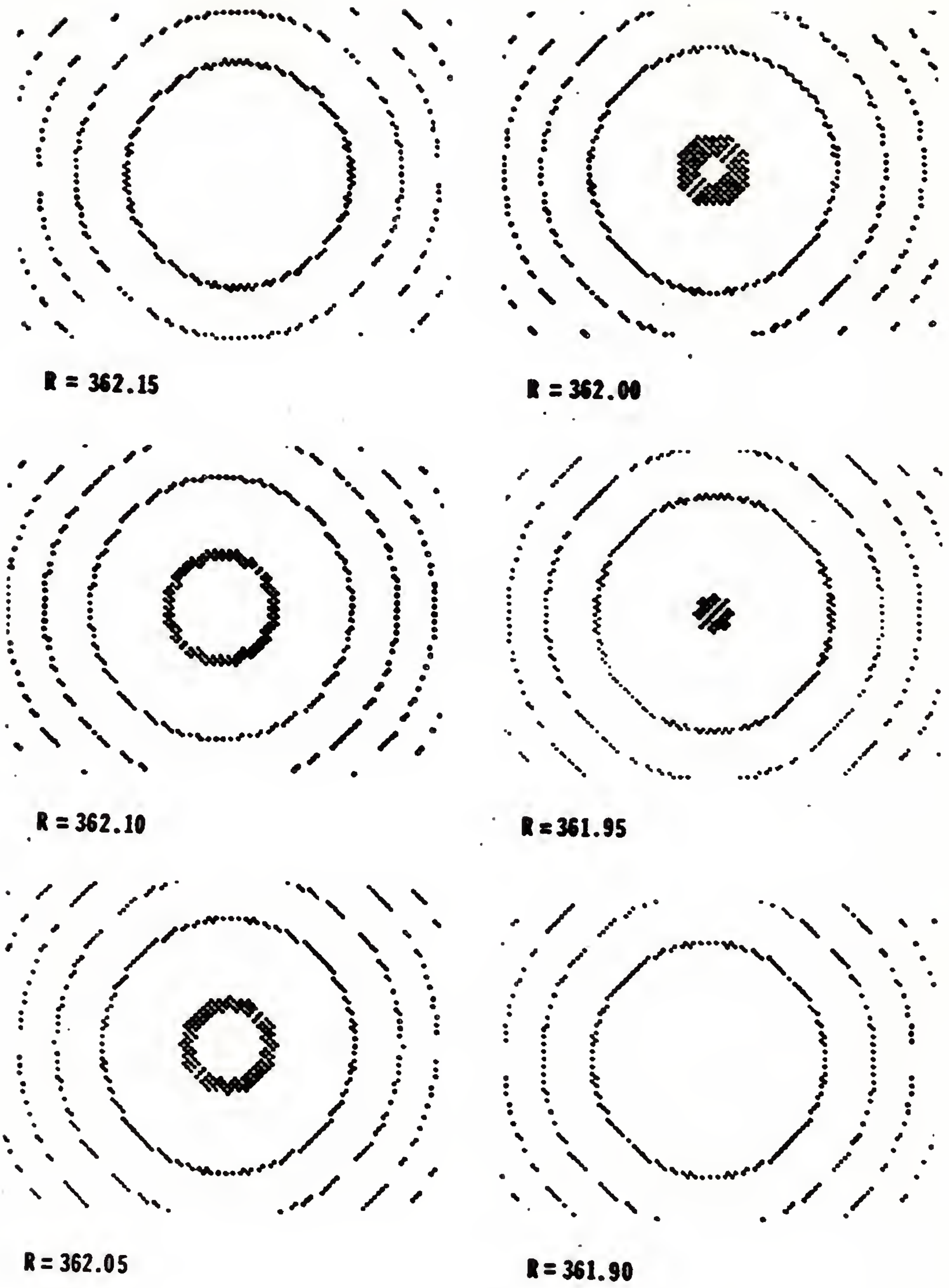

R = 362.15

R = 362.00

R = 362.10

R = 361.95

R = 362.05

R = 361.90

Figure 39. Computer simulated field evaporation of the (100) pole of silicon.

feasible to include the appropriate dislocation parameters in this program to develop computer images for dislocations emerging at these particular pole regions on the silicon surface.

CHAPTER VI

CONCLUSIONS

The operational performance of the individual components of the completed atom probe field-ion microscope is summarized as follows:

1. The atom probe system was capable of vacuums below 1×10^{-9} Torr.

2. An image intensifier was designed and included in the atom probe to improve the image. Its image formation parameters were established for helium, neon and helium-10 percent neon imaging gases.

3. Critical alignment of the specimen tip and ion detector was done by optical, He-Ne laser and electronic means.

4. A goniometer-type specimen manipulator was designed and constructed that allowed a minimum of 45° tilt in any direction while maintaining the specimen tip within 0.3 mm of the optical axis and while simultaneously maintaining the tip at high potential and at selected cryogenic temperatures.

5. The constructed specimen holder satisfied the simultaneous imaging requirements of electrical insulation, cryogenic cooling, mechanical manipulation and ultra-high

vacuum. It could also be positioned in a biased position to allow rapid specimen exchange.

6. Critical impedance matching of the high voltage pulse with the high voltage feedthrough circuitry was achieved, such that the sharp leading edge of the pulse was not affected, while the amplitude was only slightly reduced at the tip.

7. Single particle events were detected by the Bendix Spiraltron detector and the associated control circuitry functioned well to provide resulting traces of the single species.

The calibration of the atom probe indicated the following:

1. The sensitive area of the specimen tip depended upon the input aperture of the Spiraltron detector and ranged between 30 and 50 Å^2 for corresponding tip radii of 400 and 800 Å.

2. The Spiraltron detector was operated successfully in both the analog and pulse counting modes.

3. Precise alignment of the Spiraltron detector and specimen tip was made by monitoring the ion and electron currents emitted from the tip. The measured ion currents ranged from 10^{-17} to 10^{-14} amps which agreed with reported values.(52)

4. A defocusing effect was observed that prevented detection of the pulsed field evaporated ionic species.

This was attributed to a large time constant and residual charge buildup at the perimeter of the probe holes in the microchannel-plate and phosphor-coated screen. This effect was most important because even a 1 volt transverse component of the field was sufficient to deflect the path of the ions by 1 cm at the detector. The defocusing effect was remedied by using the microchannel-plate and screen as electrostatic einzel lenses. Optimum ion currents were obtained by applying the negative potentials of 225 and 1,850 volts to the microchannel-plate and screen, respectively.

5. Gas desorption studies of tungsten surfaces indicated that single image spots could be aligned with the probe hole. The following ionic species were identified from the 20 μsec traces taken with the Tektronix 549 Storage Oscilloscope: H^+, N^{++}, N^+, O^+, O_2^+, CO_2^+, WN_2^{+3}, WN_2^{++} and possibly $W_2O_5^+$. The efficiency in detecting these aligned single spots was about 50 percent. When the probe hole was fixed on a particular crystallographic plane this efficiency was decreased. However, the fixed probe hole method was successful in monitoring the field evaporation process, since the measured ion current was a maximum as the ionizing ring coincided with the probe hole.

6. Field evaporation of tungsten at 78°K in a helium-10 percent neon imaging gas indicated the following ionic species from the 10 and 20 μsec traces: CO_2^+, WO_2^{+4}, WO_2^{+3}, WH_2^+, $WO_2 \cdot H_2O^+$ and possibly $W_2O_5^{+3}$. In addition, H^+, Ne^{++},

N^{++}, O^{+} and possibly WH_2^{+4} were also observed. Since only the W^{184} isotope was assumed in identifying these species, it was difficult to confirm the presence of tungsten-helium and -neon compounds. However, if all the possible tungsten isotopes were present, an unambiguous distinction between the overlapping tungsten-hydrides and -helides compounds becomes very difficult. The efficiency in detecting the aligned surface atom was less than 50 percent. However, this could be improved by positioning the probe hole on the inside of the ionizing rings which confirmed the reported parallax between the surface atom and its ionization region.(11,52)

7. Calculations for the detected ionic species indicated better than a ±.5 AMU resolution for m/n ratios below 100 and ±.7 AMU for those m/n values above 100. In these calculations the pulse factor, α, and the electronic dead time, δ, were assumed two and zero, respectively. Suggestions were made to use single isotope metals and imaging gases to obtain an accurate pulse factor, α, and electronic dead time, δ, from a sufficient statistical representation of detected ionic species. However, if materials to be analyzed by the atom probe are not adjacent in the periodic table, no difficulty should exist in achieving better than ±.5 AMU mass resolution.

The significant conclusions determined from the constructed field emission and field ionization microscopes are as follows:

1. The microscope was capable of vacuums below 10^{-9} Torr.

2. The completed specimen exchange mechanism allowed successful specimen changes in less than two hours, while maintaining the microscope body below 1×10^{-7} Torr.

3. Improved image resolution was realized with the phosphor-coated optical fiber screen.

4. The field emission analysis of tungsten successfully measured the work function of the (111) plane of tungsten from the optical fiber screen.

5. The feasibility of preparing adequate tips of phosphor-doped silicon for field-ion studies was realized. Also, the initial F-IM images of silicon indicated excessive oxide formation, but indicated that field evaporation can be used to help develop a "clean" silicon surface.

Although certain refinements were discovered during the calibration of the atom probe, it is evident that the completed instrument is operational and capable of providing ±.5 AMU mass resolution for the field evaporated ionic species. The experimental results obtained with this versatile and powerful instrument suggest many future applications in materials science, physics and chemistry.

LIST OF REFERENCES

1. Inghram, M. G. and Gomer, R. J., Chem. Phys., 22, 1279 (1954).

2. Beckey, H. D., Z. Naturforsch., 16a, 505 (1961).

3. Block, J., Z. Phys. Chem., 39, 169 (1963).

4. Thomsen, M. P. R., Master's Thesis, Pennsylvania State University, 1963.

5. Vanselow, R. and Schmidt, W. A., Z. Naturforsch, 21a, 1690 (1966).

6. Barofsky, D. G. and Müller, E. W., Surface Sci., 10, 177 (1968).

7. Müller, E. W., Naturwissenschaften, 57, 222 (1970).

8. Müller, E. W., Panitz, J. A. and McLane, S. B., 14th Field Emission Symposium, Washington, D.C., 1967.

9. Müller, E. W., Panitz, J. A. and McLane, S. B., Rev. Sci. Instr., 39, 89 (1968).

10. Brenner, S. S. and McKinney, J. T., 15th Field Emission Symposium, Bonn, 1968.

11. Müller, E. W. and Tsong, T. T., Field Ion Microscopy, Principles and Applications, Elsevier Publishing Co., New York, 1969.

12. Müller, E. W., McLane, S. B. and Panitz, J. A., Proc. 4th European Reg. Conf. Electron Microscopy, Vol. 1, pg. 135, Rome, 1968.

13. Brenner, S. S. and McKinney, J. T., Appl. Phys. Letters, 13, 29 (1968).

14. Müller, E. W., Quart. Rev., 23, 177 (1969).

15. McKinney, J. T. and Brenness, S. S., 16th Field Emission Symposium, Pittsburgh, Pa., 1969.

16. Müller, E. W., Krishnaswamy, S. V. and McLane, S. B., Surface Sci., 23, 112 (1970).

17. Müller, E. W., Naturwissenschaften, 29, 533 (1941).

18. Müller, E. W., Phys. Rev., 102, 618 (1956).

19. Southon, M. J., Ph.D. Dissertation, University of Cambridge, 1963.

20. McKinstry, D., Surface Sci., 37, 1 (1972).

21. Brandon, D. G., Field-Ion Microscope, J. J. Hren and S. Ranganthan, eds., Plenum Press, New York, 1968.

22. Gomer, R., Field Emission and Field Ionization, Harvard University Press, 1961.

23. Brandon, D. G., Brit. J. Appl. Phys., 15, 349 (1963).

24. Müller, E. W., Advances in Electronics and Electron Physics, 18, 83 (1960).

25. Gomer, R. and Swanson, L. W., J. Chem. Phys., 38, 1613 (1963).

26. Tsong, T. T., J. Chem. Phys., 54, 4205 (1971).

27. Gadzuk, J. W., Surface Sci., 6, 133 (1967).

28. Bardeen, J., Phys. Rev., 92, 1140 (1953).

29. Juretschke, H. J., Phys. Rev., 92, 1140 (1953).

30. Loucks, T. and Cutler, P. H., J. Phys. Chem. Solids, 25, 105 (1964).

31. Brandon, D. G., Surface Sci., 3, 1 (1965).

32. Brandon, D. G., Phil. Mag., 14, 803 (1966).

33. Tsong, T. T., Surface Sci., 10, 102 (1968).

34. Tsong, T. T. and Müller, E. W., Phys. Stat. Sol., 1, 513 (1970).

35. Plummer, E. W. and Rhodin, T. N., J. Chem. Phys., 49, 3479 (1968).

36. Brandon, D. G., Surface Sci., 5, 137 (1966).

37. Machlin, E. S. et al., in 12th Field Emission Symposium, Pennsylvania State University, 1965.

38. McKinstry, D., Ph.D. Dissertation, University of Nevada, 1972.

39. Müller, E. W. and Tsong, T. T., 16th Field Emission Symposium, Pittsburgh, Pa., 1969.

40. Vanselow, R. and Schmidt, W. A., 13th Field Emission Symposium, Cornell University, 1966.

41. Dyke, W. P. and Dolan, W. W., Advances in Electronics and Electron Physics, 8, 89 (1956).

42. Drechsler, M. and Wolf, P. Proc. 4th International Conf. Electron Microscopy, Vol. 1, p. 835, Berlin, 1958.

43. Nishikawa, O. and Müller, E. W., J. Appl. Phys., 35, 2806 (1964).

44. Müller, E. W., Surface Sci., 8, 462 (1967).

45. Müller, E. W., McLane, S. B. and Panitz, J. A., Surface Sci., 17, 430 (1969).

46. Hren, J. J., Moore, A. J. W. and Spink, J. A., Surface Sci., 29, 331 (1972).

47. Müller, E. W., Berichte der Bunsen-Gesellschaft, 75, 979 (1971).

48. Müller, E. W., Panitz, J. A. and McLane, S. B., Rev. Sci. Instr., 40, 1321 (1969).

49. Stolt, K. G., Masters Thesis, UCRL-20303.

50. Tong, 17th Field Emission Symposium, Yale University, 1970.

51. Hren, J. J. and Stoltz, D. L., Am. Vac. Soc., Southeastern Section, Clearwater, Fla., 1972.

52. Brenner, S. S. and McKinney, J. T., Surface Sci., 23, 88 (1970).

53. Turner, P. J. et al., J. Sci. Instr., 2, 731 (1969).

54. Hren, J. J., Jenkins, D. A. and Stoltz, D. L., 16th Field Emission Symposium, Pennsylvania State University, 1969.

55. Schmidt, K. C. and Hendee, C. F., IEEE Trans. on Nucl. Sci., NC-13 [3], 100 (1966).

56. Schmidt, K. C., Bendix Electro-Optics Div. Tech. Appl. Note 9803, 1969.

57. Yellin, E., Yin, L. I. and Adler, I., Rev. Sci. Instr., 41 [1], 18 (1970).

58. Chen, Y. C. and Seidman, D. N., Surface Sci., 26, 61 (1971).

59. Müller, E. W., Z. Physik, 106, 541 (1937).

60. Air Products and Chemical Ins., Allentown, Pa.

61. Hren, J. J. and Newman, R. W., Rev. Sci. Instr., 38, 869 (1967).

62. Ehrlich, G. and Hudda, F. G., J. Chem. Phys., 35, 1421 (1961).

63. Arthur, J. R., J. Appl. Phys., 36, 3221 (1965).

64. Müller, E. W., J. Appl. Phys., 26, 732 (1955).

65. Robbins, H. and Schwartz, B., J. Electrochem. Soc., 106 [6], 505 (1959).

66. Klein, D. L. and D'Stefan, D. J., J. Electrochem. Soc., 109 [1], 37 (1962).

67. Robbins, H. and Schwartz, B., J. Electrochem. Soc., 107 [2], 108 (1960).

68. Schwartz, B. and Robbins, H., J. Electrochem. Soc., 108 [4], 365 (1961).

69. Sanwald, R. C. and Hren, J. J., Surface Sci., 7, 197 (1967).

BIOGRAPHICAL SKETCH

Daniel Lewis Stoltz was born December 9, 1937, at Princeton, Indiana. In June, 1956, he was graduated from Robinson High School, Robinson, Illinois. In February, 1961, he was graduated from the University of Illinois with the degree of Bachelor of Metallurgical Engineering. He worked as a powder metallurgist for Delco Morainne, Dayton, Ohio, from February, 1961, to February, 1962. From this time to August, 1966, he worked as a research metallurgist at Battelle Memorial Institute in Columbus, Ohio. In September, 1966, he entered Graduate School at the University of Florida. He has worked as a research assistant in the Department of Metallurgical and Materials Engineering since that date. In June, 1970, he received a degree of Master of Engineering in Metallurgical and Materials Engineering and since that date has pursued the degree of Doctor of Philosophy in the same discipline.

Daniel Lewis Stoltz is married to the former Orleen Faye Corn and is the father of three children. He is a member of Omicron Delta Kappa, Alpha Sigma Mu, Epsilon Lambda Chi, American Institute of Mining, Metallurgical and Petroleum Engineers, American Society for Metals, American Ceramic Society, and the American Powder Metallurgy Institute.

I certify that I have read this study and that in my opinion it conforms to acceptable standards of scholarly presentation and is fully adequate, in scope and quality, as a dissertation for the degree of Doctor of Philosophy.

JJ Hren

J. J. Hren, Chairman
Professor of Materials Science
and Engineering

I certify that I have read this study and that in my opinion it conforms to acceptable standards of scholarly presentation and is fully adequate, in scope and quality, as a dissertation for the degree of Doctor of Philosophy.

L. L. Hench
Professor of Materials Science
and Engineering

I certify that I have read this study and that in my opinion it conforms to acceptable standards of scholarly presentation and is fully adequate, in scope and quality, as a dissertation for the degree of Doctor of Philosophy.

R. T. DeHoff

R. T. De Hoff
Professor of Materials Science
and Engineering

I certify that I have read this study and that in my opinion it conforms to acceptable standards of scholarly presentation and is fully adequate, in scope and quality, as a dissertation for the degree of Doctor of Philosophy.

James B. Conklin, Jr.

J. B. Conklin
Associate Professor of Physics

I certify that I have read this study and that in my opinion it conforms to acceptable standards of scholarly presentation and is fully adequate, in scope and quality, as a dissertation for the degree of Doctor of Philosophy.

E. H. Hadlock

E. H. Hadlock
Professor Emeritus of Mathematics

This dissertation was submitted to the Dean of the College of Engineering and to the Graduate Council, and was accepted as partial fulfillment of the requirements for the degree of Doctor of Philosophy.

December, 1972

Robert E Uhrig

Dean, College of Engineering

Dean, Graduate School

UNIVERSITY OF FLORIDA
3 1262 08553 9855